UNIVERSITY OF CALIFORNIA
RIVERSIDE

Portable and Innovative Approaches for Air Quality Characterization: Using Drones, Environmental Chambers, and Mobile Laboratories to Characterize Ozone, Methane, and Atmospheric Aerosols

A Dissertation submitted in partial satisfaction
of the requirements for the degree of

Doctor of Philosophy

in

Chemical and Environmental Engineering

by

Zihan Zhu

September 2023

Dissertation Committee:
Dr. Don R. Collins, Chairperson
Dr. David R. Cocker III
Dr. Cesunica Ivey

The Dissertation of Zihan Zhu is approved:

Committee Chairperson

University of California, Riverside

Acknowledgements

The past five years have been an incredible journey, and I am filled with gratitude towards the many people who have made it possible.

I feel blessed to have Don as my advisor. It was him to give me the opportunity to join him at Riverside. His unwavering support has been the source of my confidence, and the challenges we have overcome together will forever hold a special place in my heart. I appreciate the guidance from all the professors I have worked with, especially Dr. Cocker, Dr. Ivey, Dr. Miller, and Dr. Hopkins.

I started my graduate study with no experience in lab. I owe a great debt of gratitude to those within and outside my research group who supported me along the way. Being a part of my group, alongside Ningjin, Xuanlin, Minghao, Ying, Diana, Josh, and Candice, has been a true blessing. Additionally, I am grateful for the friendships that have blossomed with Khanh, Javier, Isis, Ranga, Yifan, Qi, Chen, Sahar, Hyuna, Hanwei, Tianbo, and Jerry outside of graduate school. As all my research projects involved field campaigns, I want to thank the staff at ARM and all my collaborators in Visalia and Houston for making the fieldwork both enjoyable and productive.

Above all others, I received the most love and support from my family and friends. Jing would probably not know how much joy I got from our monthly movie nights. I'm lucky to have Xiangyu together in so many adventures. Last but not least, I'll be forever grateful to my parents as my biggest supporters since day one.

ABSTRACT OF THE DISSERTATION

Portable and Innovative Approaches for Air Quality Characterization: Using Drones, Environmental Chambers, and Mobile Laboratories to Characterize Ozone, Methane, and Atmospheric Aerosols

by

Zihan Zhu

Doctor of Philosophy, Graduate Program in Chemical and Environmental Engineering
University of California, Riverside, September 2023
Dr. Don R. Collins, Chairperson

Different air pollutants have unique properties, spatial and temporal distributions that require different approaches to accurately measure and characterize them. This dissertation presents four different approaches for characterizing air pollutants in various regions using unmanned aerial systems (UAS), environmental chambers, and mobile laboratories.

An onboard sensor based UAS measurement system was developed to measure vertical ozone and particulate matter profiles in Riverside, CA from August to November 2020. The profiles were compared with ground monitoring and Community Multiscale Air Quality (CMAQ) model simulations. The study investigated the sensitivity of the model to various factors. The study found biases in the default version of the model's planetary boundary layer (PBL) and NOx emissions contributing to the model's bias.

The second project aimed to develop a solution for quantifying methane emissions using UAS. The sample collection system with wind estimation was validated for locating, identifying, and quantifying methane emissions. The results demonstrated the real potential of UAS for improving our understanding of methane emissions.

The third project studied new particle formation (NPF) and growth using the Captive Aerosol Growth and Evolution (CAGE) chamber system at the DOE Atmospheric Radiation Measurement (ARM) Program's Southern Great Plains (SGP) site in Oklahoma. The study investigated the sensitivity of particle growth to injected seed particle composition, liquid water content, and precursor gases. The time dependence of the growth rate was quantified. The study investigated the sensitivity of particle growth to injected seed particle composition, liquid water content, and precursor gases.

The fourth project was conducted in the Houston Metropolitan area in the summer of 2022. A mobile laboratory was deployed at five sites over various atmospheric conditions to gather data on particle size distribution, CCN activity, aerosol optical properties, aerosol composition, trace gas, and meteorological parameters. The collected data was analyzed to investigate the spatial and temporal variability and meteorological impact on new particle formation and growth.

These approaches using UAS, environmental chambers, and mobile laboratories are helpful for improving air pollution characterization. The results of these studies can be used to develop targeted and effective air quality control policies, and to provide insights for more accurate climate modeling.

Contents

1. Introduction 1

2. Unmanned Aerial System-Based Vertical Ozone and Particulate Matter Measurements and Model Comparisons in Riverside, CA 5

2.1. Introduction 5

2.2. Methods 7

2.2.1. Site Description 7

2.2.2. Platform and Instrumentation 9

2.2.3. UAS Flights 12

2.2.4. CMAQ Model Description 13

2.2.5. Ground Observation Data 15

2.3. Results and Discussion 16

2.3.1. Vertical Profile Patterns 16

2.3.2. Model Comparisons With the Ground and UAS Measurements 18

2.3.3. Evaluation and Model Inter-comparisons with Modifications 20

2.3.4. Impact of PBL Change on Ozone 21

2.4. Conclusions 29

2.5. References 31

3. Toward On-Demand Measurements of Greenhouse as Emissions Using Multirotor Uncrewed Aircraft Systems 35

3.1. Introduction 35

3.2. Methods and Materials 38

3.2.1. Field Operations 38

3.2.2. Ground-Based Meteorological and Gas Sensors 41

3.2.3. Aircore System 42

3.2.4. Multirotor UAS Wind Velocity Sensing 44

3.2.5. Evaluation of Multirotor UAS Wind Velocity Estimates 46

3.2.6. Methane Emission Estimates 47

3.3. Results 50

3.3.1. Multirotor UAS Wind Velocity and Air Composition Profiles 50

3.3.2. Validation of Multirotor UAS Wind Velocity Profiles 53

3.3.3. Validation of Aircore Profiles 55

3.3.4. Comparison of Emission Rates Estimated from Different Methods 57

3.4. Conclusions 59

3.5. References 61

4. Small Particle Growth Observations at the U.S. DOE Southern Great Plains Field Site Using Ambient Air Captive Aerosol Chambers 63

4.1. Introduction 63

4.2. Methods 65

4.2.1. CAGE Chambers 65

4.2.2. Measurement Site 69

4.2.3. Instrumentation 70

4.3. Results 72

4.3.1. Hourly Variations of Particle Growth Rate 72

4.3.2. Case Study: 10 October, Growth with Air Mass Change 75

4.3.3. Effect of Gas Addition of Precursor Gases on Particle Growth Rate 77

4.3.4. Effect of Particle Compositions on Particle Growth Rate 79

4.4. Summary 83

4.5. References 85

5. Mapping the Aerosol Properties at Houston During the TRACER-MAP Campaign 88

5.1. Introduction 88

5.2. Methods 89

5.2.1. Sites Description 89

5.2.2. Instrumentations 91

5.2.3. Data Analysis 94

5.3. Results and Discussion 95

5.3.1. Particle Number Size Distributions 95

5.3.2. New Particle Formation Events 97

5.3.3. Supermicron Particles 101

5.3.4. CCN Activity 103

5.4. Conclusions 106

5.5. References 108

6. Conclusions and Recommendations for Future Work 119

List of Figures

Figure 2-1 (Top) Satellite image of the launch site in Riverside, California, United States. (Bottom) Depiction of the launch site relative to the campus of University of California, Riverside, and the interstate highway 215. 9

Figure 2-2 Pictures of (a) DJI Matrice 600 Pro, (b) Personal Ozone Monitoring (POM), (c) Portable Temperature and Humidity Data Logger OM-141, (d) MINIMA from Applied Particle Technology. 11

Figure 3-1 a) A satellite image showing the locations where multirotor UAS flight operations were performed to measure wind velocity and air composition vertical profiles on January 20th, 21st, and 24th, 2020. b) An image of the UAS-based Aircore system profiling air composition while steadily ascending up to 120 m above ground level. 39

Figure 3-2 a) An illustration of the vertical flight operation. b) The process of the Aircore system pulling samples. C) The inner structure of the Aircore. 40

Figure 3-3 The a) and b) images show the CSAT-3 sonic anemometers installed on a meteorological evaluation tower at heights of 3 m and 11 m above ground level, respectively. The c) image shows the Picarro G1301 gas analyzer used to measure CH_4 and CO_2 concentrations of Aircore samples. 41

Figure 3-4 A schematic of the setup used during the Aircore calibration experiments. The solid lines and arrows show the gas flow when the Picarro analyzer and Aircore pulled air simultaneously. The dashed lines and arrows showed the gas flow when the Picarro

analyzer pulled air from the Aircore system. b) A schematic showing the needle valve position over time during the Aircore calibration experiment. 44
Figure 3-5 a) A schematic showing the configuration of the body-fixed reference unit vectors b_1, b_2, and b_3, relative to the front, right, and bottom sides of the multirotor sUA airframe. b) A schematic showing how the orientation of the body-fixed reference frame relative to the inertial reference frame is used to measure the $\boldsymbol{\alpha}$ and $\boldsymbol{\beta}$ parameters used to estimate wind speed and wind direction separately. 47
Figure 3-6 The vertical profiles of wind velocity, methane, and carbon dioxide measured using the sUAS-based Aircore system from a) 9:55 to 10:06 PST on January 20th, 2020, b) 15:54 to 16:06 PST on January 21st, 2020, c) 16:24 to 16:36 PST on January 21st, 2020, a, and c) from 16:38 to 16:49 PST on January 24th, 2020. 52
Figure 3-7 A pollution rose analysis showing how the mole fraction of methane changed with respect to wind direction and altitude during the second and third flights performed at the same solation. The a) and d) satellite images show the location where the second and thirds deployments took place on January 21st, 2020. The b) and c) pollution rose plots show methane enhancement variations with respect to wind direction and height during the second flight. The e) and f) pollution rose plots show methane enhancement variations with respect to wind direction and height. 53
Figure 3-8 The comparison of wind speed observations measured using the UAS-based Aircore sytem and the 11-m MET tower from a) 9:55 to 10:06 PST on January 20th,

2020, b) 15:54 to 16:06 PST on January 21st, 2020, c) 16:24 to 16:36 PST on January 21st, 2020, and c) from 16:38 to 16:49 PST on January 24th, 2020. 54
Figure 3-9 A plot showing the comparison of Aircore and CRDS (Direct) measurements of mole fraction spikes produced over time intervals of 5 and 10 seconds. 56
Figure 3-10 The comparison of methane and carbon dioxide observations collected from the UAS-based Aircore system and a ground-based CRDS from a) 9:55 to 10:06 PST on January 20th, 2020, b) 15:54 to 16:06 PST on January 21st, 2020, c) 16:24 to 16:36 PST on January 21st, 2020, and c) from 16:38 to 16:49 PST on January 24th, 2020. 57
Figure 3-11. Sensitivity map predicted by the dispersion model. The solid triangle shows the place where the drone was flown, and the rectangle area shows the nearest dairy farm we focused on researching. Tr on the color bar is the transport matrix dispersion model estimates, its unit is ppm per unit emission rate. 58
Figure 4-1 Sketch of a CAGE chamber showing the path of ambient air that is pulled in through an inlet, filtered, and then flows through the center of the ePTFE membrane-wrapped center channel..... 66
Figure 4-2 Comparison of spectral intensity measured just below one of the chambers and just outside of the chamber enclosure on a sunny day..... 68
Figure 4-3 (a): Satellite images of the Southern Great Plains (SGP) site relative to Oklahoma and Kansas. (b): The location of SGP at which the field study was conducted. Map data © 2022 Google. (c): the clearing in which the chambers and instrument trailers were..... 69

Figure 4-4 Schematic of the dual-chamber experimental system. 72
Figure 4-5 Top: Ambient aerosol size distribution time series from October 8th to 11th during the 2021 study. Middle and bottom: size distribution time series over the same period in chamber A and B with ambient air flushed. Left: x-y presentation of the size distribution measured at the time indicated by the rectangle in the time series. 73
Figure 4-6 Top: Time series of the lognormal fit diameters of injected modes in Figure 4-5. Lower: Calculated growth rates for the same period at the top. 74
Figure 4-7 Hourly average particle growth rate histogram. A total of 1212 values were used to construct the histogram. The time of sunrise and sunset for the first (October 8) and last (November 18) day of measurements are also indicated. 75
Figure 4-8 (a): Ambient aerosol size distribution time series. (b): time series of the lognormal fit diameters of injected modes in the two chambers. (c): calculated growth rates for the same period in (b). (d): wind direction and wind speed. (e): ambient relative humidity and temperature. (f) ambient SO_2 and O_3 concentration. (f): non-refractory submicron aerosol species measured with the ACSM. 76
Figure 4-9 (a): Ambient aerosol size distribution time series over 2.5 days during the α-pinene injection. (b): Size distribution time series over the same period in the reference chamber with ambient air flushed. (c): Size distribution time series over the same period in the perturbed chamber with ambient air and 5 ppb α-pinene flushed. (d): Time series of the lognormal fit diameters of injected modes in the two chambers. (e): Particle growth rates calculated from the time series of lognormal fit diameters. 78

Figure 4-10 (a): Ambient aerosol size distribution time series 4 days during the SO_2 injection. (b): Size distribution time series over the same period in the reference chamber with ambient air flushed. (c): Size distribution time series over the same period in the perturbed chamber with ambient air and 5 ppb SO_2 flushed. (d): Time series of the lognormal fit diameters of injected modes in the two chambers. (e): Particle growth rates calculated from the time series of lognormal fit diameters..... 79
Figure 4-11 (a): Ambient aerosol size distribution time series 2 days during the particle compositions sensitivity experiment. (b): Time series of the lognormal fit diameters of injected modes in the two chambers. (c): Particle growth rates calculated from the time series of lognormal fit diameters with markers for modes in aqueous phase based on the RH history and efflorescence and deliquescence RH of the two types. (d): Wind direction and wind speed. (e): Ambient relative humidity and temperature. (f) Ambient SO_2 and O_3 concentration. (g): Mass fractions..... 82
Figure 5-1 Locations of the five sites. 90
Figure 5-2 MAQL2 outer and inner instrumentation..... 92
Figure 5-3 Times series of the number and volume distributions throughout the campaign. 96
Figure 5-4 Times series of the number (left) and volume (right) distributions throughout the campaign. 96
Figure 5-5 (a): Ambient aerosol size distribution time series 2 days during a storm. (b): Time series of the lognormal fit diameters of identified and particle growth rates

calculated correspondingly. (c): Wind direction and wind speed. (d): Ambient relative humidity and temperature. (e) Dew point and solar intensity. (f): KAZR reflectivity. .. 100
Figure 5-6 Number and volume size distributions before, during, and after the storm.. 101
Figure 5-7 Comparisons of time series of the total number and volume concentration measured by MAQL2 and AMF. 102
Figure 5-8 (Top) Time series of the total number concentration measured by MAQL2 and Single Scattering Albedo (SSA). (Bottom) Time series of the absorption and scattering coefficient at 365 and 450 nm..... 103
Figure 5-9 The summary of the hygroscopicity coefficient κ and critical dry diameter Dp_50 at supersaturation Sc of 0.15, 0.37, and 0.64 for different sites..... 105
Figure 5-10 Diurnal cycle of averaged hygroscopicity coefficient κ at different sites... 106

List of Tables

Table 3-1 Summary of multirotor UAS and Aircore flight operations conducted in the San Joaquin Valley, California in January. 40

Table 3-2 Dairy farm sections likely to produce methane emissions from enteric fermentation or manure management. 48

Table 3-3 Integrated comparison area under the signals lasting the duration of 5 and 10 seconds. 56

Table 5-1 List of sample sites 91

Table 5-2 List of instrumentation deployed in the MAQL2. 93

Table 5-3 New particle formation event summary 98

1. Introduction

Air pollution has detrimental effects on human health, environment, and climate. Despite the significant progress made over many years, there are still various regions worldwide where particulate matter and ground-level ozone pose substantial risks to health. Scientific research has proven that exposure to PM and ozone can lead to permanent respiratory damage and even premature deaths (Abbafati et al., 2020). Methane, a long-lasting greenhouse gas, poses a significant threat to both present and future generations by contributing to climate change and ocean acidification (Turner et al., 2019). Atmospheric aerosols influence air quality, human health, the ecosystem, and climate (IPCC, 2021). Aerosols have an impact on climate by either absorbing or scattering solar radiation, or by indirectly influencing cloud properties, particularly when they reach a size of 50-100 nm, at which point they can act as cloud condensation nuclei (CCN) (Seinfeld and Pandis, 2016). The number and activity of CCN are crucial factors in understanding the climatic effects of aerosols.

Understanding, predicting, and potentially mitigating the negative effects of air pollutants rely on comprehensive quantification and characterization under a wide range of conditions. Traditionally, fixed-location ground measurements and satellite observations have been used to measure gas and particle-phase air pollutants. However, ground observations are limited in their ability to provide spatially resolved measurements over a large area and capture three-dimensional data under varying emission scenarios. Satellite

observations are insufficient in providing high resolution sub-region level geographically resolved insights. Therefore, there is a growing demand for portable, cost-effective, and time-efficient atmospheric measurement techniques to address these limitations.

Chapter 2 presents an unmanned aerial system (UAS) based measurement system using onboard ozone and particulate matter (PM) sensors. It is common biases exist between model-simulated ozone and ground site measurements (J. J. Guo et al., 2018; Travis et al., 2016). Previous studies have linked the complex patterns of vertical transport of ozone to model simulation performance (Akimoto et al., 2019; Fast et al., 2014; Lin & McElroy, 2010; Li & Rappenglueck, 2018). The 327 vertical ozone and PM concentration profiles from a 4-month-long daily routine measurement are compared with monitoring station measurements and Community Multiscale Air Quality (CMAQ) model simulated results statistically. The discussion includes the planetary boundary layer (PBL) estimated from a ceilometer to understand the potential reason for the model bias related to the vertical structure in meteorology. Additionally, the study investigates the sensitivities of the model results to factors such as PBL, eddy diffusivity, NO_x, and VOC emissions.

In Chapter 3, an Aircore-based UAS sample collection system was developed to measure methane emissions from dairy sources. Methane is a powerful greenhouse gas that is contributing to climate change and is mainly caused by human activities such as oil and gas extraction, solid waste management, and agriculture (Duren et al., 2019). Conventional methods for identifying greenhouse gas sources use fixed or mobile sensors, which are less accurate and sensitive compared to cavity ring-down spectroscopy. Moreover, ground

measurements cannot track how greenhouse gas concentrations and weather variables change within the PBL, which is critical for estimating emission rates. UAS provides an affordable and easy-to-operate approach for obtaining air samples for more accurate analysis. By using UAS's rotational kinematics parameters to estimate winds, the methane emissions were assessed for dairy sites in Central California.

Chapter 4 discussed the small particle growth at the U.S. DOE Southern Great Plains field site using ambient air captive aerosol chambers. New particle formation (NPF) and growth influence the solar radiation budget and the microphysics and properties of clouds (Seinfeld and Pandis, 2016). The traditional environmental chambers for studying small particle growth are limited in that they typically only cover one or a small number of precursor gases, leading to large variations between different locations. To address this, the Captive Aerosol Growth and Evolution (CAGE) chamber system was developed and deployed to investigate the growth rate over a 4-month long campaign, as well as the sensitivity of particle growth to the injected seed particle composition, liquid water content, and precursor gas additions.

Chapter 5 explores studying atmospheric aerosols using mobile platforms. The Tracking Aerosol Convection Interactions Experiment (TRACER) experiment aimed to map aerosol properties in the Houston Metropolitan area through a comprehensive series of aerosol, gas, and meteorological measurements. Measurements were taken at five different sites, and various atmospheric conditions were covered, including both local and transported emissions and different meteorological phenomena like precipitation and convection. The

data collected during the experiment was analyzed to explore spatial variability and investigate the impact of meteorological factors on new particle formation and growth, as well as CCN activity.

2. Unmanned Aerial System-Based Vertical Ozone and Particulate Matter Measurements and Model Comparisons in Riverside, CA

2.1. Introduction

Air pollution is a major health risk factor globally (Abbafati et al., 2020). Ground-level ozone is one of the six criteria air pollutants regulated by the USEPA because of its adverse impacts on people's health. Globally, it is linked to over one million premature deaths annually (Jerrett et al., 2009; C. et al., 2010). Moreover, tropospheric ozone is a short-lived climate pollutant that contributes to global warming (Stocker et al. 2013). It is mainly formed in the atmosphere through secondary chemical reactions involving ozone precursors including NO_x, CO, VOCs (volatile organic compounds), and PANs (peroxyacetyl nitrates) (Seinfeld and Pandis, 1998).

Southern California is one of the most severely polluted regions in the United States, suffering from excessive tropospheric ozone pollution. The concurrent state-wide tightening of VOCs and NO_x emissions regulations have made great progress to reduce the maximum hourly average mixing ratios of ozone from 490 ppb to 140 ppb during the past 30-year period (California Air Resources Board, 2019). However, several studies (Gaudel et al., 2018; Jose Granados-Munõz & Leblanc, 2016) show the ozone concentration is continuing to increase. Despite significant regulatory efforts, in 2020 the South Coast Air Basin still experienced 142 days exceeding the daily maximum 8-hour average ozone National Ambient Air Quality Standard (NAAQS) (California Air

Resources Board, 2020). The challenge to understanding ozone pollution is linked to the photochemical reactions of various pollutant sources, and the complicated transport mechanism due to the terrain of California's South Coast Air Basin (SoCAB).

The challenge to reach attainment of the 8-hour ozone NAAQS using current control strategies motivates the need to reconsider mitigation scenarios. Comprehensive atmospheric models have contributed further insights through their prediction of the response of surface ozone to emissions control strategies. However, biases commonly exist between model simulated ozone and ground site measurements (J. J. Guo et al., 2018; Travis et al., 2016). Previous studies have found that complex patterns of vertical transport of ozone affect model simulation accuracy significantly (Akimoto et al., 2019; Fast et al., 2014; Lin & McElroy, 2010; Li & Rappenglueck, 2018).

Near-surface and aloft measurements are often used to quantify uncertainties in model simulations (Mena-Carrasco et al. 2007; Tang et al. 2017; Hu et al. 2012; Cuchiara et al. 2014). There have been dozens of large-scale campaigns in Southern California, including the Southern California Ozone Study (SCOS) and the California Research at the Nexus of Air Quality and Climate Change Study (CALNEX). In those and other previous studies, the deployment of airborne instrumentation is limited in the research domain and duration, and generally restricted to heights of kilometer level. Recently, the surface to a few hundred-meter layer void is being filled with the development of unmanned aerial vehicle (UAV) technology for earth science applications. Chen et al., (2019) and Area et al., (2019) have carried out ozone vertical profile measurements using

UAVs over Shanghai and Amazonia urban areas, respectively. Their successful results highlight the value of UAV measurements for air composition characterization and vertical distribution assessment.

In this chapter, we will discuss the results from a 4-month-long daily campaign to measure UAV-based vertical profiles of ozone and particulate matter. The UAV was deployed from August to November 2020. Resulting are 327 vertical profiles from the surface to 500 m above ground level (AGL) collected in the early mornings and late afternoons when the atmosphere is generally most stratified. The measured ozone concentration profiles are statistically compared with monitoring station measurements and Community Multiscale Air Quality (CMAQ) model simulated results. The height of the top of the planetary boundary layer (PBL) estimated from a ceilometer is leveraged to help understand the potential contributors to CMAQ model bias related to vertical structure in meteorology. CMAQ sensitivities to factors such as PBL, eddy diffusivity, NO_x emissions, and VOC emissions are investigated due to their importance in vertical pollution profiles in the model.

2.2. Methods

2.2.1. Site Description

The city of Riverside is located in Southern California, approximately 80 km east of downtown Los Angeles. It has a population of 314,998 over an area of 211.17 km2. The mean accumulated precipitation from August to November in 2020 is 0 mm. The monthly mean surface air temperature during the measurement period is between 17.72 °C and

26.22 °C. The launch site (Figure 2-1) is inside the University of California, Riverside's Agricultural Operations research station in Riverside, CA (33.965083, -117.342417). The Agricultural Operations area is mainly covered by citrus trees and various other plants. The launch site is located in suburban Riverside and is approximately 1.2 km southwest of U.S. Interstate 215.Riverside is located in Southern California, about 80 km east of downtown Los Angeles. It has a population of 314,998 over an area of 211.17 km^2. The mean accumulated precipitation from August to November in 2020 is 0 mm, with the mean surface air temperatures between 17.72°C and 26.22°C. The launch site (shown in Figure 2-1) for the UAS used in the study is situated inside the Agricultural Operations Field at the University of California, Riverside in Riverside, CA (33.965083, -117.342417). The field is primarily composed of citrus trees and other vegetation and is situated approximately 1.2 km southwest of Interstate Highway 215.

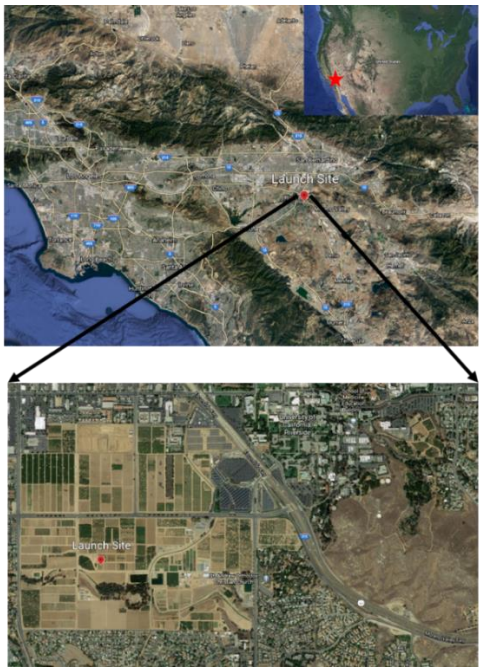

Figure 2-1 (Top) Satellite image of the launch site in Riverside, California, United States. (Bottom) Depiction of the launch site relative to the campus of University of California, Riverside, and the interstate highway 215.

2.2.2. Platform and Instrumentation

In this study, a customized hexacopter unmanned aerial vehicle Matrice 600 Pro (DJI Innovations, China) was used as the flight platform. It has a maximum flight duration of about 30 minutes with a maximum payload weight of 5 kg. Flight records including flight time, speed, altitude, latitude, and longitude information were retrieved from the DJI GO app.

A Personal Ozone Monitor (POM) (2B Technologies, Inc., Colorado, USA) was mounted inside an enclosure with a short, perfluoroalkoxy-lined inlet tubing with ¼" outside diameter, extending outside and underneath the UAV's body. The ultraviolet absorption-based POM has a precision of the higher of 1.5 ppb or 2% of the reading. POM's default

adaptive filter to average the data was turned off to obtain the raw data. The measurement time interval was set to be 2 s with a sampling flow rate of 0.8 L/min to obtain a better vertical resolution, which is estimated to be 1.2 m for the flight speed of 0.6 m/s. The raw data were averaged over a sliding window of length 30 across neighbouring elements, and outliers were removed.

Particulate matter concentration was measured using a commercially available MINIMA wearable sensor (Applied Particle Technology, California, USA). The MINIMA measured PM1, PM2.5, and PM10 every 15 s. The data were uploaded to its vendor-hosted web interface via a mobile hotspot in real-time.

Temperature and relative humidity measurements were collected using a Portable temperature and humidity data logger OM-141 (Omega Engineering Inc., Connecticut, USA). Its accuracy is ± 1.8°F (1°C) for temperatures ranging from 14° to 104°F (-10° to 40°C) and ± 3% for relative humidity ranging from 20 to 80%. The temperature and relative humidity data were used to validate modelled PBL heights. A Personal Ozone Monitoring (POM) (2B Technologies, Inc., Colorado, USA) was mounted inside an enclosure with a short PFA inlet tubing of ¼" OD extending outside under the UAS's body. The ultraviolet absorption-based ozone monitoring has a precision of 1.5 ppb or 2% of the reading. The instrument's default adaptive filter to average the data was set to be off to get the raw data. The measurement time interval was set to be 2 s at a sampling flow of 0.8 LPM to obtain a better vertical resolution, which was estimated to have a vertical resolution of 1.2 m for

the flight speed of 0.6 m/s. The raw data was moving averaged with a window size of 30 with the negative values and outliers were removed.

The particulate matter was measured using a commercially available MINIMA personal exposure particle sensor (Applied Particle Technology; APT, Missouri, USA). The monitoring measures PM1, PM2.5, and PM10 every 15 seconds. The data were uploaded to its vendor-hosted web interface via a mobile hotspot in real time.

The temperature and relative humidity measurements were conducted using a Portable Temperature and Humidity Data Logger OM-141 (Omega Engineering Inc., Connecticut, USA). Its accuracy is ±1°C from 10° to 40°C and ±3% from 20 to 80% RH. Its accuracy is ±1.8°F (1°C) from 14° to 104°F (-10° to 40°C) and ±3% from 20 to 80% RH. The temperature and relative humidity data were used to help validate PBL heights.

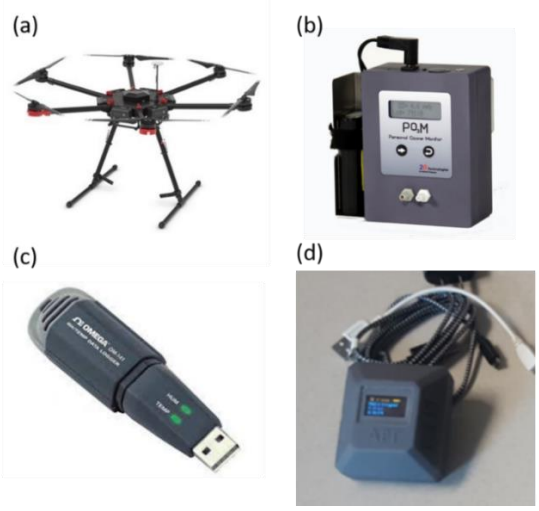

Figure 2-2 Pictures of (a) DJI Matrice 600 Pro, (b) Personal Ozone Monitoring (POM), (c) Portable Temperature and Humidity Data Logger OM-141, (d) MINIMA from Applied Particle Technology.

2.2.3. UAS Flights

Between 16 August and 30 November 2020, 376 profiles were measured. Routine flights were conducted every day both early in the morning around sunrise and late in the afternoon around sunset as permitted by weather conditions. The flight operation time is shown in Figure 2-3 with the sunrise and sunset time as references. The UAV was controlled using the DJI GO app to fly a round trip vertically to 500 meters above ground level at a constant vertical velocity of 0.6 m/s. The flights during the campaign were authorized by the Federal Aviation Administration (FAA). From August 1st to November 31st, 2020, a total of 376 profiles were obtained through daily routine flights conducted in the early mornings around sunrise and late afternoons around sunset, subject to favorable weather conditions. The UAS utilized the DJI GO app and flew a straight path vertically up to 500 meters above ground level at a constant speed of 0.6 m/s. The FAA approved all flights carried out during the campaign.

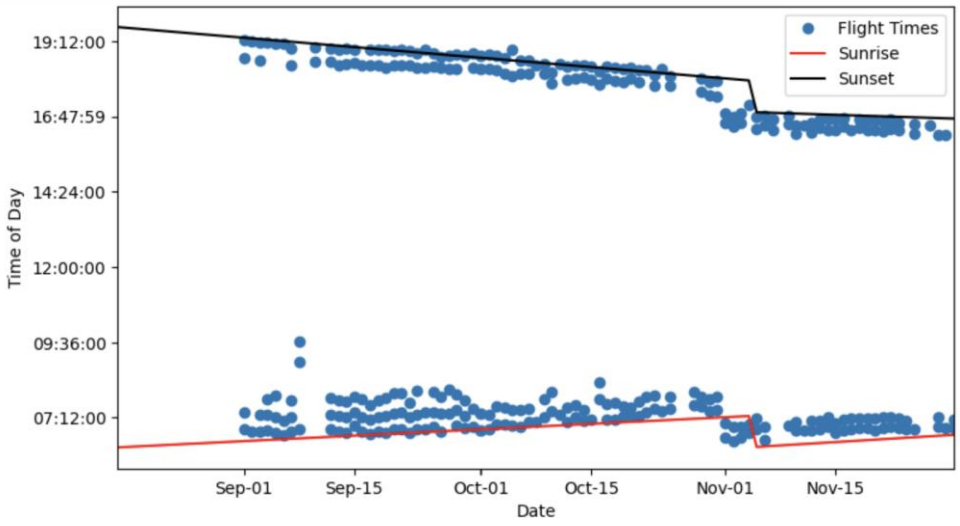

Figure 2-3 Flight time and sunrise/sunset time (PDT).

2.2.4. CMAQ Model Description

The Community Multiscale Air Quality (CMAQ) model was used to simulate vertical ozone profiles for comparison with flight measurements. We chose CMAQ, as it is widely used for NAAQS compliance purposes. CMAQ was used to simulate ozone mixing ratios for each day of August to November 2020. Baseline emissions were modified accordingly to capture the reductions in traffic during the lockdown periods of the COVID-19 pandemic. The model was compiled and run with the GFortran compiler on a dual Xeon workstation running the Ubuntu operating system. The model was run with a configuration provided by SCAQMD that has 4 km horizontal grid spacing and 11 vertical layers over SoCAB.

The SAPRC07tc_ae6_aq chemical mechanism option (SAPRC07tc photochemical mechanism, aerosol module 6, and aqueous chemistry) was used due to its relevance to Southern California NOx-VOC-ozone regimes. Gridded emission inputs of 73 air pollutants were provided as daily emission files with hourly temporal resolution. Details of the SAPRC-07 gas-phase mechanism and an overview of CMAQ's governing processes may be found in the works of William P.L. Carter and Byun and Schere, respectively (Carter 2010; Byun and Schere 2006). The Weather Research and Forecasting (WRF) model version 3.9 was used to generate meteorological inputs for the CMAQ simulations. The optimal WRF options for SoCAB are USGS land use, thermal diffusion surface layer scheme (Huang, Huang, and Huang 2014), and Yonsei University planetary boundary layer scheme (Hong, Noh, and Dudhia 2006). We combined

initialization data from the North American Mesoscale (NAM) Forecast System with NOAA high-resolution sea surface temperature (SST) nudging (Reynolds et al. 2007) to improve the accuracy of meteorological inputs.

The finest modeling domain has a horizontal grid spacing of 4 km (domain 3), covering fully the South Coast Air Quality Management District (SCAQMD) region (Figure 2-4), and domain 3 consisted of 156 x 102 grids nested one way within domains 1 (36 km) and 2 (12 km). More information on baseline model performance using this configuration can be found in a preceding study (Do et al., 2023).

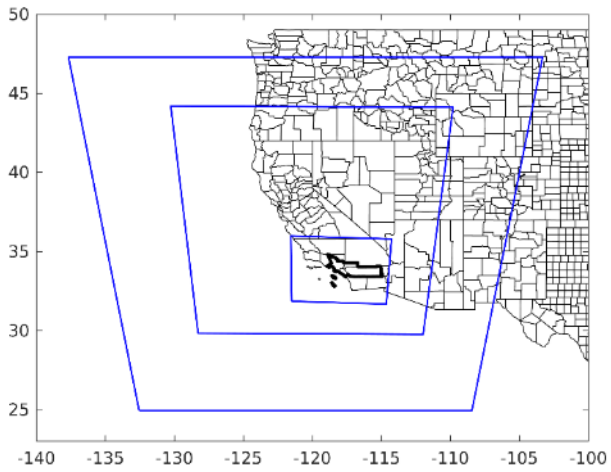

Figure 2-4 The map shows the target area SoCAB in thick black lines.

The 2020 emission correction was carried out using two-step calculations.

1st step: Estimating 2020 emissions from AQMD 2019 emissions and AQMD emission projection

The input emissions for CMAQ 2020 simulation were modified from the AQMD 2019 inventory. The linear correction factor (Eq. 1) was applied to 2019 emissions based on the AQMD emission projection from 2012 to 2034 to obtain 2020 estimated emissions.

$$Correction\ Factor = \frac{2020\ emis - 2019\ emis}{2019\ emis} \quad (1)$$

The correction factor was carried out for seven air pollutant groups (total organic gas, reactive organic gas, CO, NO_x, SO_x, NH_3, PM).

2nd step: Correcting for traffic reduction.

The lockdown due to the pandemic has shown great traffic reduction, especially from March to May 2020. AQMD projection did not consider the reduction in traffic which decreases mobile emissions. The weekly traffic change in 2020 was provided from the UCR emission group which recorded the weekly changes from January 1st to September 30th, 2020, for the total flow, flow change, speed change, and observed percent of 2991 locations in Southern California. Since the traffic data were not evenly distributed over the South Coast, we used K-Nearest Neighbors to obtain the traffic data for the grid cell (location) that had no more than 5 data points. For the grid cell that had more than 5 data points, we first normalized with the traffic volume and averaged the normalized traffic data.

2.2.5. Ground Observation Data

Ozone measurements from the South Coast Air Quality Management District (SCAQMD) Riverside-Rubidoux air monitoring site (33° 59' 58"N 117° 24' 57"W) for comparative analyses. The monitoring site is approximately 8 km northwest of the UAV launch site. Data were downloaded via the Air Quality and Meteorological Information System, which

is managed by the California Air Resources Board (CARB) (http://www.arb.ca.gov/aqmis2/aqdselect.php). Observed boundary layer heights are estimated using data from a ceilometer (Vaisala CL51, Vaisala Inc., Finland), also operated at the Riverside-Rubidoux air monitoring site. Boundary layer heights were assumed to be the height above ground level at which the negative gradient of the backscatter coefficient was greatest.

2.3. Results and Discussion

2.3.1. Vertical Profile Patterns

A total of 376 profiles were collected in this study. A representative profile for the morning flights is shown in Figure 2-5, with the steep increase in ozone mixing ratio by more than 60 ppb across 100 to 300 m in altitude indicating the boundary layer. The $PM_{2.5}$ and PM_{10} concentrations changed by 10 $\mu g/m^3$ at the same altitude range, while the change in PM_1 was not as pronounced.

Another representative example of the morning profile is shown in Figure 2-6. In this profile, the ozone mixing ratio shows a smooth change from about 20 ppb at the surface to over 80 ppb at 500 m AGL. This indicates an effective diffusivity when the ozone formation is slower than the depletion. The PM profiles show a similar trend to the preceding example, with $PM_{2.5}$ and PM_{10} both decreasing by about 10 $\mu g/m^3$ at the altitude range of 100 to 200 m.

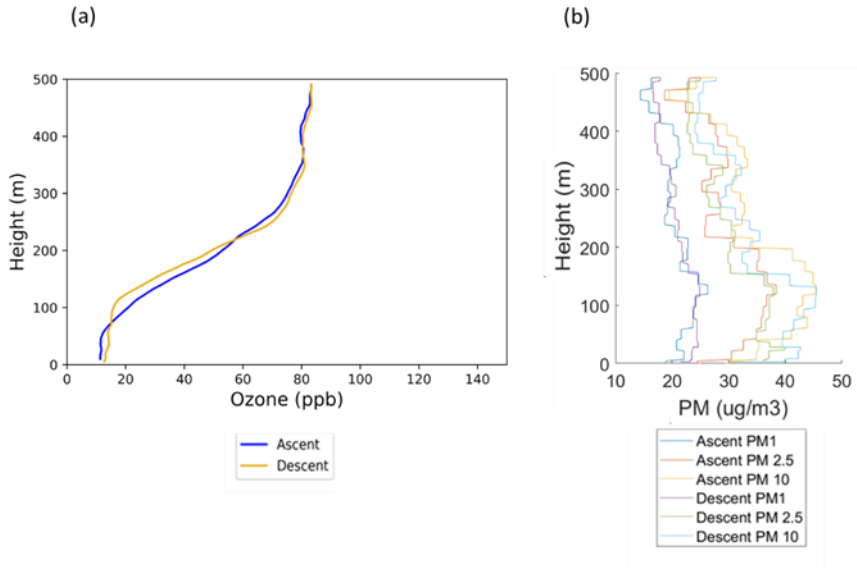

Figure 2-5 Vertical profiles of (a) ozone concentration, (b) PM1, PM 2.5 and PM 10 from surface to 500 m on 4 September 2020 at 7:48 (PDT).

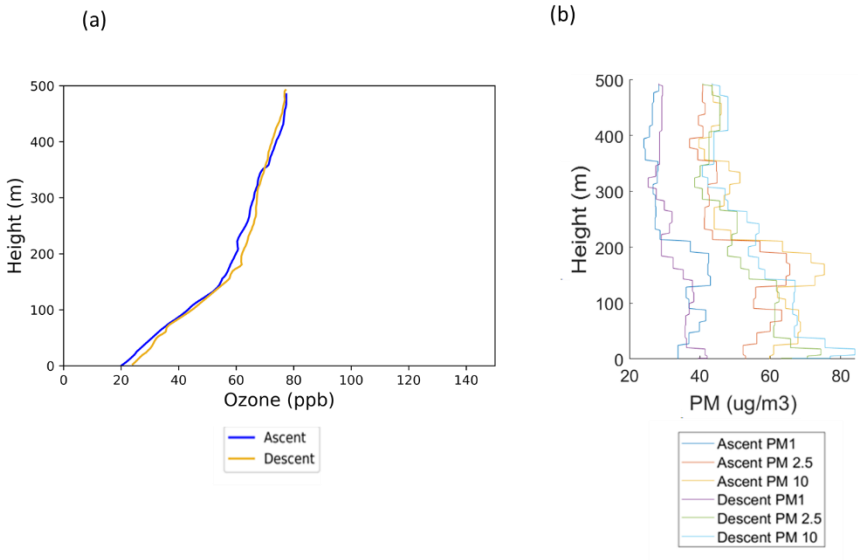

Figure 2-6 Vertical profiles of (a) ozone concentration, (b) PM1, PM 2.5 and PM 10 from surface to 500 m on 4 October 2020 at 6:59 (PDT).

Late afternoon profiles typically show no obvious ozone mixing ratio gradient. In the Figure 2-7 profiles, the ozone mixing ratio is nearly constant at 75 ppb from the surface

to 500 m AGL. This is believed to result from efficient vertical mixing accompanying boundary layer growth during the daytime. The $PM_{2.5}$ and PM_{10} profiles increased gradually by about 10 $\mu g/m^3$ with increasing altitude. The PM profiles show less sensitivity to the PBL height change compared to the ozone mixing ratio profiles in the above examples.

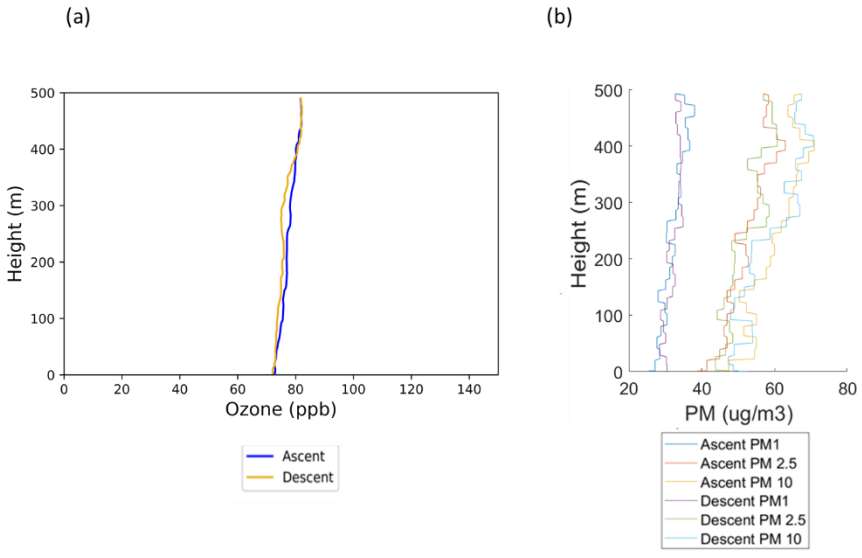

Figure 2-7 Vertical profiles of (a) ozone concentration, (b) PM1, PM 2.5 and PM 10 from surface to 500 m on 21 October 2020 at 17:54 (PDT).

2.3.2. Model Comparisons With the Ground and UAS Measurements

Ozone vertical profiles were compared to CMAQ simulated results and ground observations from the Riverside-Rubidoux air monitoring site. Figure 2-8a shows the UAV-measured data and the hourly simulated data plotted with the ground monitoring hourly data for the same period along with the linear regression fit. The average of the UAV measurements below 5 meters and CMAQ's bottom-most layer (height typically under 18 m above ground level) are considered to be the ground-level concentrations in

this analysis. The R^2 for the relationship between the UAV and monitoring site data (0.88) is higher than that for the relationship between the CMAQ and monitoring site data (0.66), suggesting a better accuracy with UAV measurement than CMAQ simulation. Compared with CMAQ, the UAV frequency distribution matches better with the ground monitoring observations (Figure 2-8b). The box plot in Figure 2-9 reveals that CMAQ is biased positively near the ground in this case. The gradient of the vertical profile in the simulation is smaller than that of the UAV observations.

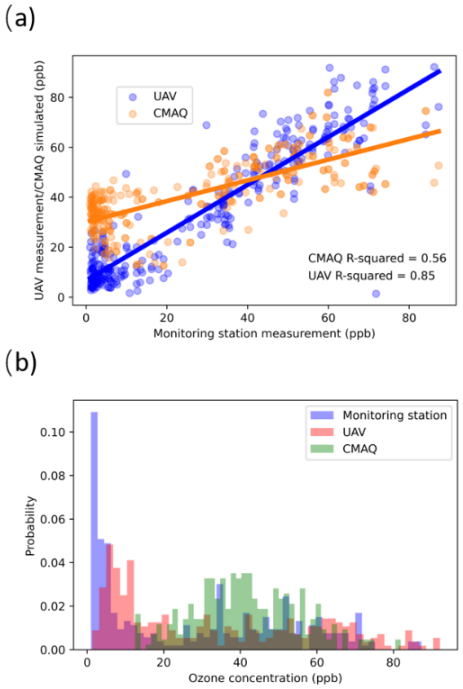

Figure 2-8 (a) The comparison of UAS measured and model simulation compared with the monitoring station data recorded at the same time. (b) The frequency distribution of the UAS measured and model simulation data compared with the monitoring station observations.

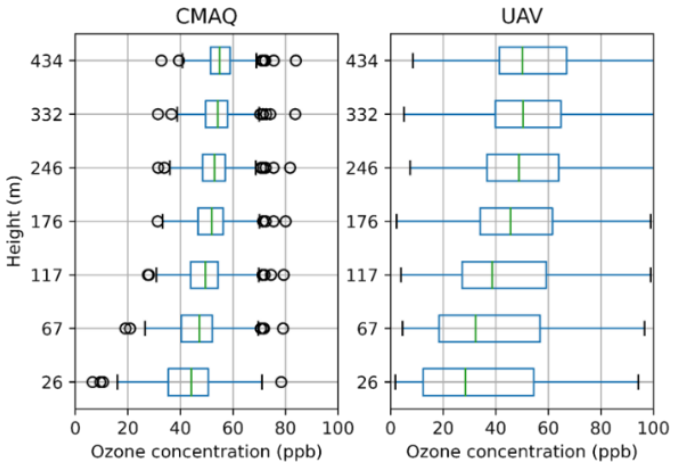

Figure 2-9 The comparison of UAS measured and model-simulated ozone concentration box plots. The centerline inside the box is the median, the left, and right of the box are the first and third quartiles, respectively, and the lower and upper whiskers are the range of the data. Outliers are plotted as separate dots.

2.3.3. Evaluation and Model Inter-Comparisons With Modifications

Ground-level ozone mixing ratio is influenced by local ozone production, chemical and depositional loss, and mixing in both horizontal and vertical directions. We posit that the bias from mixing in the vertical direction is mainly controlled by the model representations of the PBL. Ozone is formed via a series of photolytic reactions involving NO_x and VOCs. The daily maximum surface ozone mixing ratio varies nonlinearly with the precursor concentrations. This process is illustrated in Figure 2-10, highlighting the nonlinear relationship between the three compounds. Therefore, the sensitivity of modeled ozone mixing ratio to PBL, NO_x concentration, and VOC concentration is explored here by modifying key parameters: PBL height, eddy diffusivity, NO_x emissions, and VOC emissions.

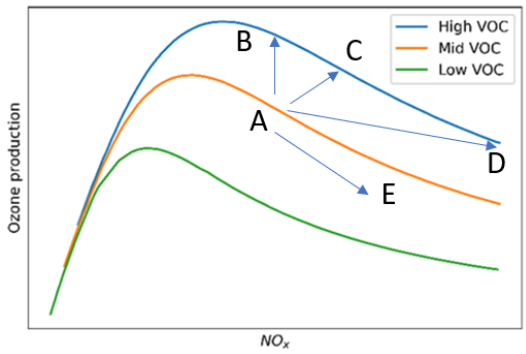

Figure 2-10 The ozone production as a function of NO_x concentration shown on three levels of VOC.

2.3.4. Impact of PBL Change on Ozone

The Yonsei University (YSU) planetary boundary layer scheme was used here as the baseline scheme to generate the original PBL. Figure 2-11 shows the default version of PBL height generated in WRF and the estimated PBL height using the ceilometer's backscatter coefficient measurements shown on the density graph. The PBL height is estimated to be where the backscatter coefficient's gradient is largest. For reference, a study based on over a decade-long dataset (Rahn and Mitchell 2016) measured the PBL height using commercial aircraft soundings at the Ontario International Airport approximately 25 km from the UAV measurement site. That study found a median PBL height of approximately 400 m in the early morning and 500 m in the late afternoon This agrees with the PBL heights estimated in this study using the ceilometer data; however, there were discrepancies in modeled PBL height determined by the YSU scheme.

As surface concentrations vary inversely with the PBL height, a lower PBL height would be associated with shallower vertical mixing and higher NO_x and VOC concentration. In the daytime, higher precursor concentrations will generally lead to increased ozone production, while higher NO_x concentration at night leads to overall consumption of ozone via the reaction between NO_x and O_3. PBL height was adjusted by applying a global correction factor to better reflect the ceilometer observations, which made the modeled PBL height higher in the nighttime and lower in the daytime. Compared to the default PBL scheme, the modified PBL height led to a 2-ppb increase and a 0.6 ppb increase in the mean ground-level ozone for morning and afternoon, respectively (Figure 2-12).

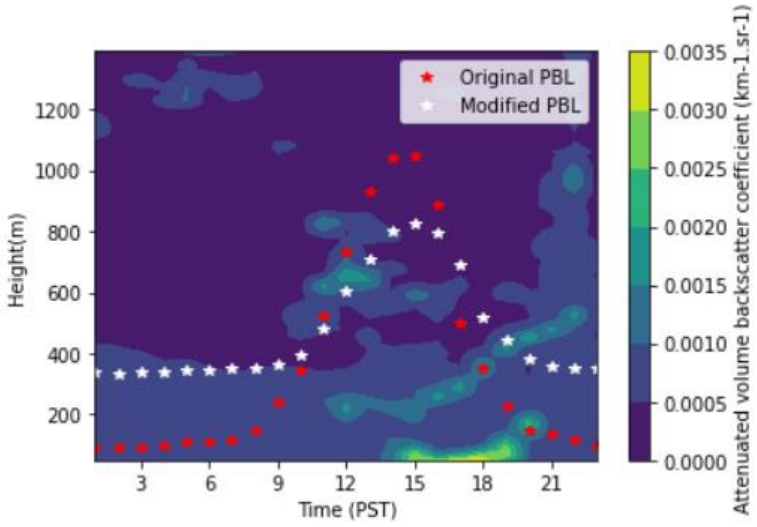

Figure 2-11 PBL default version of used in CMAQ (red stars) and modified PBL estimated using the ceilometer's backscatter coefficient measurement (white stars) averaged over the measurement time series.

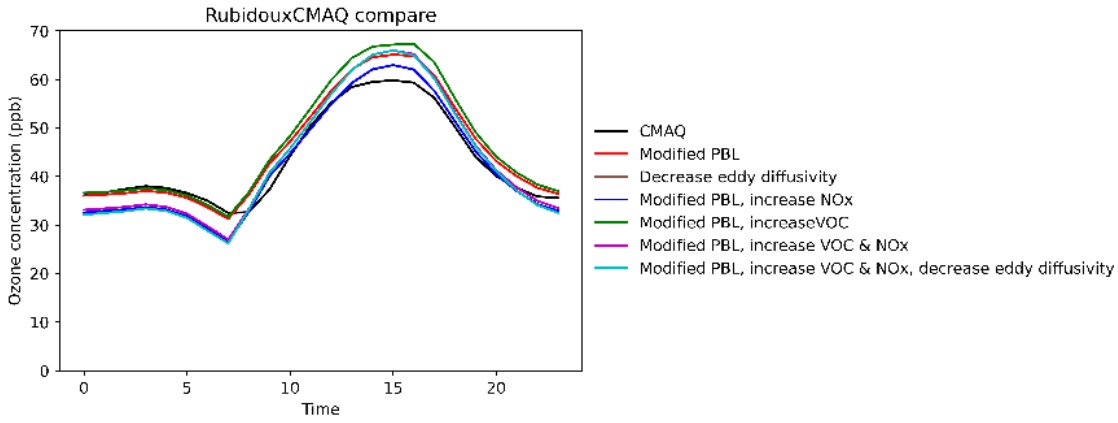

Figure 2-12 The averaged simulated ozone diurnal cycle at Rubidoux based on all measurement days.

2.3.5. Impact of Eddy Diffusivity Change on Ozone

Considering that the YSU scheme is based on bulk Richardson number rather than eddy diffusivity, to further examine the effect of vertical mixing in the model, we decreased the eddy diffusivity by 20%. The eddy diffusivity is expected to have a similar impact as the PBL height in that decreasing diffusivity would cause increases in ground-level precursor concentrations. The mean surface ozone mixing ratios were 1.8 and 0.2 ppb lower than the default version of the simulation in the morning and afternoon, respectively (Figure 2-13). The decrease in the afternoon ozone production is the result of the complex nonlinear dependencies of the ozone production on NO_x and VOC concentration. Referencing Figure 2-10, a 20% decrease in eddy diffusivity might lead to a more pronounced change in NO_x and VOC concentration (A → D). However, the modeled profile gradients in the morning still don't show much change due to the modification of diffusivity.

2.3.6. Impact of Emissions' Change on Ozone

Despite NO_x being a significant precursor of O_3, its increased concentration in the CMAQ simulation might have led to a decrease in simulated ozone mixing ratio due to the dual role of NO_x as both a precursor and a sink through NO_x titration, as well as the potential suppression of net O_3 formation caused by high NO_2 levels, which deflect the initial oxidation of VOC. By increasing NO_x emissions by 30% and retaining the PBL modification (Figure 2-10, A → E), the mean ground-level ozone mixing ratio decreased by 6.1 ppb and 3.1 ppb in the morning and afternoon, respectively, compared with the results from the PBL-only modification. The morning ozone reduction results from the enhanced NO_x titration at night. When nitric acid dominates the sink of odd hydrogen, OH decreases with increasing NO_x, and ozone production is weakened with less OH. When NO_x increases with constant VOC, the ozone production initially increases and then decreases in the high NO_x scenario (Figure 2-10).

Increasing VOC emissions by 30% with the modified PBL height increased the morning and afternoon ozone mixing ratio by 0.5 ppb and 2.6 ppb, respectively, compared with the results from the PBL-only modification. Ozone production increased with the increase of VOC at high NO_x but enhanced relatively low at low NO_x (Figure 2-10, A → B). In this case, the ozone formation is contributed mainly by the hydrocarbon-OH reactions that increase with increasing VOC emissions as opposed to NO_x having dual impacts.

Then we increased both NO_x and VOC emissions by 30% with the modified PBL height. The mean ozone ground mixing ratio decreased by 5.5 and 1.2 ppb in the morning and afternoon, respectively, compared with the results from the PBL-only modification. This result is the combination of all preceding scenarios (A → D). Ozone formation is favored by the VOC enhancement while weakened due to increased NO_x at the same time.

2.3.7. Combined Evaluation

Figures 2-13 and 2-14 present boxplot summaries for the UAV observations and model simulations in the mornings and afternoons for all scenarios, and the fractional bias between the UAV measurement and model simulations, respectively. The vertical gradients in the box plots don't change significantly with the change in PBL height. Note that the differences between the modifications are largest in the early morning (Figure 2-14). The variability in the ozone mixing ratio in the late afternoon is relatively small (Figure 2-14).

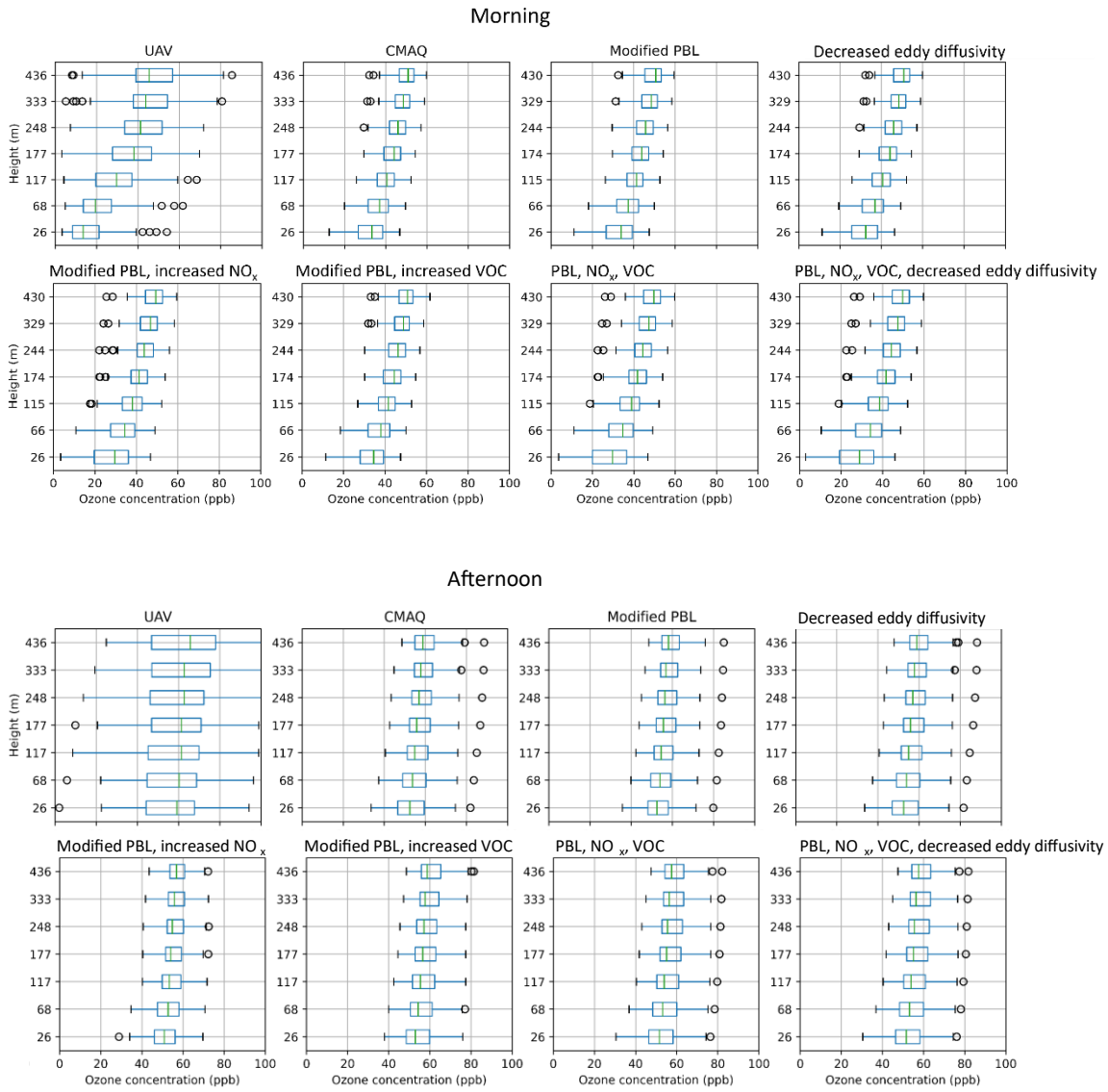

Figure 2-13. Comparison of UAV measured and model-simulated ozone mixing ratio for all modification scenarios.

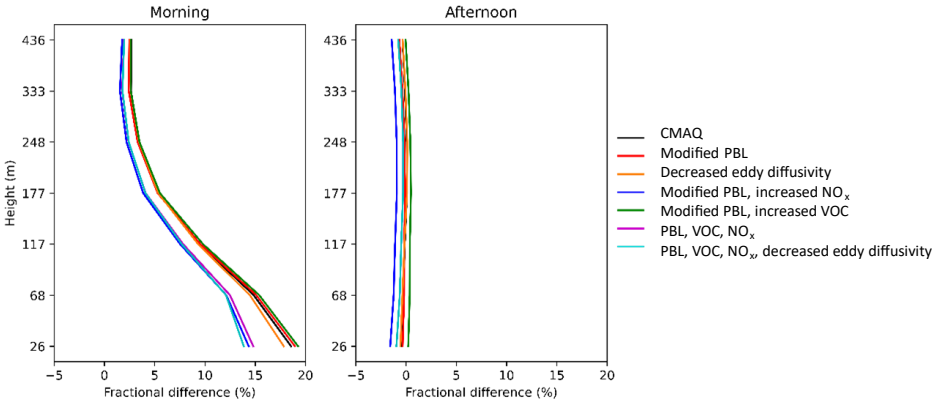

Figure 2-14. Fractional bias (%) between the UAV measurements and modeled ozone profiles. Results are averaged over all profiles.

All the simulations have poor performance for ground-level ozone mixing ratio in the morning and better performance at all heights in the afternoon (Figure 2-14). Among all the modifications, that which combined modifying PBL, decreasing eddy diffusivity, and increasing NO_x and VOCs led to the lowest fractional bias of 13.9% for ground-level ozone in the morning. However, these modifications rank the second worst for the fractional difference of -0.9% in the afternoon. The modified PBL and increased VOC simulation has the lowest ground-level fractional bias of 0.2% in the afternoon, while it has the largest ground-level fractional bias of 19.6% in the morning. This suggests that morning mixing conditions did not have a strong influence on the afternoon concentrations.

We also compared the frequency distribution of NO_x concentration extracted from the model and that measured at the Rubidoux monitoring station (Figure 2-15). The median NO_x concentration increased after modifying PBL height, which agrees with the

enhanced mixing as expected. CMAQ underestimates NO_x concentration significantly even after increasing NO_x emissions by 30%. The median of the monitoring site observation is 5.1 ppb higher than the simulated NO_x in the default configuration of CMAQ. The underestimation of observed NO_x indicates the potential underestimation of emissions in the current inventory.

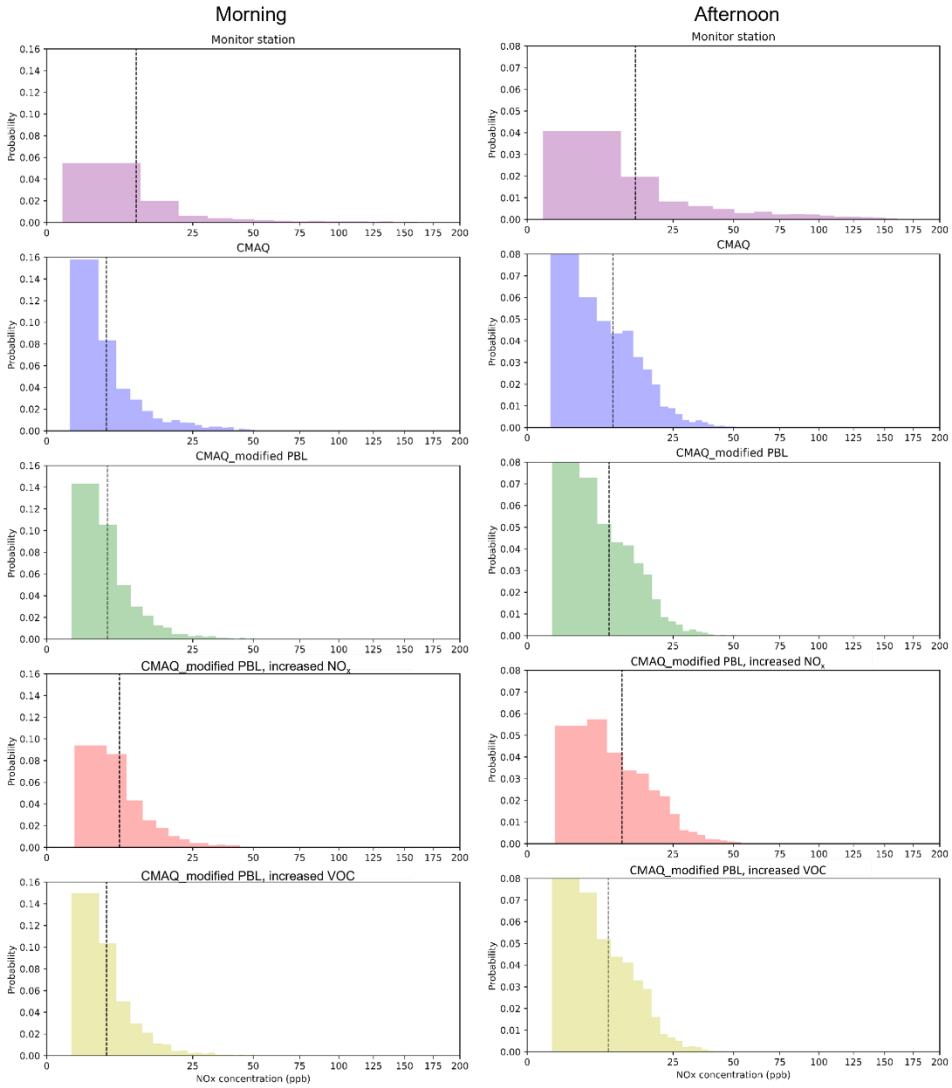

Figure 2-15. The frequency distribution of the NOx concentration of the Rubidoux monitoring station and the model simulations. The black vertical lines represent the median concentration of each case.

2.4. Conclusions

We completed a four-month field campaign where daily unmanned aerial vehicle (UAV) flights were made to measure vertical ozone and particulate matter profiles from the University of California, Riverside's Agricultural Operations Field from August to November 2020. Measured ozone mixing ratio was compared with the ground observations from the Rubidoux air monitoring site (SCAQMD) and with CMAQ model simulations. Vertical profiles captured the influence of the boundary layer in the early morning flights. UAV measurements at low altitude agreed well with the ground observations at the air monitoring site. However, CMAQ underestimated surface ozone by 11.2 ppb in the afternoon and overestimated it by 11.2 ppb in the morning. PBL height estimated from ceilometer data aided our understanding of the potential model biases due to meteorology. We conclude that vertical mixing within the PBL plays a large role in the surface ozone mixing ratio diurnal cycle. The PBL height observations from the ceilometer were lower in daytime and higher in nighttime compared with the modeled PBL height. The model simulation had a larger bias near the ground than aloft. We performed a sensitivity analysis to NO_x and VOC emissions. We found that an increase in NO_x emission by 30% reduced surface ozone mixing ratios by 6.1 and 3.1 ppb in the morning and afternoon, respectively. The extracted NO_x concentrations from the model were 5.1 ppb lower than ground observations on average. Inversely, ozone mixing ratios increased with increasing VOC emissions. Surface mean ozone mixing ratio was 0.5 ppb and 2.6 ppb higher in the morning and afternoon, respectively, after increasing VOC

emission by 30%. Increasing NOx and VOC emissions by 30% decreases ozone by 5.5 and 1.2 ppb in the morning and afternoon, respectively. This study highlights that model biases are related to a combination of meteorological and emissions uncertainties over complex terrain. Future modeling studies may benefit from high temporal resolution vertical measurements near the surface, such as those provided by UAV platforms, to closely evaluate model performance and increase model accuracy in heavily burdened air basins.

2.5. References

Abbafati, Cristiana, Kaja M. Abbas, Mohsen Abbasi-Kangevari, Foad Abd-Allah, Ahmed Abdelalim, Mohammad Abdollahi, Ibrahim Abdollahpour, et al. 2020. "Global Burden of 87 Risk Factors in 204 Countries and Territories, 1990–2019: A Systematic Analysis for the Global Burden of Disease Study 2019." *The Lancet* 396 (10258): 1223–49. https://doi.org/10.1016/S0140-6736(20)30752-2.

Akimoto, Hajime, Tatsuya Nagashima, Jie Li, Joshua S. Fu, Dongsheng Ji, Jiani Tan, and Zifa Wang. 2019. "Comparison of Surface Ozone Simulation among Selected Regional Models in MICS-Asia III - Effects of Chemistry and Vertical Transport for the Causes of Difference." *Atmospheric Chemistry and Physics* 19 (1): 603–15. https://doi.org/10.5194/acp-19-603-2019.

Area, Urban, Jianhuai Ye, Carla Batista, Rafael Barbosa, and Igor Ribeiro. n.d. "Vertical Profiles of Ozone Concentration Collected by an Unmanned Aerial Vehicle and the Mixing of the Nighttime Boundary Layer over an Amazonian," 1–14.

Byun, Daewon, and Kenneth L. Schere. 2006. "Review of the Governing Equations, Computational Algorithms, and Other Components of the Models-3 Community Multiscale Air Quality (CMAQ) Modeling System." *Applied Mechanics Reviews*. https://doi.org/10.1115/1.2128636.

C., Anenberg Susan, Horowitz Larry W., Tong Daniel Q., and West J Jason. 2010. "An Estimate of the Global Burden of Anthropogenic Ozone and Fine Particulate Matter on Premature Human Mortality Using Atmospheric Modeling." *Environmental Health Perspectives* 118 (9): 1189–95. https://doi.org/10.1289/ehp.0901220.

Carter, William P.L. 2010. "Development of the SAPRC-07 Chemical Mechanism." *Atmospheric Environment*. https://doi.org/10.1016/j.atmosenv.2010.01.026.

Chen, Qian, Dongsheng Wang, Xiaobing Li, Bai Li, Ruifeng Song, Hongdi He, and Zhongren Peng. n.d. "Vertical Characteristics of Winter Ozone Distribution within the Boundary Layer in Shanghai Based on Hexacopter Unmanned Aerial Vehicle Platform."

Cuchiara, G. C., X. Li, J. Carvalho, and B. Rappenglück. 2014. "Intercomparison of Planetary Boundary Layer Parameterization and Its Impacts on Surface Ozone Concentration in the WRF/Chem Model for a Case Study in Houston/Texas." *Atmospheric Environment* 96: 175–85. https://doi.org/10.1016/j.atmosenv.2014.07.013.

Fast, J. D., J. Allan, R. Bahreini, J. Craven, L. Emmons, R. Ferrare, P. L. Hayes, et al. 2014. “Modeling Regional Aerosol and Aerosol Precursor Variability over California and Its Sensitivity to Emissions and Long-Range Transport during the 2010 CalNex and CARES Campaigns.” *Atmospheric Chemistry and Physics* 14 (18): 10013–60. https://doi.org/10.5194/acp-14-10013-2014.

Gaudel, A., O. R. Cooper, G. Ancellet, B. Barret, A. Boynard, J. P. Burrows, C. Clerbaux, et al. 2018. “Tropospheric Ozone Assessment Report: Present-Day Distribution and Trends of Tropospheric Ozone Relevant to Climate and Global Atmospheric Chemistry Model Evaluation.” *Elementa* 6 (May). https://doi.org/10.1525/elementa.291.

Guo, Jean J., Arlene M. Fiore, Lee T. Murray, Daniel A. Jaffe, Jordan L. Schnell, Charles T. Moore, and George P. Milly. 2018. “Average versus High Surface Ozone Levels over the Continental USA: Model Bias, Background Influences, and Interannual Variability.” *Atmospheric Chemistry and Physics* 18 (16): 12123–40. https://doi.org/10.5194/acp-18-12123-2018.

Guo, Yitian, Jingwei Zhang, Junling An, Yu Qu, Xingang Liu, and Yele Sun. 2020. “Effect of Vertical Parameterization of a Missing Daytime Source of HONO on Concentrations of HONO , O 3 and Secondary Organic Aerosols in Eastern China” 226 (June 2019). https://doi.org/10.1016/j.atmosenv.2019.117208.

Hong, Song You, Yign Noh, and Jimy Dudhia. 2006. “A New Vertical Diffusion Package with an Explicit Treatment of Entrainment Processes.” *Monthly Weather Review*. https://doi.org/10.1175/MWR3199.1.

Hu, Jianlin, Cody J. Howard, Frank Mitloehner, Peter G. Green, and Michael J. Kleeman. 2012. “Mobile Source and Livestock Feed Contributions to Regional Ozone Formation in Central California.” *Environmental Science and Technology* 46 (5): 2781–89. https://doi.org/10.1021/es203369p.

Huang, Melin, Bormin Huang, and Allen H. Huang. 2014. “Implementation of 5-Layer Thermal Diffusion Scheme in Weather Research and Forecasting Model with Intel Many Integrated Cores.” In *High-Performance Computing in Remote Sensing IV*. https://doi.org/10.1117/12.2069426.

Jerrett, Michael, Richard T. Burnett, C. Arden Pope, Kazuhiko Ito, George Thurston, Daniel Krewski, Yuanli Shi, Eugenia Calle, and Michael Thun. 2009. “Long-Term Ozone Exposure and Mortality.” *New England Journal of Medicine* 360 (11): 1085–95. https://doi.org/10.1056/nejmoa0803894.

Jose Granados-Munõz, Maria, and Thierry Leblanc. 2016. “Tropospheric Ozone Seasonal and Long-Term Variability as Seen by Lidar and Surface Measurements at the JPL-Table Mountain Facility, California.” *Atmospheric Chemistry and Physics* 16 (14): 9299–9319. https://doi.org/10.5194/acp-16-9299-2016.

Li, Xiangshang, and Bernhard Rappenglueck. 2018. “A Study of Model Nighttime Ozone Bias in Air Quality Modeling.” *Atmospheric Environment* 195 (September): 210–28. https://doi.org/10.1016/j.atmosenv.2018.09.046.

Lin, Jin-Tai, and Michael B. McElroy. 2010. “Impacts of Boundary Layer Mixing on Pollutant Vertical Profiles in the Lower Troposphere: Implications to Satellite Remote Sensing.” *Atmospheric Environment* 44 (14): 1726–39. https://doi.org/10.1016/j.atmosenv.2010.02.009.

Mena-Carrasco, Marcelo, Youhua Tang, Gregory R. Carmichael, Tianfeng Chai, Narisara Thongbongchoo, J. Elliott Campbell, Sarika Kulkarni, et al. 2007. “Improving Regional Ozone Modeling through Systematic Evaluation of Errors Using the Aircraft Observations during the International Consortium for Atmospheric Research on Transport and Transformation.” *Journal of Geophysical Research* 112 (D12): D12S19. https://doi.org/10.1029/2006JD007762.

Rahn, David A., and Christopher J. Mitchell. 2016. “Diurnal Climatology of the Boundary Layer in Southern California Using AMDAR Temperature and Wind Profiles.” *Journal of Applied Meteorology and Climatology* 55 (5): 1123–37. https://doi.org/10.1175/JAMC-D-15-0234.1.

Reynolds, Richard W., Thomas M. Smith, Chunying Liu, Dudley B. Chelton, Kenneth S. Casey, and Michael G. Schlax. 2007. “Daily High-Resolution-Blended Analyses for Sea Surface Temperature.” *Journal of Climate*. https://doi.org/10.1175/2007JCLI1824.1.

Stocker, Thomas F., Dahe Qin, Gian Kasper Plattner, Melinda M.B. Tignor, Simon K. Allen, Judith Boschung, Alexander Nauels, Yu Xia, Vincent Bex, and Pauline M. Midgley. 2013. “Climate Change 2013 the Physical Science Basis: Working Group I Contribution to the Fifth Assessment Report of the Intergovernmental Panel on Climate Change.” *Climate Change 2013 the Physical Science Basis: Working Group I Contribution to the Fifth Assessment Report of the Intergovernmental Panel on Climate Change* 9781107057: 1–1535. https://doi.org/10.1017/CBO9781107415324.

Tang, Guiqian, Xiaowan Zhu, Jinyuan Xin, Bo Hu, Tao Song, Yang Sun, Jinqiang Zhang, et al. 2017. “Modelling Study of Boundary-Layer Ozone over Northern

China - Part I : Ozone Budget in Summer" 187: 128–37. https://doi.org/10.1016/j.atmosres.2016.10.017.

Travis, Katherine R., Daniel J. Jacob, Jenny A. Fisher, Patrick S. Kim, Eloise A. Marais, Lei Zhu, Karen Yu, et al. 2016. "Why Do Models Overestimate Surface Ozone in the Southeast United States?" *Atmospheric Chemistry and Physics* 16 (21): 13561–77. https://doi.org/10.5194/acp-16-13561-2016.

3. Toward On-Demand Measurements of Greenhouse as Emissions Using Multirotor Uncrewed Aircraft Systems

3.1. Introduction

Methane and carbon dioxide are potent greenhouse gases whose growing concentration in the atmosphere is contributing to climate change (IPCC, 2021). An important source for methane is anthropogenic activity including the production and transport of coal, natural gas and oil, livestock and other agricultural practices, land use and by the decay of organic waste in municipal solid waste landfills (US Environmental Protection Agency, 2023). To mitigate the effects of climate change, it is essential to develop dependable techniques for detecting, locating, quantifying and validating current emissions estimates. Instruments of various types have been widely employed to detect greenhouse gas emissions. Sensors and detectors are often used due to their relatively low cost and light weight, which makes them appropriate for handheld use or installation on mobile platforms (Aldhafeeri et al., 2020; Fox et al., 2019; Iwaszenko et al., 2021). However, compared to more advanced analytical instruments, sensors and detectors typically offer limited accuracy and precision. Additionally, they are more susceptible to interference from other gases, fluctuations in temperature or humidity, and other environmental factors that can affect their measurements. Generally, the accuracy of low-cost methane sensors/detectors can range from +/- 10% to 20% of the measured value. In contrast, more advanced instruments such as Tunable Diode Laser Absorption Spectroscopy (TDLAS) can achieve accuracies in the range of +/- 1% or less. A wide range of

advanced analyzers can be used to measure methane and carbon dioxide including Cavity Ring-Down Spectroscopy (CRDS) Analyzers, Tunable Diode Laser Absorption Spectroscopy (TDLAS), and Non-Dispersive Infrared (NDIR) Analyzers (Jha, 2022; McHale et al., 2016; So et al., 2020). However, these advanced instruments are often costly and bulky, which can make them less practical for use in the field or deployment on mobile platforms.

In addition to the accurate measurement, the meteorological variables also play an important role in estimating emission rate using dispersion models. Multirotor small unmanned aerial systems (UAS) offer a solution to this problem by providing the ability to sample emissions within the planetary boundary layer (PBL) covering the height range from the ground to a few hundred meters, which is hard to achieved using conventional methods such as tower installations or crewed aircrafts. They are also portable and can safely maneuverer near emission sources at low altitudes in both urban and rural environments. These characteristics are particularly advantageous for improving the spatial and temporal resolution of methane and carbon dioxide measurements at local (sub-1km) scales, which can lead to more reliable estimates of anthropogenic emission sources that are difficult or infeasible to measure directly.

Some studies (Demali, n.d.; Falabella et al., 2018; Golston et al., 2017; Wilkinson et al., 2018) have demonstrated the successful use of small onboard sensors to measure various gas species, such as CH_4 and CO_2. Typically, these sensors are desirable due to their light weight and ease of integration onto the aircraft. Several methods for sampling the

atmosphere have combined the capabilities of both multirotor UAS and ground-based instruments to achieve precise measurements of greenhouse gas emissions. One such approach involves capturing an air sample using Teflon bag at a high altitude using the multirotor UAS and subsequently analyzing it on the ground using sophisticated instruments (Li C, 2020). Other studies (Brosy et al., 2017; Shah et al., 2020) have attempted to directly measure the air composition by towing a ground-based gas analyzer's inlet with a multirotor UAS, eliminating the need to average air samples over time. However, the maximum altitude of such measurements is limited by the length of the analyzer's inlet. Therefore, further investigation is necessary to develop air sampling techniques that can provide improved temporal and spatial resolution for more accurate greenhouse gas emission characterization.

Aircore technology has the potential to offer more practical and effective techniques for combining ground instruments and multirotor UAS for atmospheric sampling of greenhouse gases. The Aircore system is a passive air sampling technology that was initially introduced to measure trace gas profiles (Karion et al., 2010). The system is made up of a tubing coil, and air samples are collected due to the pressure difference between the outside and inside of the inlet. This air sampling technology has been widely used on aircraft and weather balloons to complement in situ and remote observations. Despite its potential to increase the spatial and temporal resolution of greenhouse gases in the atmosphere, the integration of multirotor UAS and Aircore systems has not been extensively explored. To address this, Andersen et al., 2018 have developed a multirotor

UAS active Aircore system that draws air samples using a micro pump. This system consists of a 50-meter-long stainless-steel tube with a volume of 358 mL and is capable of measuring atmospheric mole fraction of CO_2, CH_4, and CO.

In this study, we developed a system that combines a multirotor UAS and an Aircore system to measure air composition and wind velocity profiles. The Aircore system was designed to collect air samples and measure CH_4 and CO_2 with a spatial resolution of 5 meters while flying at a rate of 0.5 m/s. The vehicle kinematics of the multirotor UAS were utilized to estimate wind speed and direction during steady ascending flight. We deployed this system to measure CH_4 and CO_2 emissions from dairy farm operations downwind. Our findings demonstrate that this multirotor UAS and Aircore system is an effective tool for tracking gas emissions.

3.2. Methods and Materials

3.2.1. Field Operations

From January 20th to 24th, 2020, a UAS-based Aircore system was utilized in the San Joaquin Valley of California to measure CH_4 and CO_2 emissions from dairy farm operations. Before each deployment, CH_4 and CO_2 concentrations were measured by driving downwind of both isolated and clustered dairy farm facilities, as shown in Figure 3-1a. This was done by placing the inlet of a cavity ring-down gas analyzer through the side window of a van driving below 20 miles per hour. The UAS-based Aircore system, shown in Figure 3-1b, was rapidly deployed within 5 minutes at locations where CH_4 or CO_2 significantly exceeded the background concentration level of approximately 2 ppm

for CH_4. The air sample collected onboard the Aircore was subsequently analyzed using the cavity ring-down gas analyzer upon landing. Wind velocity profiles were estimated offsite using flight data collected onboard the UAS autopilot and a kinematic vehicle motion model. Four flights were performed in total across the three identified CH_4 and CO_2 hotspots, as shown in Table 3-1. All four flights' observations were used to assess the UAS-based system's efficacy in measuring vertical greenhouse gas emissions from dairy farm operations.

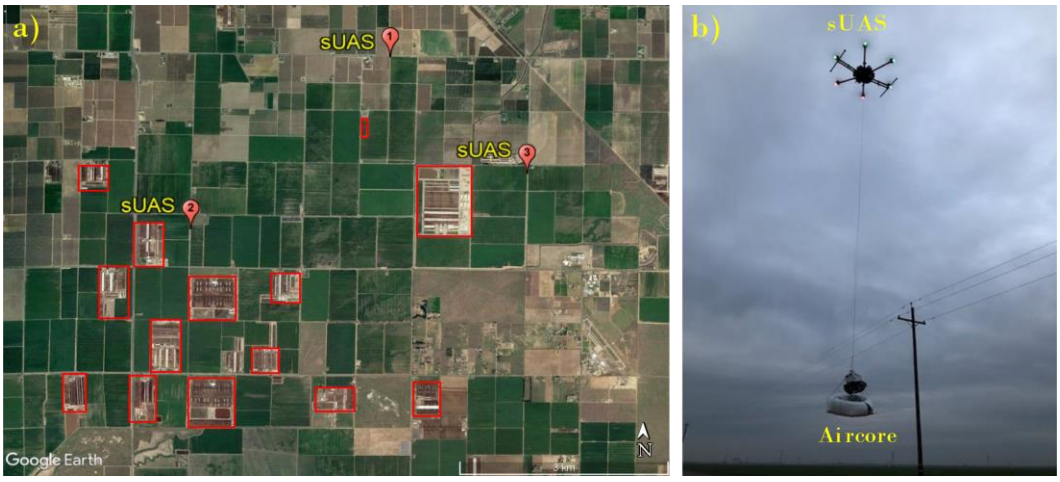

Figure 3-1 a) A satellite image showing the locations where multirotor UAS flight operations were performed to measure wind velocity and air composition vertical profiles on January 20th, 21st, and 24th, 2020. b) An image of the UAS-based Aircore system profiling air composition while steadily ascending to 120 m above ground level.

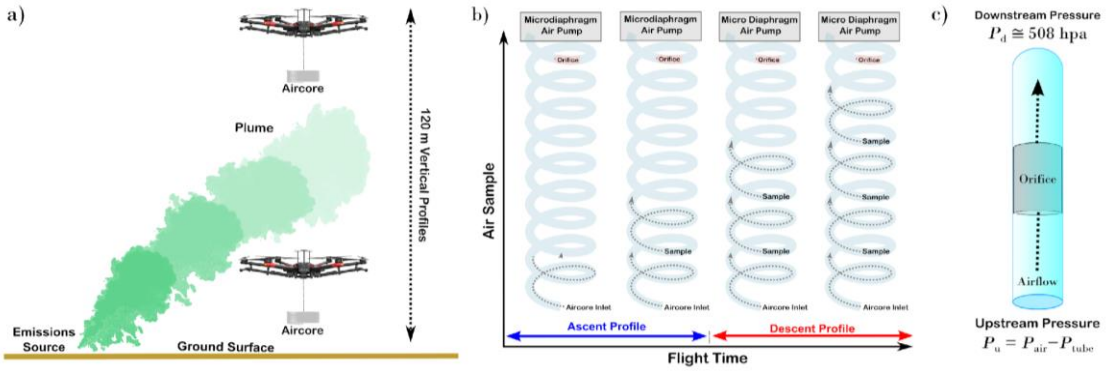

Figure 3-2 a) An illustration of the vertical flight operation. b) The process of the Aircore system pulling samples. C) The inner structure of the Aircore.

Table 3-1 Summary of multirotor UAS and Aircore flight operations conducted in the San Joaquin Valley, California in January.

Date	Pacific Standard Time	Latitude	Longitude
January 20th, 2020	9:54 AM – 10:06 AM	36°29'14.28"N	119°21'11.88"W
January 21st, 2020	15:54 PM – 16:05 PM	36°27'49.32"N	119°23'7.44"W
January 21st, 2020	16:23 PM – 16:33 PM	36°27'49.32"N	119°23'7.44"W
January 24th, 2020	16:38 PM – 16:48 PM	36°28'16.68"N	119°19'52.68"W

3.2.2. Ground-Based Meteorological and Gas Sensors

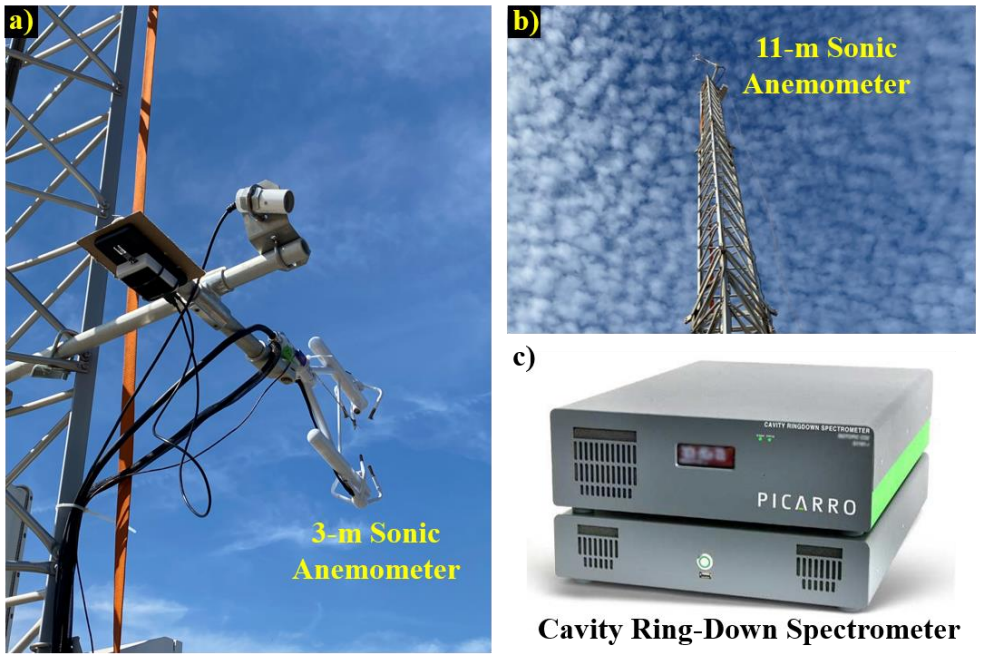

Figure 3-3 The a) and b) images show the CSAT-3 sonic anemometers installed on a meteorological evaluation tower at heights of 3 m and 11 m above ground level, respectively. The c) image shows the Picarro G1301 gas analyzer used to measure CH_4 and CO_2 concentrations of Aircore samples.

3.2.2.1. Cavity Ring-Down Spectrometer

The cavity ring-down spectrometer (CRDS) used to measure CH_4, CO_2, and water vapor is the Picarro G1301 gas analyzer (Figure 3-3c). It was housed inside a passenger van vehicle. Power was supplied to the instrument using a standalone 12-Volts marine deep cycle battery. The instrument's flow rate was measured to be 0.7 standard litres per minute.

3.2.2.2. Meteorological Evaluation Tower

A meteorological evaluation (MET) tower was deployed at a dairy farm to measure wind velocity near the surface (36°24'45.5"N 119°20'42.0"W). As shown in Figures 3-2a and 3-2b, the meteorological evaluation tower was integrated with two CSAT 3 sonic anemometers at heights of 3 m and 11 m above ground level. A CR3000 data logger was used to collect and process 1-second and 5-minute sonic anemometer measurements. The sonic anemometers and data loggers were both powered using a 12-V marine deep-cycle battery.

3.2.3. Aircore System

3.2.3.1. Multirotor UAS

The UAS used in this study was a commercially available multicopter Matrice 600 Pro (SZ DJI Technology, China). It was of 1668 mm × 1518 mm × 727 mm with a maximum take-off payload weight of 6 kg. With the Aircore of about 5 kg, the maximum flight time is about 13 min, corresponding to a mean fly speed of about 0.3 m/s. The Aircore was attached to the bottom frame of the UAS using a stainless-steel wire of about 5 m. The flight record including fly speed, height, time, GPS information, motion perturbations information is logged on-board automatically. The DJI GO app (SZ DJI Technology, China) was used for remote control and retrieve flight records.

3.2.3.2. Hardware Description

The Aircore system consists of a ~ 60 m perfluoroalkoxy (PFA) coil tubing with a 12.7 mm outer diameter (9.525 mm inner diameter) and a volume of 4.3 L. The inlet of the

coil is open to the ambient to sample emissions. The outlet of the coil is connected to a micro diaphragm pump. Airflow through the Aircore is held constant using an orifice (O'Keefe Controls Co.) installed upstream of the micro diaphragm pump. The pressure upstream of the orifice is the ambient pressure minus the small pressure drop through the tube. The pump and its battery are placed in a plastic enclosure.

3.2.3.3. Aircore Calibration Experiments

Laboratory tests were conducted to validate the Aircore's performance resolving real-time methane concentration change. We diluted CH_4 from a 500-ppm cylinder with room air in a Teflon bag. A three-way valve was controlled to switch between the CH_4 signals and the ambient air. The Aircore system and a Picarro Analyzer were connected using a tee junction to pull air simultaneously from the Teflon bag, with the valve open for 5 and 10 second intervals as shown in Figure 3-4. The CRDS analyzer recorded the methane concentration in real time during the calibration experiment. Subsequently the needle valve was closed to allow the CRDS analyzer to only pull from the Aircore.

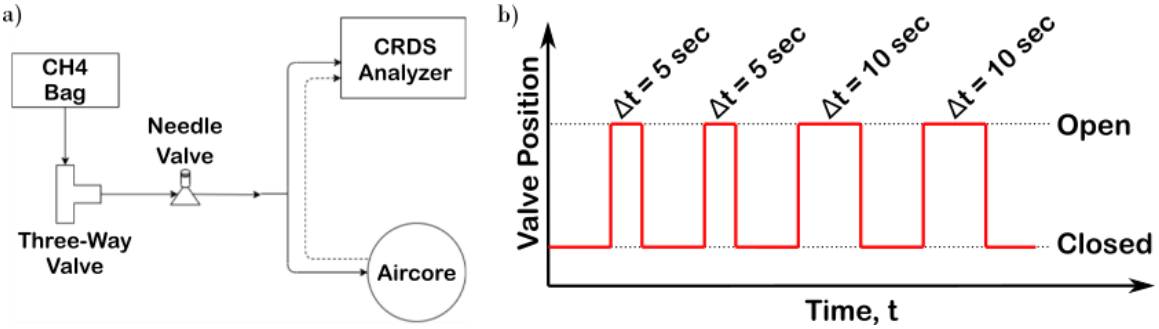

Figure 3-4 A schematic of the setup used during the Aircore calibration experiments. The solid lines and arrows show the gas flow when the Picarro analyzer and Aircore pulled air simultaneously. The dashed lines and arrows showed the gas flow when the Picarro analyzer pulled air from the Aircore system. b) A schematic showing the needle valve position over time during the Aircore calibration experiment.

3.2.4. Multirotor UAS Wind Velocity Sensing

3.2.4.1. Wind Estimation Method

Wind velocity profiles were inferred from the rotational kinematics of a multirotor UAS in steady-ascending vertical flight using the wind estimation algorithm proposed by Neuman et al. (2011). We first defined a body-fixed reference frame, $F_b = \{b_1, b_2, b_3\}$ at the aircraft centre of gravity such that the unit vectors b_1 and b_2 point along the front and lateral sides of the vehicle, respectively. The unit vector b_3 is parallel to the propeller spin axis and points along the direction of the propulsive flow (see Figure 3-5). We also defined an inertial reference frame $F_i = \{i_1, i_2, i_3\}$, affixed to the Earth's surface such that the unit vectors i_1 and i_2 point in the North and East directions, respectively, and the i_3 unit vector points towards the Earth's centre. The orientation of the body-fixed reference frame is measured relative to the inertial reference frame using the roll-pitch-yaw Euler

angles, $\Theta = \{\phi, \theta, \psi\}$. After defining the body-fixed and inertial reference frames, two kinematic relationships were derived to infer wind speed and wind direction separately.

Wind speed estimates were inferred from the tilt of the aircraft that is realized in steady-ascending vertical flight to compensate for wind disturbances. The tilt of the multirotor UAS was determined by computing the dot product between i_3 and the projection of b_3 onto F_i,

$$\alpha = ([R^T(\phi, \theta) \cdot b_3] \cdot i_3) \quad \textbf{(3-1)}$$

Where

$$R(\phi, \theta) = (cos\ cos\ \theta\ \ 0\ \ sin\ sin\ \theta\ \ \ sin\ sin\ \theta\ \ sin\ sin\ \phi\ \ \ cos\ cos\ \phi\ \ \ cos\ cos\ \theta$$
$$sin\ sin\ \phi\ \ \ sin\ sin\ \theta\ \ cos\ cos\ \phi\ \ \phi\ \ \ cos\ cos\ \theta\ \ cos\ cos\ \phi\ ) \quad \textbf{(3-2)}$$

is the rotation matrix mapping b_3 from F_b to F_i. In employing this approach, we assume there is a one-to-one relationship between the tilt angle α and the horizontal wind speed (i.e., $\alpha = ||u + v||$).

The wind direction was inferred from the projection of the b_3 unit vector onto the $i_1 - i_2$ plane shown in Figure 3-5b during steady-ascending flight. If the aircraft heading is pointing North, wind direction is expressed in the inertial reference frame by computing the four-quadrant tangent inverse of the components of the b_3 unit vector projected onto the i_1 and i_2 unit vectors.

$$\beta = tan_4^{-1}\left(\frac{[R^T(\phi,\theta)\cdot b_3]\cdot i_2}{[R^T(\phi,\theta)\cdot b_3]\cdot i_1}\right) \quad (3\text{-}3)$$

Otherwise, wind direction is expressed in the Earth-fixed reference frame by making the following correction:

$$Wind\ Direction = \{\beta - \psi, \quad if\ \beta > \psi \quad \beta - \psi + 360, \quad if\ \beta < \psi$$

3.2.5. Evaluation of Multirotor UAS Wind Velocity Estimates

Multirotor UAS wind velocity estimates were validated employing two methods. First, we compared the multirotor UAS wind velocity estimates to wind velocity observations collected from the 11-m MET tower. The difference between multirotor UAS and MET tower wind observations was quantified using the mean absolute error metric. Second, we compared multirotor UAS wind speed estimates to wind speed profiles obtained from the wind power law described in Eq. (3-4)

$$U(Z_2) = U(Z_1) * \left(\frac{Z_2}{Z_1}\right)^{\alpha} \quad (3\text{-}4)$$

where $U(z_1)$ and $U(z_2)$ are the wind speeds at heights z_1 and z_2, respectively, and α is the wind shear exponent value obtained from sonic anemometer observations collected at $Z_1 = 3$ m and $Z_2 = 10$ m using Eq. (3-5)

$$\alpha = \frac{ln\ U(z_2) - ln\ U(z_1)}{ln\ z_2 - ln\ z_1} \quad (3\text{-}5)$$

Results from these two assessments are useful for cauterizing the multirotor UAS wind estimation performance.

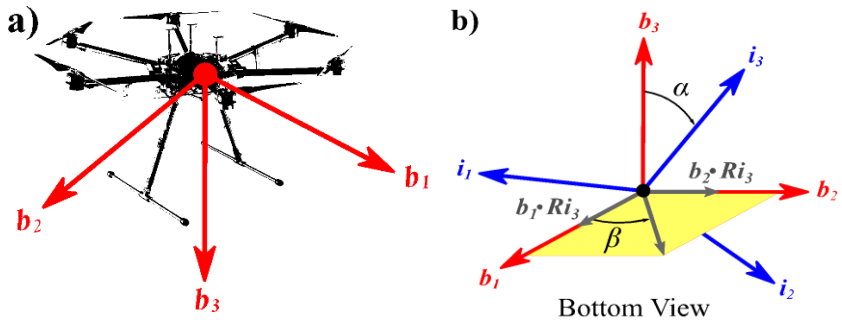

Figure 3-5 a) A schematic showing the configuration of the body-fixed reference unit vectors b_1, b_2, and b_3, relative to the front, right, and bottom sides of the multirotor sUA airframe. b) A schematic showing how the orientation of the body-fixed reference frame relative to the inertial reference frame is used to measure the α and β parameters used to estimate wind speed and wind direction separately.

3.2.6. Methane Emission Estimates

The multirotor UAS vertical profiles of wind velocity and methane concentrations that were collected from 9:54 AM to 10:05 AM on January 20th, 2020, were used along with an atmospheric dispersion model to quantify methane emissions from a dairy farm located near Visalia, California. The multirotor UAS vertical profiles of wind velocity and methane were measured 1,700 m Northwest from the midpoint of dairy farm's north end during a period in which the wind direction changed from North to South, allowing the downwind and upwind profiles to be collected from a single flight. The dairy farm involved in this study is 800 m wide and 933 m long, and consists of five manure lagoons, three cattle corrals, and three cattle sheds, with dimensions listed in Table 3-2. We divided the dairy farm into eleven sections that were expected to be methane emission sources to estimate the surface area of the dairy farm emitting methane into the atmosphere. Surface area estimates and multirotor UAS vertical profiles of wind velocity

and methane were used to evaluate the utility of multirotor UAS and Aircore technology for quantifying emission estimates at facility scale.

Table 3-2 Dairy farm sections likely to produce methane emissions from enteric fermentation or manure management.

Source Areas	Source Width	Source Length	Source Descriptor
Manure Lagoon	149 m	273 m	L1
Manure Lagoon	149 m	51 m	L2
Manure Lagoon	149 m	60 m	L3
Manure Lagoon	149 m	56 m	L4
Manure Lagoon	149 m	58 m	L5
Free Standing Shed	106 m	152 m	FS1
Free Standing Shed	106 m	152 m	FS2
Free Standing Shed	213 m	494 m	FS3
Free Standing Shed	88 m	137 m	FS4
Cattle Corral	152 m	342 m	C1
Cattle Corral	119 m	495 m	C2
Cattle Corral	119 m	495 m	C3
Miscellaneous	56 m	139 m	MC
Milk Parlour	28 m	145 m	MP
Total Source Area	1,732 m	3,049 m	TSA

3.2.6.1. Dispersion Model Methane Emission Estimates

The unknown emission rate from the dairy can be estimated from atmospheric CH_4 observations (CH_4) through the following relationship.

$$CH_{4i} = \sum T_{ij} E_j + C_b + \varepsilon_i \quad (3\text{-}4)$$

where T_{ij} is the model estimates on data point i with unit emission at source j, ε_i is the residual, C_b is the background concentration measured from sUAS and E_j is the inferred emission rate obtained by minimizing $\sum \varepsilon_i^2$ with the constraint that their values are greater than or equal to zero. To achieve this, we use the MATLAB function *lsqnonneg*

described in Lawson and Hanson (1995, Solving Least Squares Problems, Prentice-Hall, 1974, Chapter 23, p. 16). The 95% confidence intervals for the emission rate can be determined by a bootstrapping method which generates a distribution of emission rates by fitting the pseudo-observations to the model estimates.

In the numerical model, the dairy farm can be treated as an area source, which consists of a set of line sources perpendicular to the wind direction. The contribution from each line source to the receptor, we use an analytical approximation to the integral along the source (Venkatram & Horst, 2006), which gives the concentration as

$$C(x,y,z) = q[erf(t_1) - erf(t_2)]F_z(x,z) \tag{3-5}$$

$$t_i = \frac{y - y_i}{\sqrt{2}\sigma_y x}$$

where q is the line source emission rate per unit length, x is the downwind distance of the receptor from the source, $y - y_i$ is the distance of the receptor from two end points of the line along the direction parallel to the source, σ_y is the horizontal plume spread, and $F_z(x,z)$ is the vertical distribution function, which applied the numerical solution of the mass conservation equation(Venkatram & Schulte, 2018)

$$U(z)\frac{\partial C}{\partial x} = \frac{\partial}{\partial z}\left(K(z)\frac{\partial C}{\partial z}\right) \tag{3-6}$$

where C denotes the crosswind-integrated concentration $\underline{C}^y$ for convenience, $K(z)$ is the vertical eddy diffusivity, and $U(z)$ is the horizontal velocity. The boundary conditions are

$$K(z)\frac{\partial C}{\partial z} = 0 \; at \; z = z_0$$

and

$$\frac{\partial C}{\partial z} = 0 \; at \; z = H \tag{3-7}$$

where z_0 is the roughness length, which is computed to be 0.005m (Qian, Princevac, & Venkatram, 2010), H is the boundary layer height. The numerical method initializes a Gaussian concentration distribution at $x = 0$, which is centered at source height $z_s = 0.1m$ and with an initial vertical spread $\sigma_z = 0.1m$. Van Ulden, (1978) shows that the analytical solution of Eq. (3-2) provides an excellent description of concentrations measured in Prairie Grass (Barad, 1958). Venkatram & Schulte, (2018) evaluates the usefulness of the analytical formulas through the numerical solution using the Businger-Dyer expressions for eddy diffusivity of heat $K_H(z)$, and the wind profile $U(z)$.

3.3. Results

3.3.1. Multirotor UAS Wind Velocity and Air Composition Profiles

Four deployments of the UAS-based Aircore system were successfully performed downwind of dairy farm operations in the San Joaquin Valley. The UAS-based Aircore system measured vertical profiles of wind velocity, methane, and carbon dioxide up to a height of 120 m above ground level during periods of unstable and stable wind conditions. The first deployment on January 21st, 2020 experienced unstable wind conditions from 9:55 to 10:06 PST, while the second and third deployments on the same day and the fourth deployment on January 24th, 2020 experienced stable wind conditions (as shown in Figure 3-6 a,b,c). The data collected during both stable and unstable wind conditions were analyzed to evaluate the effectiveness of the UAS-based Aircore system in detecting and quantifying methane emissions from dairy farm operations.

During the first flight, the wind direction changed from South to North, with wind speeds ranging from 0 m/s to 3.5 m/s (as shown in Figure 3-6a). The methane and carbon dioxide concentrations measured during this flight varied from 2.5 ppm to 3 ppm below 60 m and remained constant at higher altitudes. During the second flight, the wind consistently blew from the southwest, with speeds ranging from 1 m/s to 2.5 m/s (as shown in Figure 3-6b). Comparing ascent and descent profiles during this flight revealed that methane concentrations varied from 2.5 ppm to 5 ppm, while carbon dioxide concentrations remained constant at 410 ppm. Minutes later, during the third flight, winds from the southwest ranging from 0.5 m/s to 1.5 m/s were measured at the same location (as shown in Figure 3-6c). Comparing ascent and descent profiles during this period showed that methane concentrations increased from 2.8 ppm to 5.8 ppm, while carbon dioxide concentrations increased from 410 ppm to 510 ppm. Pollution rose plots in Figures 3-7 suggest that the differences in methane profiles between the second and third flights may have been caused by plume meander resulting from minor changes in wind direction.

During the fourth flight, the wind consistently blew from the southeast, with speeds ranging from 1.5 m/s to 3 m/s (as shown in Figure 3-7d). The methane concentrations remained elevated by more than 5 ppm up to 100 m before tapering off at higher altitudes. A brief increase in carbon dioxide concentration of 100 ppm was observed during the fourth flight.

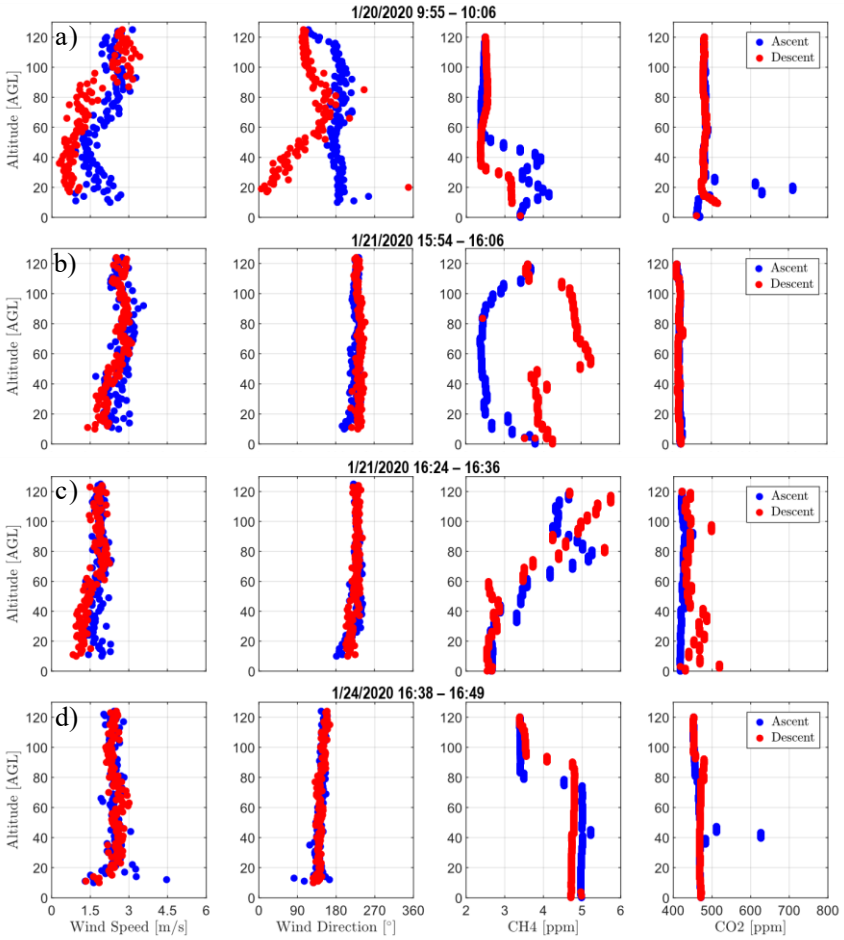

Figure 3-6 The vertical profiles of wind velocity, methane, and carbon dioxide measured using the sUAS-based Aircore system from a) 9:55 to 10:06 PST on January 20th, 2020, b) 15:54 to 16:06 PST on January 21st, 2020, c) 16:24 to 16:36 PST on January 21st, 2020, a, and c) from 16:38 to 16:49 PST on January 24th, 2020.

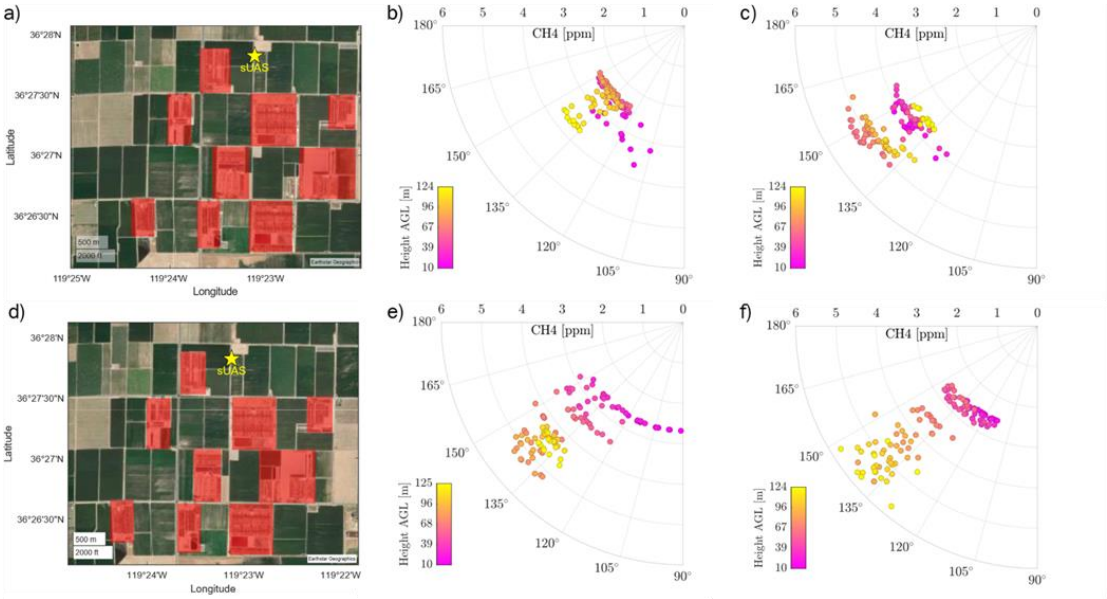

Figure 3-7 A pollution rose analysis showing how the mole fraction of methane changed with respect to wind direction and altitude during the second and third flights performed at the same solation. The a) and d) satellite images show the location where the second and third deployments took place on January 21st, 2020. The b) and c) pollution rose plots show methane enhancement variations with respect to wind direction and height during the second flight. The e) and f) pollution rose plots show methane enhancement variations with respect to wind direction and height.

3.3.2. Validation of Multirotor UAS Wind Velocity Profiles

In Figure 3-8 a, the wind observations collected from the UAS and an 11-m MET tower were found to be in close agreement at the beginning and end of each flight. Differences between the UAS and tower observations were observed only at higher altitudes when the height difference between the UAS and the 11-m MET tower was greatest. The UAS-based Aircore system provided wind speed estimates that were consistent with those near the surface. The wind speed estimates obtained from the UAS-based Aircore system, and the wind power law were observed to display comparable trends in the vicinity of the surface, as shown in Figure 3-8 a. Similarly, the bias was seen to rise as the altitude increased. The discrepancies observed both near the surface and at higher altitudes

emphasize the valuable information that the technology can offer compared to ground-based wind measurements taken from fixed locations.

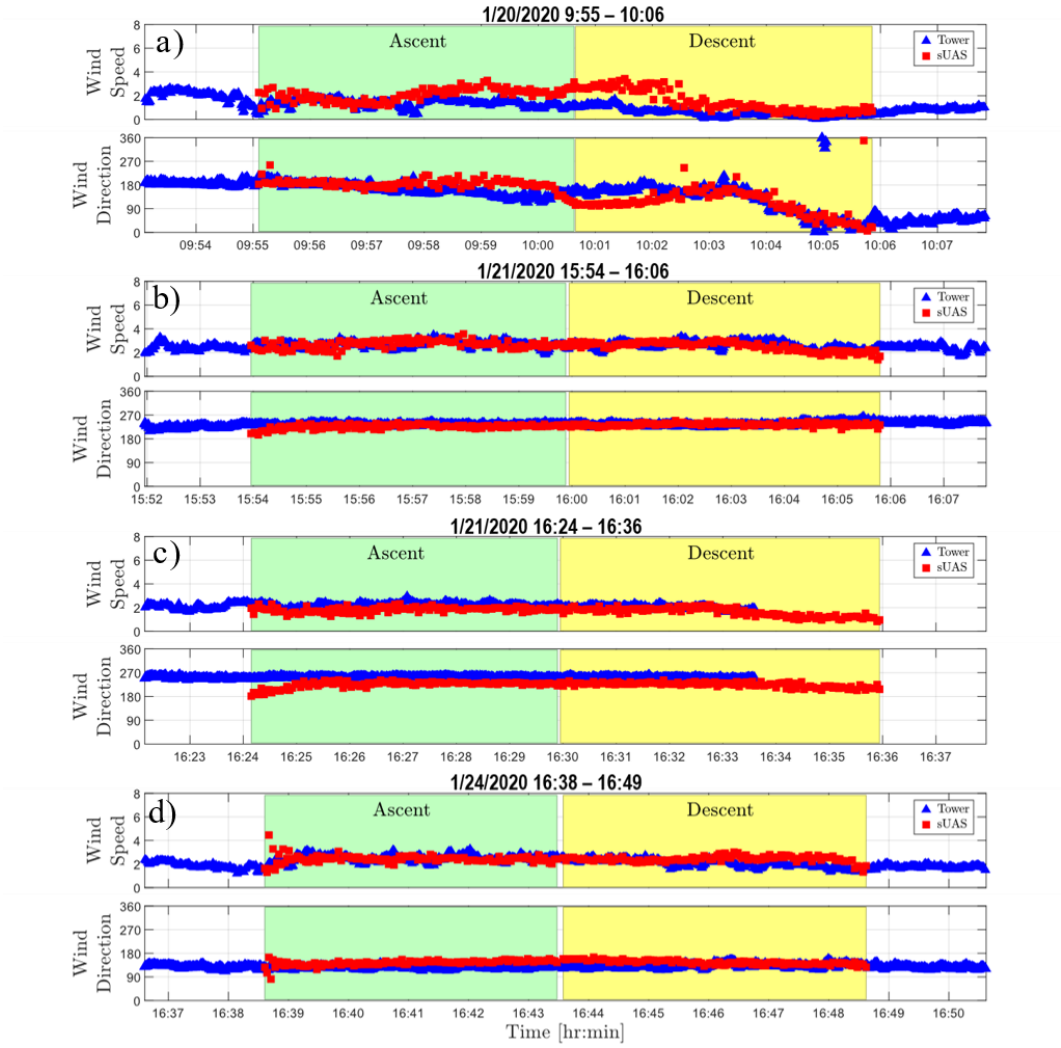

Figure 3-8 The comparison of wind speed observations measured using the UAS-based Aircore sytem and the 11-m MET tower from a) 9:55 to 10:06 PST on January 20th, 2020, b) 15:54 to 16:06 PST on January 21st, 2020, c) 16:24 to 16:36 PST on January 21st, 2020, and c) from 16:38 to 16:49 PST on January 24th, 2020.

3.3.3. Validation of Aircore Profiles

Results from the Aircore calibration experiments show that the Aircore can resolve mole fraction variations of methane occurring over periods of 10 seconds or larger with high accuracy. As shown in Figure 3-9, the peak concentrations between Aircore and CRDS direct measurement corresponding to periods of 5 seconds were found to disagree by a factor greater than 2. The Aircore measurement can resolve the peak concentration more accurately when the signals last for 10 seconds or more. The different performance with signal duration is due to the limitation on CRDS response time and smearing effect in the Aircore. These findings provide useful information on determining Aircore's resolution. With flight speed at 0.3 m/s, the Aircore can reliably measure methane mole fraction variations that are sustained over periods of 10 seconds or larger, which corresponding to the spatial range of 3 m.

Though spatial variation of the concentrations is helpful to describe the distribution of the plume, the smearing effect is not supposed to influence the integration result of the total emission estimated with dispersion model. The integrated areas under the direct CRDS and Aircore measurement are shown in Table 3-3. It is found Aircore measurement has a bias in integration concentration from – 15 % to 20 %. The bias is partially because of the different flow rates between the CRDS and the pump used in the Aircore system and it resulted in different sampled volume with same signal duration. We resampled the Aircore measurement to match the sample number as the direct CRDS measurement.

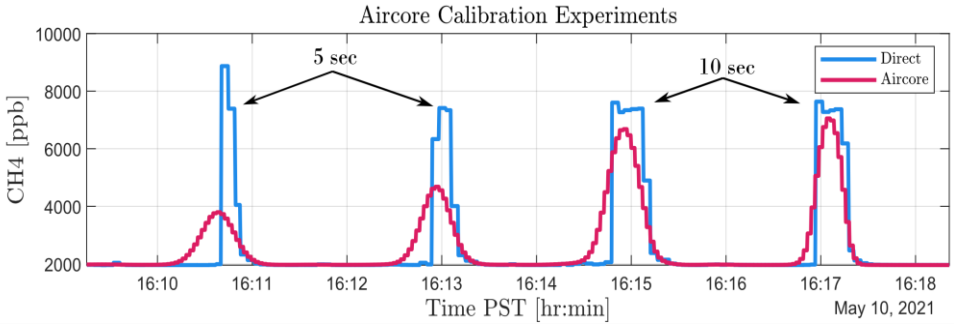

Figure 3-9 A plot showing the comparison of Aircore and CRDS (Direct) measurements of mole fraction spikes produced over time intervals of 5 and 10 seconds.

The mole fractions retrieved from the Aircore and from the ground CRDS during the same time when deployment was ongoing was compared in Figure 3-10. The retrieved mole fraction time series were in the agreement with the ground measurements at the beginning and the end of the deployment. The differences were observed during the flight. The aloft concentration could be higher or lower than the ground concentration. further highlighting the necessities of introducing airborne measure in addition to the ground measurements. Furthermore, during the deployment on January 21st, 2020, between 16:24 and 16:36 PST (Figure 3-10 c), the mole fractions retrieved by the Aircore displayed a similar increase then decrease trend to the ground measurements but provided more detailed information.

Table 3-3 Integrated comparison area under the signals lasting the duration of 5 and 10 seconds.

	5s signals (ppb)	10s signals (ppb)
CRDS (Direct) measurement	1014466	844895
Aircore	810060	979959
Difference percentage	20.1%	-15.7%

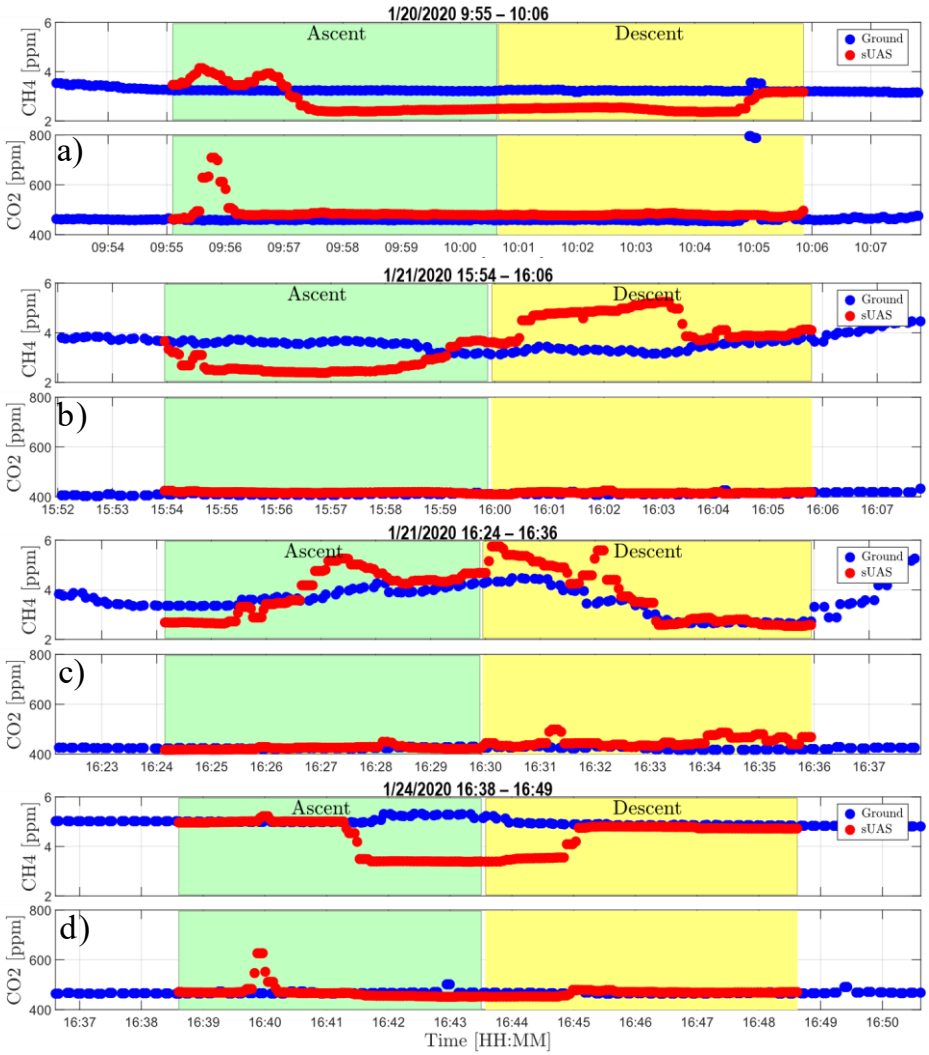

Figure 3-10 The comparison of methane and carbon dioxide observations collected from the UAS-based Aircore system and a ground-based CRDS from a) 9:55 to 10:06 PST on January 20th, 2020, b) 15:54 to 16:06 PST on January 21st, 2020, c) 16:24 to 16:36 PST on January 21st, 2020, and c) from 16:38 to 16:49 PST on January 24th, 2020.

3.3.4. Comparison of Emission Rates Estimated From Different Methods

On January 20th, vertical profiles of wind velocity and methane were utilized in conjunction with dispersion modelling to identify and assess methane emissions from a single dairy farm operation. Figure 3-11 demonstrates how dispersion modelling and

vertical observations of wind velocity and methane can be useful in identifying the areas that have the greatest impact on methane concentrations measured by the UAS-based Aircore system. Moreover, combining dispersion modelling with vertical wind velocity and methane data can aid in quantifying methane emissions, as shown in Table 3-5, where the methane emission estimate was 226 kg per hour. Despite being preliminary, these findings highlight the potential of UAS-based Aircore technology for detecting and quantifying greenhouse gas emissions from dairy farms.

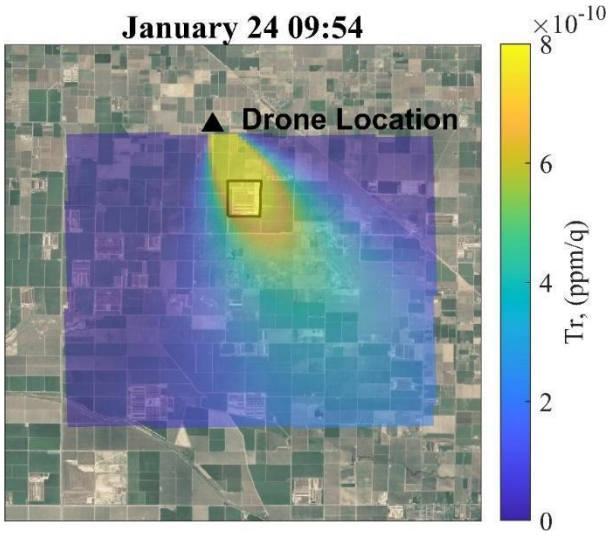

Figure 3-11. Sensitivity map predicted by the dispersion model. The solid triangle shows the place where the drone was flown, and the rectangle area shows the nearest dairy farm we focused on researching. Tr on the color bar is the transport matrix dispersion model estimates, its unit is ppm per unit emission rate.

Table 3-5 Inferred emission rate and 95 % confidence intervals from dispersion model

Time	Emission Rate	95 % Confidence Interval	
		Lower Limit	Upper Limit
01/20/2021 9:54	226.06 kg/hr	180.40 kg/hr	277.28 kg/hr

3.4. Conclusions

Four deployments of the UAS-based Aircore system were successful measuring vertical profiles of wind velocity, methane, and carbon dioxide near dairy farm operations in the San Joaquin Valley. The vertical profiles captured spatiotemporal variations in the mole fraction of methane and carbon dioxide extending up to a height of 120 m during periods of unstable and stable wind conditions.

The UAS-based Aircore system was found to be effective estimating wind speed and wind direction trends in the lower atmosphere. The change in wind direction measurements obtained from UAS-based Aircore system and the 11-m MET tower during flight were consistent. The wind velocity measurements from the UAS-based Aircore system and the 11-m MET tower were consistent at the ground and show discrepancies in the air, suggesting the necessity of introducing the wind estimation during emission quantification.

The UAS-based Aircore system was also found to be reliable profiling methane and carbon dioxide in the lower atmosphere based on laboratory and field experiments. Based on laboratory and field experiments, the UAS-based Aircore system was deemed dependable in profiling methane and carbon dioxide in the lower atmosphere. As with wind estimation, variations were detected in the air, underscoring the significance of understanding the 3-D distribution of the emission plume.

The emission footprint was generated using wind velocity and concentration profiles. The emission rate estimated using dispersion model was about 226.06 kg/hr.

The study highlights the capability of the UAS-based Aircore system to offer wind data and atmospheric compositions in the lower atmosphere, aiding in the identification and detection of potential emission sources, beyond conventional ground measurements. Moreover, the vertical profiles obtained can aid in quantifying emission sources on a facility scale, which can revolutionize the approach to improving bottom-up assessments of emissions.

3.5. References

Aldhafeeri, T., Tran, M. K., Vrolyk, R., Pope, M., & Fowler, M. (2020). A review of methane gas detection sensors: Recent developments and future perspectives. In *Inventions* (Vol. 5, Issue 3, pp. 1–18). MDPI Multidisciplinary Digital Publishing Institute. https://doi.org/10.3390/inventions5030028

Andersen, T., Scheeren, B., Peters, W., & Chen, H. (2018). A UAV-based active AirCore system for measurements of greenhouse gases. *Atmospheric Measurement Techniques*, *11*(5), 2683–2699. https://doi.org/10.5194/amt-11-2683-2018

Brosy, C., Krampf, K., Zeeman, M., Wolf, B., Junkermann, W., Schäfer, K., Emeis, S., & Kunstmann, H. (2017). Simultaneous multicopter-based air sampling and sensing of meteorological variables. *Atmospheric Measurement Techniques*, *10*(8), 2773–2784. https://doi.org/10.5194/amt-10-2773-2017

Demali, G. (n.d.). *Developing a UAS-Deployable Methane Sensor Using Low-Cost Developing a UAS-Deployable Methane Sensor Using Low-Cost Modular Open-Source Components Modular Open-Source Components*. https://ideaexchange.uakron.edu/honors_research_projects

Falabella, A. D., Wallin, D. O., & Lund, J. A. (2018). Application of a customizable sensor platform to detection of atmospheric gases by UAS. *2018 International Conference on Unmanned Aircraft Systems, ICUAS 2018*, 883–890. https://doi.org/10.1109/ICUAS.2018.8453480

Fox, T. A., Barchyn, T. E., Risk, D., Ravikumar, A. P., & Hugenholtz, C. H. (2019). Erratum: A review of close-range and screening technologies for mitigating fugitive methane emissions in upstream oil and gas (Environmental Research Letters (2019) 14 (053002) DOI: 10.1088/1748-9326/ab0cc3). In *Environmental Research Letters* (Vol. 14, Issue 6). Institute of Physics Publishing. https://doi.org/10.1088/1748-9326/ab20f1

Golston, L. M., Tao, L., Brosy, C., Schäfer, K., Wolf, B., McSpiritt, J., Buchholz, B., Caulton, D. R., Pan, D., Zondlo, M. A., Yoel, D., Kunstmann, H., & McGregor, M. (2017). Lightweight mid-infrared methane sensor for unmanned aerial systems. *Applied Physics B: Lasers and Optics*, *123*(6). https://doi.org/10.1007/s00340-017-6735-6

Iwaszenko, S., Kalisz, P., Słota, M., & Rudzki, A. (2021). Detection of natural gas leakages using a laser-based methane sensor and uav. *Remote Sensing*, *13*(3), 1–16. https://doi.org/10.3390/rs13030510

Jha, R. K. (2022). Non-Dispersive Infrared Gas Sensing Technology: A Review. In *IEEE Sensors Journal* (Vol. 22, Issue 1, pp. 6–15). Institute of Electrical and Electronics Engineers Inc. https://doi.org/10.1109/JSEN.2021.3130034

Karion, A., Sweeney, C., Tans, P., & Newberger, T. (2010). AirCore: An innovative atmospheric sampling system. *Journal of Atmospheric and Oceanic Technology*, *27*(11), 1839–1853. https://doi.org/10.1175/2010JTECHA1448.1

McHale, L. E., Hecobian, A., & Yalin, A. P. (2016). Open-path cavity ring-down spectroscopy for trace gas measurements in ambient air. *Optics Express*, *24*(5), 5523. https://doi.org/10.1364/oe.24.005523

Shah, A., Pitt, J. R., Ricketts, H., Brian Leen, J., Williams, P. I., Kabbabe, K., Gallagher, M. W., & Allen, G. (2020). Testing the near-field Gaussian plume inversion flux quantification technique using unmanned aerial vehicle sampling. *Atmospheric Measurement Techniques*, *13*(3), 1467–1484. https://doi.org/10.5194/amt-13-1467-2020

So, S., Park, D. G., Jeong, N., Kim, D., Hwang, J., & Lee, C. (2020). Study on the Simultaneous Measurement of O2 and CO Concentrations in the Exhaust Gas of a Methane/Air Flame Using Tunable Diode Laser Absorption Spectroscopy. *Energy and Fuels*, *34*(3), 3780–3787. https://doi.org/10.1021/acs.energyfuels.9b04357

Wilkinson, J., Bors, C., Burgis, F., Lorke, A., & Bodmer, P. (2018). Measuring CO2 and CH4 with a portable gas analyzer: Closed-loop operation, optimization and assessment. *PLoS ONE*, *13*(4). https://doi.org/10.1371/journal.pone.0193973

4. Small Particle Growth Observations at the U.S. DOE Southern Great Plains Field Site Using Ambient Air Captive Aerosol Chambers

4.1. Introduction

Atmospheric aerosols influence air quality (Viana et al., 2014), human health (Pöschl, 2005), ecosystems (Cirino et al., 2014; Misson et al., 2005), and climate (Jaenicke, 1980; Mcneill, 2017). Aerosols affect climate by absorbing and scattering solar radiation or indirectly influencing cloud properties when they are larger than 50-100 nm to have the potential to act as cloud condensation nuclei (CCN) (Seinfeld and Pandis, 2016). CCN are critical factors in understanding the climate impacts of aerosols.

The concentration and distribution of CCN are significantly influenced by new particle formation (NPF) and growth (Duplissy et al., 2016; Gordon et al., 2017; Kalivitis et al., 2015). The contribution of NPF to the CCN budget depends on particle size, composition, and abundance (Marinescu et al., 2019). Long-term observations and modelling predictions can provide insights into understanding these processes. Particle formation and aging mechanisms are influenced by precursor compounds and ambient conditions, including solar intensity, temperature, and relative humidity (Kerminen, 2018). Conventional approaches for studying the growth of small particles typically focus on one or a few precursor gases or rely on observations of the dynamics of ambient particle populations. Significant variations in NPF frequency exist between different locations. For instance, the NPF event frequency is reported as high as 86% in South Africa

(Hirsikko et al., 2012) , while no NPF events were observed during a three-month study in the Amazonian Forest (Wimmer et al., 2017).

Interpreting and comparing aerosol observations quantitatively is challenging since the measurements are affected by both gas and particle phase chemistry, as well as the variability in the origin and history of local and transported aerosols at a given time. Considering the growth rate is usually estimated only when NPF exists, during which limited data is available with more specific atmospheric conditions for homogeneous or heterogeneous nucleation (Kulmala et al., 2014). The heterogeneity of particle formation and growth also necessitates long-term continuous measurements that encompass a wide range of conditions.

While traditional environmental chambers provide detailed information on the species and processes involved in secondary aerosol formation and growth, they are often restricted to narrow ranges of simulated conditions and do not capture the complexity and variability of the ambient atmosphere. To address this, the Captive Aerosol Growth and Evolution (CAGE) chamber system has been developed, which is portable and designed for field use (Sirmollo et al., 2020). The system mirrors outdoor conditions including air composition and solar intensity. The system includes two identical chambers, one serving as a baseline or reference, and the other as a perturbation chamber to assess the sensitivity of particle growth to different conditions.

In this study, the results from the first deployment of the CAGE chambers at the DOE Atmospheric Radiation Measurement (ARM) Program's Southern Great Plains (SGP) site

in the late summer and fall of 2021 were analyzed. We quantified the time dependence of the growth rate throughout the study and studied the sensitivity of particle growth to the injected seed particle composition, liquid water content and precursor gas additions such as α-pinene and SO_2.

4.2. Methods

4.2.1. CAGE Chambers

Figure 4-1 illustrates a schematic of the two CAGE chambers used in the study. Detailed information about the chambers' characteristics and features has been previously reported (Sirmollo et al., 2020). Each chamber has a 2 m^3 cylindrical reactor made of UV-transmitting PFA film, with a gas-permeable 0.005 mm expanded polytetrafluoroethylene (ePTFE; Phillips Scientific) center channel.

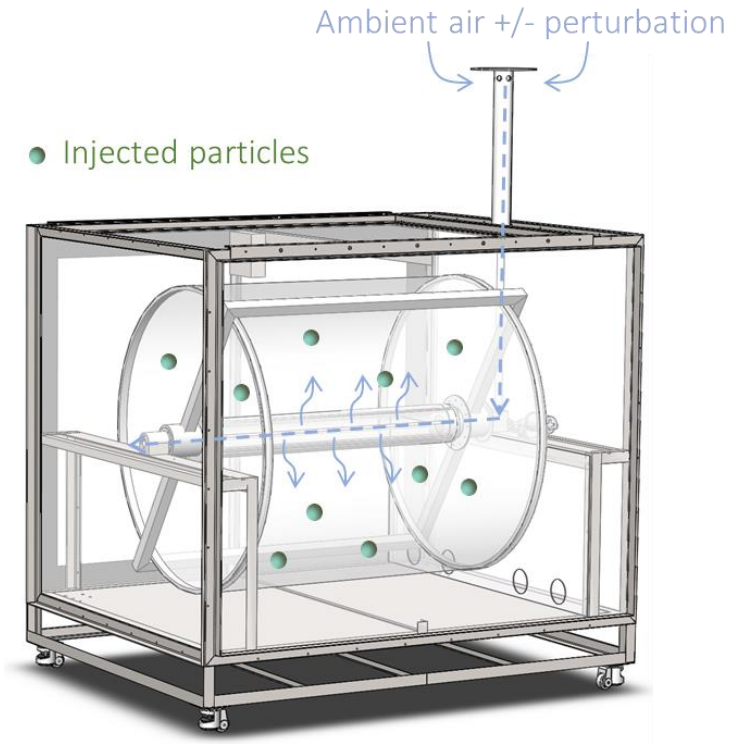

Figure 4-1 Sketch of a CAGE chamber showing the path of ambient air that is pulled in through an inlet, filtered, and then flows through the center of the ePTFE membrane-wrapped center channel.

The CAGE chambers are designed to draw ambient air through an inlet with PTFE particle filter on the top of the chamber, which then through the gas-permeable ePTFE membrane and around the chamber before being exhausted through a port connected to a blower below the chamber. This process enables efficient gas exchange and allows the chamber to maintain gas composition and concentrations close to ambient levels. The reactor is maintained at a positive pressure differential of around 1 mbar relative to the surroundings to prevent deformation and minimize contamination.

The size selected particles are injected to the chamber using the injection system that will be introduced in the next section. The injected particles are exposed to the ambient air

pulled through the ePTFE membrane and its growth is tracked by the sample system that will also be covered in the next section. To prevent losses of large particles due to gravitational settling and small particles due to convective eddies, the chambers are rotated at approximately 3 revolution per minute (rpm) using an AC motor and a pair of sprockets.

The enclosure is coated with fluoroethylene vinyl ether (FEVE) and is enclosed by S-UVT acrylic panels that transmit UV and visible light. While some solar radiation is lost through the acrylic and PFA, a PTFE gasket sheet on the enclosure floor reflects UV light to partially compensate for this loss. To characterize the relationship between the spectral actinic flux in the chambers and the ambient environment, the cosine-weighted solar spectral intensity was measured outside and at a point between the bottom of the chamber and the reflective PTFE gasket (Figure 4-2).

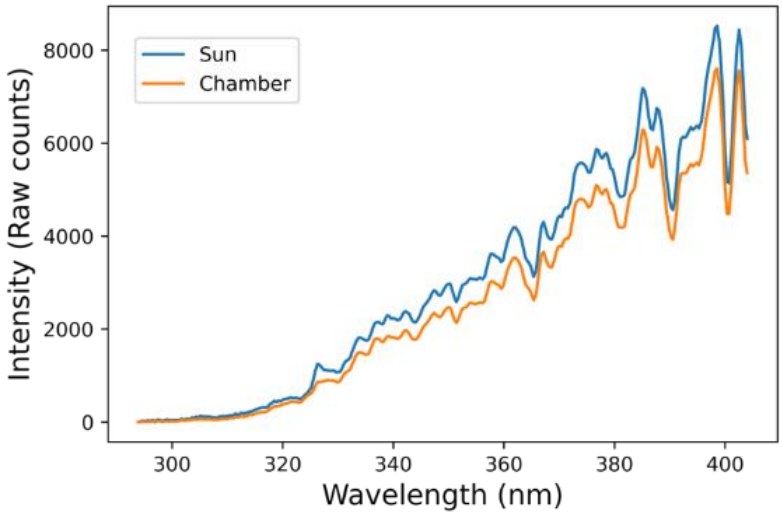

Figure 4-2 Comparison of spectral intensity measured just below one of the chambers and just outside of the chamber enclosure on a sunny day.

Trace gas concentrations in the chamber can be explained by treating the volume as a continuous stirred-tank reactor (CSTR). The resulting rate of change of the concentration of any of the trace gases can then be expressed as

$$\frac{dC_{ch}}{dt} = P - L + \frac{Q_{ex}}{V_{ch}} C_{amb} - \frac{Q_{ex}}{V_{ch}} C_{ch} \qquad (4\text{-}4)$$

Where C_{ch} is the concentration in the chamber, C_{amb} is the ambient concentration, V_{ch} is the volume of the chamber ($\approx$ 2000 L), P and L are the per unit volume rates of chemical production and loss in the chamber, respectively, and Q_{ex} is the effective exchange "flow rate" across the ePTFE membrane. The Q_{ex} cannot be measured directly and is instead estimated using Eq. (4-4) and time series of SO_2 concentration measured in the chamber. The Q_{ex} was estimated to be at about 24 L min^{-1} and $Vch/Q_{ex} = 85$ min residence time in the chamber.

4 thermistors placed at various locations inside and outside each chamber monitor the temperature. Measured temperature was sent to the control system to adjust the AC system's compressor's speed accordingly. The temperature inside the two chambers is regulated using a Micro Air Conditioner DV3220E-AC to mimic ambient conditions. The average temperature inside the chamber was maintained within 5 °C of the outside temperature.

4.2.2. Measurement Site

From August 9th to November 20th 2021, the campaign was carried out at the Southern Great Plains (SGP) site of the DOE Atmospheric Radiation Measurement (ARM) Program, situated in Oklahoma, US (Figure 4-3). The site, located southeast of Lamont, Oklahoma, is near cattle pasture and wheat fields and can be pinpointed at coordinates (36.607322, -97.487643).

Figure 4-3 (a): Satellite images of the Southern Great Plains (SGP) site relative to Oklahoma and Kansas. (b): The location of SGP at which the field study was conducted. Map data © 2022 Google. (c): the clearing in which the chambers and instrument trailers were.

4.2.3. Instrumentation

The configuration for the dual-chamber experimental system is shown in Figure 4-4. The CAGE chambers were deployed outside the Aerosol Observing System (AOS) trailer and the sampling, aerosol generation, and trace gas perturbation equipment were located inside (Figure 4-3 c.). The particle injection and sampling lines were connected using 316 stainless steel tubes with 0.95 cm outer diameter of about 5 m long. The gas injection and sampling lines were constructed using Teflon tubes with also 0.95 cm outer diameter of about the same length as particle sample and injection lines.

A monodisperse seed particle was produced by atomizing ammonium sulfate solution using a TSI 3076 atomizer, drying it using a silica gel diffusion dryer, and separating a narrow size range at approximately 0.07 μm with a differential mobility analyzer (DMA). The particle mode was repeatedly injected into the chambers as soon as the previous one became difficult to track.

A scanning mobility particle sizer (SMPS) was utilized to determine the size distribution in the two chambers approximately four times per hour. The system was configured to measure between the two chambers and the ambient air in one sequence. The sample aerosol was dried and neutralized with a Nafion tube bundle (Perma Pure Inc., USA) and a soft x-ray neutralizer L12535 (Hamamatsu, Japan). The sample then entered SMPS equipped with a TSI 3762 condensation particle counter (CPC) and a high flow DMA to quantify the particle size distribution in the range from 0.013 to 0.40 μm.

During the field experiments, one of the chambers was designated as the control, with only dried ammonium sulfate seed particles injected and ventilated solely with ambient air. Perturbation in particle composition was realized by atomizing potassium sulfate solution. The gas phase perturbation was mixed with ambient air controlled by a mass flow controller.

To aid in understanding the growth events, observations from pre-existing ARM measurements were utilized. Ozone (O_3) was measured using Thermo Fisher Scientific 49C Ozone Analyzer. Sulfur dioxide (SO_2) was measured using a Model 43i trace level-enhanced pulsed fluorescence SO_2 analyzer (Thermo Scientific, USA). The meteorological information including surface wind speed, wind direction, air temperature, and relative humidity was retrieved from the data archive from ARM Surface Meteorology Systems (MET). Non-refractory submicron particulate matter including organic aerosol (OA), sulfate, nitrate, ammonium, and chloride was measured with Aerosol Chemical Speciation Monitor (ACSM).

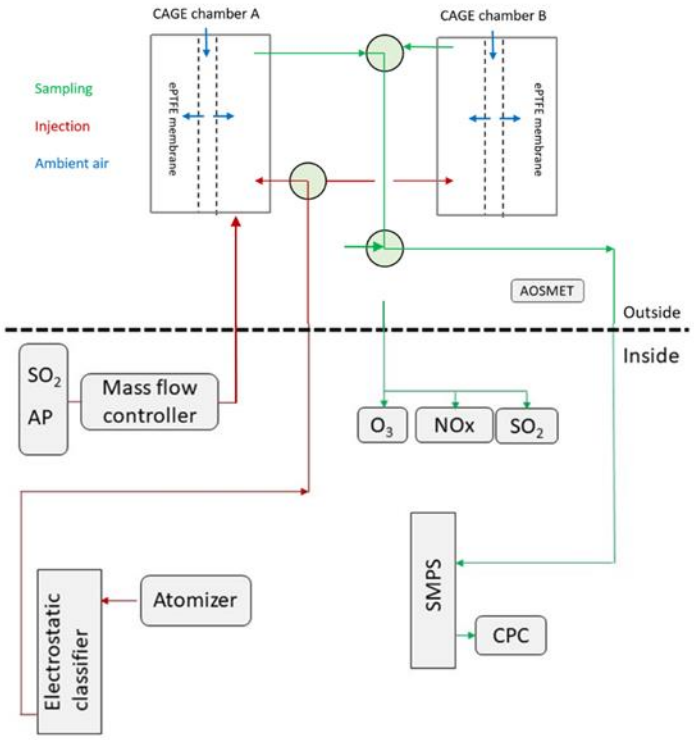

Figure 4-4 Schematic of the dual-chamber experimental system.

4.3. Results

4.3.1. Hourly Variations of Particle Growth Rate

Throughout the experiments, the particle size distribution outside and inside both chambers were measured continuously. A lognormal function was used to fit the tracked mode and decide the dry particle diameter D_p and number concentration N. The time series shows an example of the ambient and chamber measurements (Figure 4-5). During the 2.5 days period, both chambers were filled with only ambient air. The particle growths reflected the ambient aerosol growth. The x-y representation to the left shows the same injection mode at the time indicated by the black box. The multiple peaks in the x-y

plot were a result of multiple charging. In this case, particles with higher-order charges and the same apparent mobility or mass-to-charge ratio could be chosen simultaneously using a DMA (Bau et al., 2014). We kept tracking the mode with the highest concentration when injected. The average particle lifetime inside the chambers was about 6 hours.

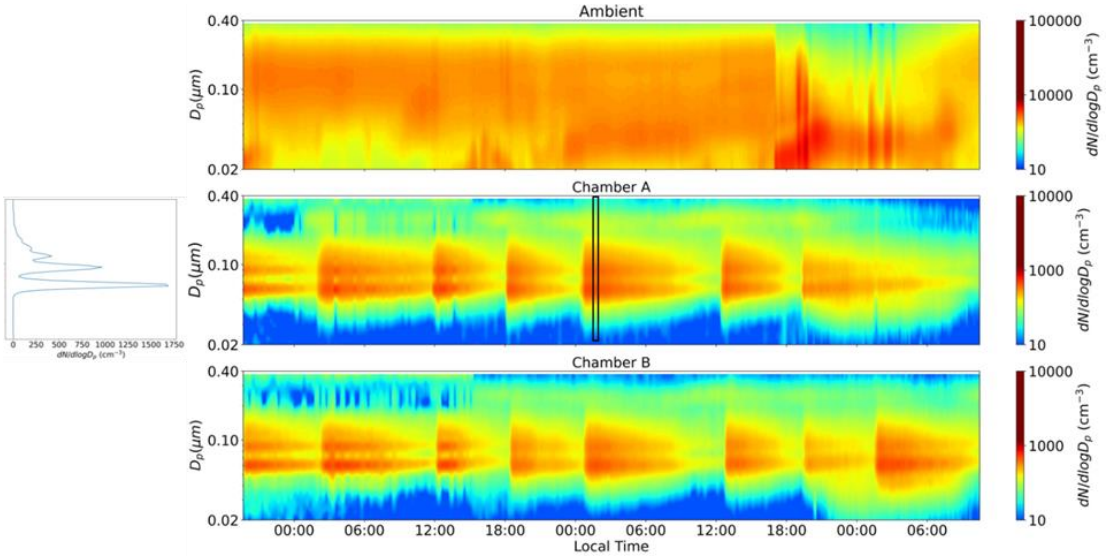

Figure 4-5 Top: Ambient aerosol size distribution time series from October 8th to 11th during the 2021 study. Middle and bottom: size distribution time series over the same period in chamber A and B with ambient air flushed. Left: x-y presentation of the size distribution measured at the time indicated by the rectangle in the time series.

The corresponding track mode is shown in Figure 4-6 with shaded bands indicating nighttime. The time-dependent growth rate for each tracked mode is calculated as the change in lognormal fit D_p between two successive measurements divided by the time difference, $\mathrm{GR} = \Delta D_p/\Delta t$. Growth in both chambers is in agreement when conditions were similar.

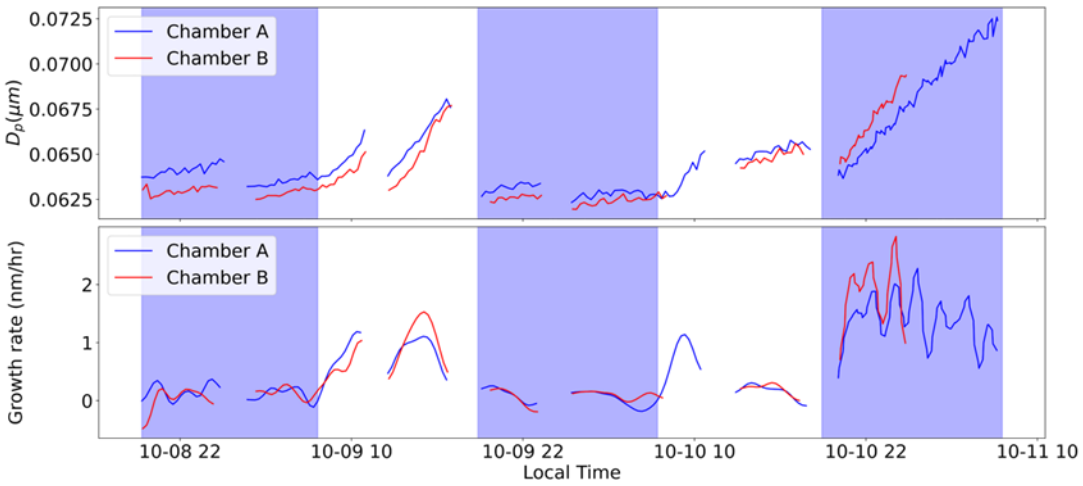

Figure 4-6 Top: Time series of the lognormal fit diameters of injected modes in Figure 4-5. Lower: Calculated growth rates for the same period at the top.

Using the continuous measurements in the reference chamber, the time-of-day-dependent growth rate is shown in Figure 4-7. GR keeps positive throughout the day, showing the lowest value in the late afternoon before sunset and the highest in the morning after sunrise. This agrees with the average growth rate calculated from the previous deployment of the second generation of CAGE chambers in Houston in 2016 (Sirmollo et al., 2020).

We observed active nighttime growth during the study. Though regional NPF typically happens in the daytime when photochemistry activity is strong, several studies have reported various pathways contributing to nighttime particle growth, including the formation of highly functionalized organonitrates (ON) by volatile organic compounds (VOC) with NO_x (W. Huang et al., 2019), and increase in semi-volatile oxygenated organic aerosol (SV-OOA) and condensed highly oxygenated organic molecules (HOMs)

(Hao et al., 2018). It is found nighttime production of HNO_3 dominates at SGP (Parworth et al., 2015). A significant HOM fraction was reported to be contained in bulk submicron OA measured at SGP (Liu et al., 2021).

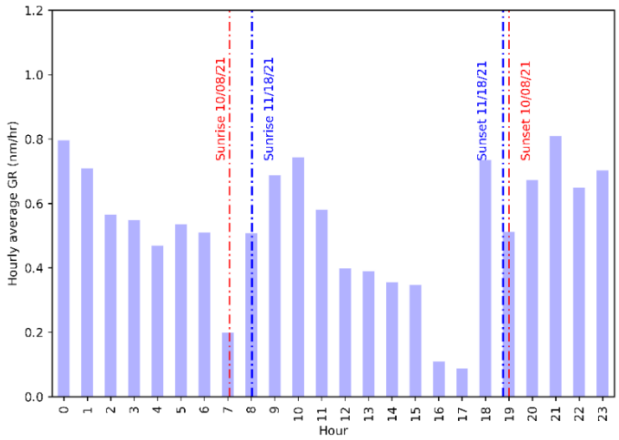

Figure 4-7 Hourly average particle growth rate histogram. A total of 1212 values were used to construct the histogram. The time of sunrise and sunset for the first (October 8) and last (November 18) day of measurements are also indicated.

4.3.2. Case Study: 10 October, Growth With Air Mass Change

On 10 October 2021, an ambient aerosol growth was recorded by the SMPS beginning around 17:00 central daylight time (CDT) (Fig. 4-8a). The time series for the lognormal fit diameters of injected modes in the two chambers and corresponding calculated growth rates are presented in Figure 4-8b-c. Both chambers showed similar rapid growth, with an average growth rate increasing from 0.3 nm $hour^{-1}$ to 1.3 nm $hour^{-1}$. At the same time, there was a change in wind direction from southwest to north as well as a decrease in temperature and an increase in relative humidity (Fig. 4-8e). Ozone concentration also showed a sudden change at 17:00. Additionally, the organic mass fraction measured by ACSM increased around the same time, as shown in Figure 4-8g, which is consistent with

the other observations. The sudden changes observed in various features of the ambient air indicate a possible shift in air mass with the change in wind direction. The growth observed in the chambers is in agreement with the ambient aerosol growth, providing a simpler way to quantify particle growth in the absence of new particle formation.

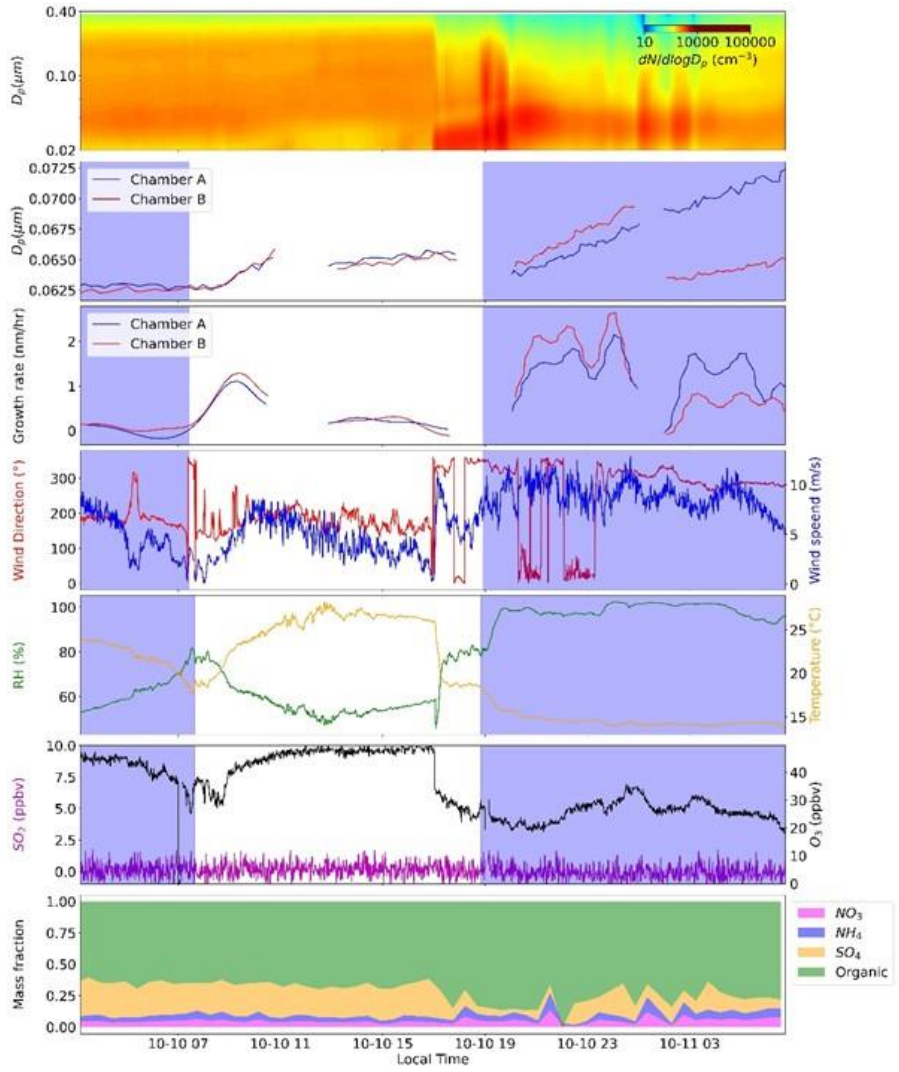

Figure 4-8 (a): Ambient aerosol size distribution time series. (b): time series of the lognormal fit diameters of injected modes in the two chambers. (c): calculated growth rates for the same period in (b). (d): wind direction and wind speed. (e): ambient relative humidity and temperature. (f) ambient SO_2 and O_3 concentration. (f): non-refractory submicron aerosol species measured with the ACSM.

4.3.3. Effect of Gas Addition of Precursor Gases on Particle Growth Rate

4.3.3.1. Effect of α-Pinene on Particle Growth Rate

The oxidation of α-pinene can result in the formation of secondary organic aerosols through acid-base reactions or equilibrium partitioning (Tröstl et al., 2016). In order to evaluate the sensitivity of particle growth to α-pinene, we injected α-pinene continuously from a compressed gas cylinder with a mass flow controller (Figure 4-9). The flow rate was set based on the estimated gas exchange flow rate of 24 L min^{-1} to keep the α-pinene concentration at about 5 ppb at equilibrium. The background chamber was operated with ambient air and no perturbation added.

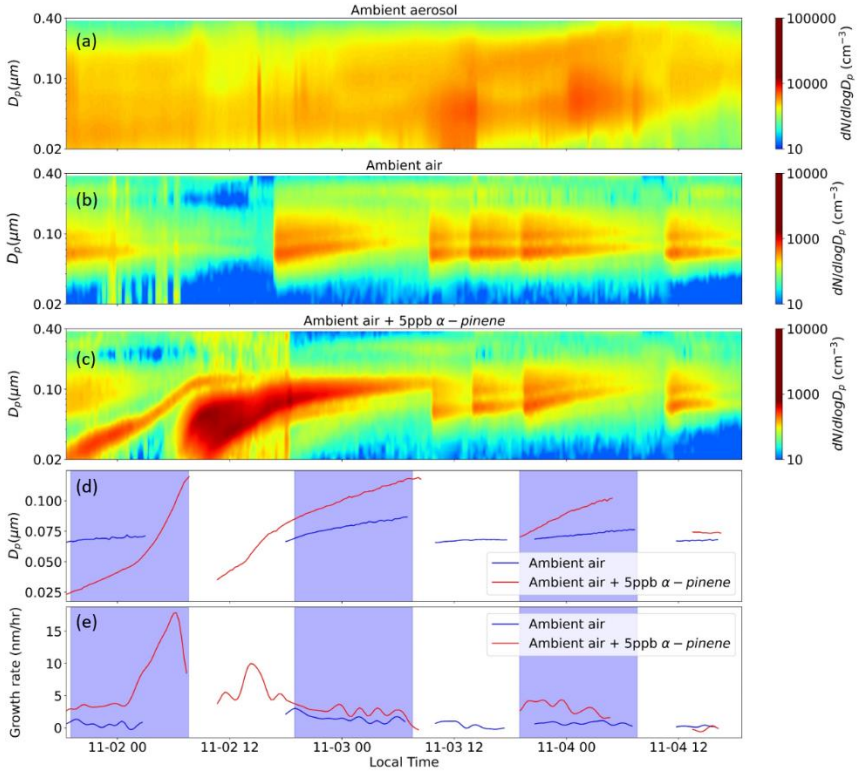

Figure 4-9 (a): Ambient aerosol size distribution time series over 2.5 days during the α-pinene injection. (b): Size distribution time series over the same period in the reference chamber with ambient air flushed. (c): Size distribution time series over the same period in the perturbed chamber with ambient air and 5 ppb α-pinene flushed. (d): Time series of the lognormal fit diameters of injected modes in the two chambers. (e): Particle growth rates calculated from the time series of lognormal fit diameters.

4.3.3.2. Effect of SO_2 on Particle Growth Rate

The previous study (Hodshire et al., 2016) found growth due to H_2SO_4 was significant at SGP. To investigate the sensitivity of particle growth to SO_2, we flushed ambient air spiked with 5 ppb SO_2 for the perturbed chamber. Figure 4-10 shows the size distribution series through this experiment.

In the chamber where SO_2 was added, two nucleation modes were detected starting in the morning at approximately 8:00 CDT on November 5 and 6. Unlike the addition of α-pinene, which is highly reactive with both O_3 and OH, the introduction of SO_2 led to

increased growth mainly during the daytime due to the strong dependence of OH on sunlight, when it also triggered NPF events. The growth rate in the reference chamber remained constant at approximately 0.5 nm hour^{-1}. In contrast, the chamber with SO_2 injection had a significantly higher growth rate of approximately 2.5 nm hour^{-1}.

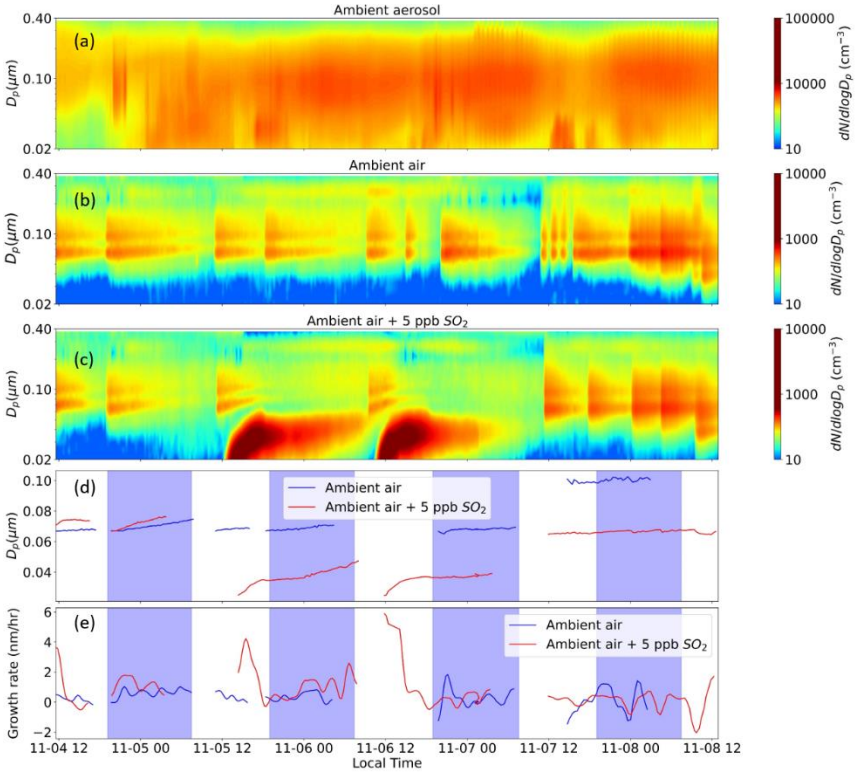

Figure 4-10 (a): Ambient aerosol size distribution time series 4 days during the SO_2 injection. (b): Size distribution time series over the same period in the reference chamber with ambient air flushed. (c): Size distribution time series over the same period in the perturbed chamber with ambient air and 5 ppb SO_2 flushed. (d): Time series of the lognormal fit diameters of injected modes in the two chambers. (e): Particle growth rates calculated from the time series of lognormal fit diameters.

4.3.4. Effect of Particle Compositions on Particle Growth Rate

To examine the impact of particle compositions, we introduced dry ammonium sulfate (AS) and dry potassium sulfate (KS) particles into the two chambers. The deliquescence

relative humidity (DRH) of AS is 75%, whereas KS has a much higher DRH at 96% (Seinfeld and Pandis, 2016). This property enables KS particles to remain crystalline while AS particles become aqueous when the ambient relative humidity (RH) reaches 80% but remains below 96%. The markers on the growth rate curves (Fig 4-11. c) identify those times when the seed particles were believed to be in aqueous phase based on the RH history and efflorescence and deliquescence RH of the two types. (Fig 4-11. e). The particles were assumed to remain solid until the RH reaches DRH, at which particles spontaneously absorb water and become aqueous phase. With RH decreasing, particles remain supersaturated until efflorescence relative humidity (ERH) occurs. AS has ERH at 35% and KS's ERH is 60%.

During the first injection mode in the afternoon of October 25, the ambient RH was above 80%, causing the AS particles to become aqueous once injected. The KS particles, on the other hand, were initially crystalline but became aqueous that night as the ambient RH increased beyond 96%. A higher growth rate was observed for aqueous-phase AS particles compared to crystalline KS particles, as well as for aqueous-phase KS particles compared to crystalline KS particles earlier. In the second injection, aqueous-phase AS particles also exhibited a higher growth rate than crystalline KS particles. In the subsequent third and fourth injections, the two types of particles showed consistent growth rates when in both crystalline and aqueous phases.

On the night of October 27, the RH increased to nearly 100% with precipitation, a wind shift and a temperature decrease. The organic fraction in the ambient aerosols decreased

relative to the inorganic fraction (Fig 4-11. g), which could be a result of enhancement in aerosol hygroscopic growth in the ambient air (Bougiatioti et al., 2016). The faster growth observed when both types of particles were in the aqueous phase suggests that water uptake had a positive impact on particle growth.

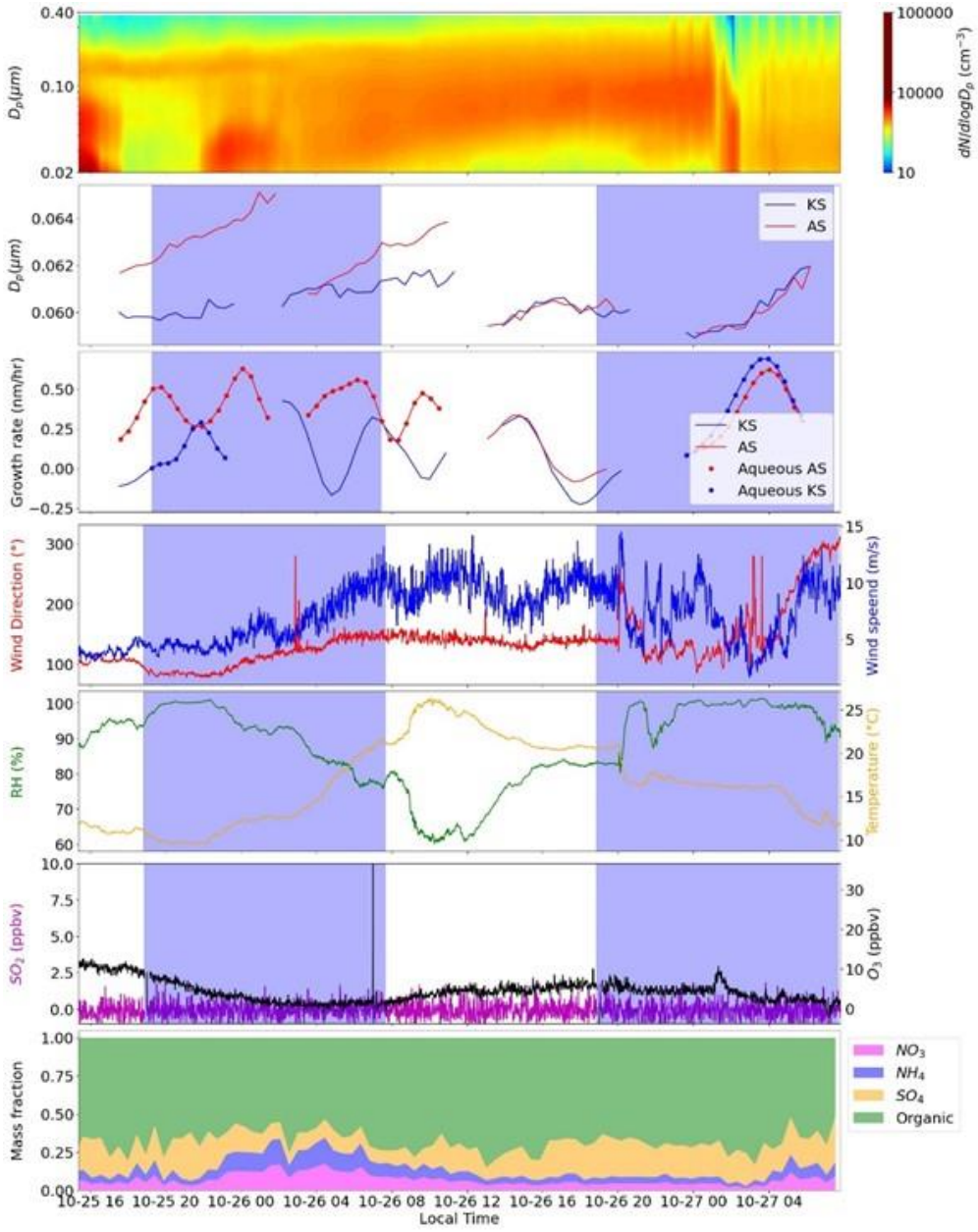

Figure 4-11 (a): Ambient aerosol size distribution time series 2 days during the particle compositions sensitivity experiment. (b): Time series of the lognormal fit diameters of injected modes in the two chambers. (c): Particle growth rates calculated from the time series of lognormal fit diameters with markers for modes in aqueous phase based on the RH history and efflorescence and deliquescence RH of the two types. (d): Wind direction and wind speed. (e): Ambient relative humidity and temperature. (f) Ambient SO_2 and O_3 concentration. (g): Mass fractions.

4.4. Summary

During the late summer and fall of 2021, we conducted a two-month operation of the CAGE chamber system at the DOE Southern Great Plains (SGP) site. Both chambers were continuously operated, with monodisperse seed particles injected every few hours and intermittently measured by a SMPS. To investigate the sensitivity of particle growth to the composition of the injected seed particles and liquid water content, as well as the addition of precursor gases, we utilized one chamber as a reference and the other as a perturbation chamber.

The preliminary experiments demonstrated consistent growth in both chambers under similar conditions. The occurrence of new particle formation and growth on October 10th serves as an example of how the CAGE chambers can mirror changes in ambient conditions when there are alterations in the air mass and meteorological conditions. During the study, size-resolved ammonium sulfate particles were injected into the reference chamber while the other chamber was injected with only filtered ambient air. The time dependent growth rate of the particles in the reference chamber was quantified and the average growth rate was found to be highest in the morning after sunrise and lowest in the afternoon before sunset.

To study the impact of precursor gases, we introduced 5 ppb α-pinene or 5 ppb SO_2 into the ambient air while keeping the reference chamber flushed with ambient air. The particle growth rate in the perturbed chamber with 5 ppb α-pinene was 5 times higher than that in the reference chamber, both during the day and night. On the other hand, the

addition of SO_2 led to increased growth only during the daytime and triggered NPF events.

The impact of different seed particle types and corresponding influence from their water contents was investigated by injecting dry ammonium sulfate particles into the reference chamber and dry potassium sulfate particles into the perturbed chamber. We observed that both compositions had about 4 times higher growth rates when in the aqueous phase compared to when in the crystalline phase.

4.5. References

Bau, S., Bémer, D., Grippari, F., Appert-Collin, J. C., & Thomas, D. (2014). Determining the effective density of airborne nanoparticles using multiple charging correction in a tandem DMA/ELPI setup. *Journal of Nanoparticle Research*, *16*(10), 1–13. https://doi.org/10.1007/s11051-014-2629-2

Bougiatioti, A., Bezantakos, S., Stavroulas, I., Kalivitis, N., Kokkalis, P., Biskos, G., Mihalopoulos, N., Papayannis, A., & Nenes, A. (2016). Biomass-burning impact on CCN number, hygroscopicity and cloud formation during summertime in the eastern Mediterranean. *Atmospheric Chemistry and Physics*, *16*(11), 7389–7409. https://doi.org/10.5194/acp-16-7389-2016

Boy, M., Mogensen, D., Smolander, S., Zhou, L., Nieminen, T., Paasonen, P., Plass-Dülmer, C., Sipilä, M., Petäjä, T., Mauldin, L., Berresheim, H., & Kulmala, M. (2013). Oxidation of SO_2 by stabilized Criegee intermediate (sCI) radicals as a crucial source for atmospheric sulfuric acid concentrations. *Atmospheric Chemistry and Physics*, *13*(7), 3865–3879. https://doi.org/10.5194/acp-13-3865-2013

Cirino, G. G., Souza, R. A. F., Adams, D. K., & Artaxo, P. (2014). The effect of atmospheric aerosol particles and clouds on net ecosystem exchange in the Amazon. *Atmospheric Chemistry and Physics*, *14*(13), 6523–6543. https://doi.org/10.5194/acp-14-6523-2014

Goldberg, L. J. (1971). Environment, Aerosol Facility67rai7) (A /AH) =-mgdt/6iraqH (1) where H = height of chamber, a = radius of particle, A = cross sectional area of chamber, C = aerosol particulate concentration, v = Stokes velocity, m = mass of particle (4/3ira3d), d = density of particle, g = gravitational con-stant, Xj = viscosity of air, and where the term “mg/6ira-q” defines the Stokes velocity of free fall. In *APPLIED MICROBIOLOGY* (Vol. 21, Issue 2). https://journals.asm.org/journal/am

Hao, L., Garmash, O., Ehn, M., Miettinen, P., Massoli, P., Mikkonen, S., Jokinen, T., Roldin, P., Aalto, P., Yli-Juuti, T., Joutsensaari, J., Petäjä, T., Kulmala, M., Lehtinen, K. E. J., Worsnop, D. R., & Virtanen, A. (2018). Combined effects of boundary layer dynamics and atmospheric chemistry on aerosol composition during new particle formation periods. *Atmospheric Chemistry and Physics*, *18*(23), 17705–17716. https://doi.org/10.5194/acp-18-17705-2018

Hirsikko, A., Vakkari, V., Tiitta, P., Manninen, H. E., Gagné, S., Gagné, S., Laakso, H., Kulmala, M., Mirme, A., Mirme, S., Mabaso, D., Beukes, J. P., & Laakso, L. (2012). Characterisation of sub-micron particle number concentrations and formation events

in the western Bushveld Igneous Complex, South Africa. *Atmospheric Chemistry and Physics*, *12*(9), 3951–3967. https://doi.org/10.5194/acp-12-3951-2012

Hodshire, A. L., Lawler, M. J., Zhao, J., Ortega, J., Jen, C., Yli-juuti, T., Brewer, J. F., Kodros, J. K., Barsanti, K. C., Hanson, D. R., Mcmurry, P. H., Smith, J. N., & Pierce, J. R. (2016). *Multiple new-particle growth pathways observed at the US DOE Southern Great Plains field site*. 9321–9348. https://doi.org/10.5194/acp-16-9321-2016

Huang, W., Saathoff, H., Shen, X., Ramisetty, R., Leisner, T., & Mohr, C. (2019). Chemical Characterization of Highly Functionalized Organonitrates Contributing to Night-Time Organic Aerosol Mass Loadings and Particle Growth. *Environmental Science and Technology*, *53*(3), 1165–1174. https://doi.org/10.1021/acs.est.8b05826

Jaenicke, R. (1980). ATMOSPHERIC AEROSOLS AND GLOBAL CLIMATE. In *J Aerosol Sci* (Vol. 11). Pergamon Press Ltd.

Kerminen, V. (2018). *Atmospheric new particle formation and growth: review of field observations Atmospheric new particle formation and growth : review of fi eld observations*.

Kulmala, M., Petäjä, T., Ehn, M., Thornton, J., Sipilä, M., Worsnop, D. R., & Kerminen, V. M. (2014). Chemistry of atmospheric nucleation: On the recent advances on precursor characterization and atmospheric cluster composition in connection with atmospheric new particle formation. *Annual Review of Physical Chemistry*, *65*, 21–37. https://doi.org/10.1146/annurev-physchem-040412-110014

Liu, J., Alexander, L., Fast, J. D., Lindenmaier, R., & Shilling, J. E. (2021). *Aerosol characteristics at the Southern Great Plains site during the HI-SCALE campaign*. 5101–5116.

Mcneill, V. F. (2017). *Atmospheric Aerosols: Clouds, Chemistry, and Climate*. https://doi.org/10.1146/annurev-chembioeng

Misson, L., Lunden, M., McKay, M., & Goldstein, A. H. (2005). Atmospheric aerosol light scattering and surface wetness influence the diurnal pattern of net ecosystem exchange in a semi-arid ponderosa pine plantation. *Agricultural and Forest Meteorology*, *129*(1–2), 69–83. https://doi.org/10.1016/j.agrformet.2004.11.008

Parworth, C., Fast, J., Mei, F., Shippert, T., Sivaraman, C., Tilp, A., Watson, T., & Zhang, Q. (2015). Long-term measurements of submicrometer aerosol chemistry at the Southern Great Plains (SGP) using an Aerosol Chemical Speciation Monitor (ACSM).

Atmospheric Environment, *106*, 43–55. https://doi.org/10.1016/j.atmosenv.2015.01.060

Pöschl, U. (2005). Atmospheric aerosols: Composition, transformation, climate and health effects. In *Angewandte Chemie - International Edition* (Vol. 44, Issue 46, pp. 7520–7540). https://doi.org/10.1002/anie.200501122

Sirmollo, C., Collins, D., McCormick, J., Milan, C., Erickson, M., Flynn, J., Sheesley, R., Usenko, S., Wallace, H., Bui, A., Griffin, R., Tezak, M., Kinahan, S., & Santarpia, J. (2020). Captive Aerosol Growth and Evolution (CAGE) chamber system to investigate particle growth due to secondary aerosol formation. *Atmospheric Measurement Techniques Discussions*, *December*, 1–28. https://doi.org/10.5194/amt-2020-443

Tröstl, J., Chuang, W. K., Gordon, H., Heinritzi, M., Yan, C., Molteni, U., Ahlm, L., Frege, C., Bianchi, F., Wagner, R., Simon, M., Lehtipalo, K., Williamson, C., Craven, J. S., Duplissy, J., Adamov, A., Almeida, J., Bernhammer, A. K., Breitenlechner, M., … Baltensperger, U. (2016). The role of low-volatility organic compounds in initial particle growth in the atmosphere. *Nature*, *533*(7604), 527–531. https://doi.org/10.1038/nature18271

Viana, M., Pey, J., Querol, X., Alastuey, A., de Leeuw, F., & Lükewille, A. (2014). Natural sources of atmospheric aerosols influencing air quality across Europe. *Science of the Total Environment*, *472*, 825–833. https://doi.org/10.1016/j.scitotenv.2013.11.140

Wimmer, D., Buenrostro Mazon, S., Manninen, H. E., Kangasluoma, J., Franchin, A., Nieminen, T., Backmann, J., Wang, J., Kuang, C., Krejci, R., Brito, J., Goncalves Morais, F., Martin, S. T., Artaxo, P., Kulmala, M., Kerminen, V.-M., & Petäjä, T. (2017). Direct observation of molecular clusters and nucleation mode particles in the Amazon. *Atmospheric Chemistry and Physics Discussions*, *August*, 1–37.

5. Mapping the Aerosol Properties at Houston During the TRACER-MAP Campaign

5.1. Introduction

Atmospheric particles can have negative effects on air quality (Viana et al., 2014), visibility (Manisalidis et al., 2020), and human health (Pöschl, 2005), as well as influence climate through direct and indirect forcing (Jaenicke, 1980; Mcneill, 2017). Sources of aerosol particles can be direct emissions or via secondary reactions. The growth, aging, and cloud condensation nuclei (CCN) activity of the aerosols differs with various sources and environmental conditions (Prisle et al., 2010; Seinfeld & Pandis, 2006; Pöschl, 2002). Previous studies have explored the characterization of aerosols in both rural and urban environments in terms of their emissions, growth, and processing (Almeida et al., 2019; Paasonen et al., 2018; Sun et al., 2018; Wang et al., 2018; Wu et al., 2017). Houston, TX is a large metropolitan area with abundant emission sources including traffic, industrial, and biogenic (Prisle et al., 2010; S. Shrestha et al., 2022a). It is found aerosol processes are influenced by land-sea cycling and convective storms (Ekman et al., 2007; Sauter et al., 2019; P. Shrestha et al., 2022; S. Shrestha et al., 2022b; Tsai et al., 2011). There have been several studies to relate the sources, compositions, transportation, and chemical process to the atmospheric aerosol growth in Houston (Al-Naiema et al., 2018; Bahreini et al., 2009; Clark et al., 2017; Dai et al., 2019).

The TRACER campaign was a comprehensive field study that took place between April 2021 and September 2022 in Houston, Texas. The TRACER campaign was designed to

build upon the findings of previous field studies in the region, such as the 2006 Texas Air Quality – Gulf of Mexico Atmospheric Composition and Climate Study (TexAQS – GoMACCS) and the NASA's DISCOVER-AQ and Southern Oxidant and Aerosol Study (SOAS) in 2013. It aims to provide new insights to investigate the convective cloud life cycles and aerosol-convection interactions.

The objective of TRACER-MAP was to investigate the spatial characteristics of aerosol properties through a series of aerosol, gas, and meteorological measurements. To achieve this goal, the Mobile Air Quality Laboratory 2 (MAQL2) was stationed at five different sites across the Houston metropolitan area, including La Porte, University of Houston, San Jacinto Battleground, Aldine, and Jones Forest. These sites were selected to capture various emissions scenarios, including biogenic, industrial, and urban emissions, under different meteorological conditions. Aerosol growth events were discussed with a range of observations, including CCN concentration, aerosol optical properties, and meteorological properties, to better understand the underlying aerosol processes.

5.2. Methods

5.2.1. Sites Description

Five different field sites across the Houston metropolitan area were selected to capture the unique atmospheric conditions and emissions sources in the Houston metropolitan region. Table 5-1 shows the time and locations MAQL2 visited during the campaign. In order to assess the impact of different emissions scenarios and meteorological conditions on aerosol growth, MAQL2 was stationed at some sites multiple times.

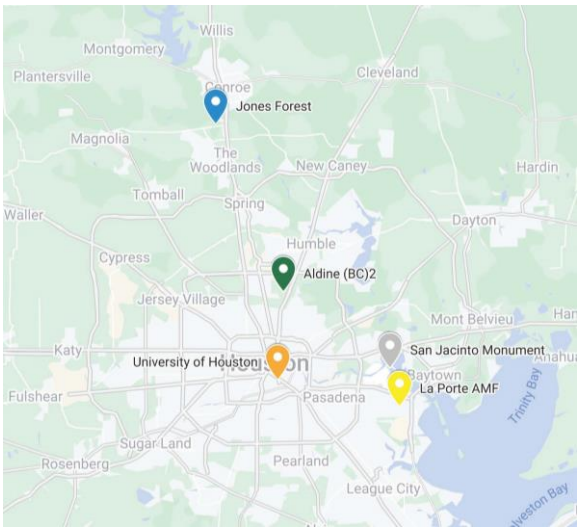

Figure 5-1 Locations of the five sites.

The La Porte AMF site as the primary site for the TRACER campaign was the location of the ARM Mobile Facility (AMF1). It is close to Trinity Bay and the Gulf of Mexico and consists of a comprehensive suite of aerosol, cloud, and meteorological properties instrumentation. This site is located near La Porte Municipal Airport, which is about 4 km south of an industrial area. The La Porte site has been the focus of several previous studies, including the 2006 Texas Air Quality – Gulf of Mexico Atmospheric Composition and Climate Study (TexAQS – GoMACCS) and NASA's DISCOVER-AQ and Southern Oxidant and Aerosol Study (SOAS) in 2013. The particle number distribution, total aerosol concentration, and CCN concentration measured by MAQL2 were compared to the AMF1 Aerosol Observing System measurement for validation.

The Aldine field site is located about 15 km north-northeast of downtown Houston, situated in a suburban environment, and is exposed to a diverse mix of urban, industrial, and biogenic emissions.

The University of Houston (UH) site is about 4 km southeast of downtown, near I-45. It was selected to capture the emissions from urban sources, such as transportation, commercial, residential, railyard, and local industry.

The San Jacinto Battleground site is located north of an industrial park about 10 km north-northwest of the AMF site, surrounded by Houston Ship Channel which includes Port Houston, the largest Gulf Coast container port and tanker terminals, and related industrial facilities in the US by water tonnage.

The Jones Forest site is located in a forested area about 54 km north-northwest of Houston and was selected to capture the effects of forested environments with a mixed pine-hardwood forest dominated by Loblolly pines.

Table 5-1 List of sample sites

Site	Aldine	University of Houston	Battleground	Aldine	Jones Forest	AMF1	University of Houston	Aldine	Jones Forest
Time	7.3 – 7.8	7.8 – 7.16	7.16 – 7.21	7.21 – 7.26	7.26 – 8.1	8.1 – 8.8	8.8 – 8.15	8.15 – 8.24	8.24 – 8.31

5.2.2. Instrumentations

The platform for TRACER-MAP is the University of Houston/Rice University/Baylor University Mobile Air Quality Laboratory 2 (MAQL2). It is a 22 m^3 insulated air-conditioned trailer equipped with a full suite of measurements. The instruments involved

in this study are summarized in Table 5-2. The detailed description for MAQL2, aerosol, gas, meteorological and atmospheric measurements can be found in previous studies (Guo et al., 2021; S. Shrestha et al., 2022c). Here the aerosol measurements using a customized Scanning Mobility Particle Sizer, Cloud Condensation Nuclei Counter (CCNc), and Aerodynamic Particle Sizer which are not covered in the previous studies are described below.

Figure 5-2 MAQL2 outer and inner instrumentation.

Table 5-2 List of instrumentation deployed in the MAQL2.

Aerosol	Gas	Met/atmospheric
Scanning Mobility Particle Sizer	Proton transfer reaction mass spectrometer (PTR-MS, Ionicon)	RM Young 86000 ultrasonic anemometer
Cloud Condensation Nuclei Counter (CCN-100, Droplet Measurement Technologies)	CO instrument (off-axis integrated cavity output spectroscopy)	RM Young 41382 temperature and relative humidity probe
Aerodynamic Particle Sizer (APS 3321, TSI)	SO_2 instrument with a pulsed fluorescence analyzer (Model 43i-TL, Thermo Environmental, Inc.)	61302V barometric pressure sensor
Aerodyne high-resolution time-of-flight aerosol mass spectrometer (HR-ToF-AMS)	Ozone monitor that has been modified to measure O3 via chemiluminescence (CL) with NO (Model 42C, Thermo Environmental, Inc.)	Meterologie Consult, GmbH filter radiometer for jNO_2
Brechtel tricolor absorption photometers (365, 520, and 640 nm)	High-sensitivity NO_x instrument, using CL to detect NO and photolysis and CL to measure NO_2 (Air Quality Designs, Inc.)	Ceilometer (Vaisala CL-31)
Condensation Particle Counter (MAGIC CPC, Aerosol Devices)	Molybdenum oxide catalytic converter and subsequent CL (Model 42i, Thermo Environmental, Inc.) for total NO_y	Garmin 19x HVS GPS receiver
TSI 3563 nephelometer (for 450, 550, and 700 nm)		

5.2.2.1. Aerosol Size Distribution Measurement

The particle size distributions were measured from 0.02 to 17 μm using a customized Scanning Mobility Particle Sizer (SMPS) and an aerodynamic particle sizer (APS; TSI 3321). The SMPS comprises a TSI 3762 condensation particle counter (CPC) and a high-flow DMA (Stolzenburg et al., 1998). The sample flow was dried through a Nafion bundle (Perma Pure Inc., USA) upstream of the DMA. The APS was operated in parallel with the SMPS sharing one inlet. The SMPS was calibrated using 0.203 nm polystyrene latex (PSL) particles.

5.2.2.2. Size Resolved CCN Activity Measurement

To measure size-resolved CCN activity, a cloud condensation nuclei counter (CCNc; DMT CCN-100) was utilized alongside the CPC in the SMPS system. The CCNc was set to operate concurrently with the SMPS system so that the total number and CCN concentrations of the size-classified aerosol were simultaneously characterized. The supersaturation was regulated that stepped at 0.15%, 0.47%, and 0.64% by controlling a temperature gradient sequence. Each supersaturation level persisted for approximately 10 minutes, which corresponded to one scan cycle of the SMPS.

5.2.3. Data Analysis

5.2.3.1. Size Distribution

The aerosol size distribution was derived by inverting the particle concentration using a routine described in Collins et al. (2002). The size distributions measured by the two were merged using a LabVIEW program by assuming the density of particles at 1.6 g/cm^3. A basic quality check was performed to remove the outliers, continuing zeros, and invalid data, which are depicted as black bands on the graphs in subsequent sections. During the experiment, a leak was detected upstream of the SMPS system, which was addressed by applying a correction factor to the SMPS size distribution curves to match the overlapped part measured by the APS.

5.2.3.2. Growth Rate

The growth rate was derived from the identified new particle formation events. The time dependent mode diameters were assumed to be the maximum diameter in the

distributions within 5 hours from the start of the new particle formation events. For each identified mode, the growth rate (GR) was calculated as the change in D_p between two successive measurements divided by the time difference.

$$\mathbf{GR} = \frac{\Delta \mathbf{D_p}}{\Delta \mathbf{t}} \quad \textbf{(5- 5)}$$

5.2.3.3. CCN Activity

Particle hygroscopicity is derived using expressions from Petters & Kreidenweis (2007).

$$\boldsymbol{\kappa} = \frac{4\mathbf{A}^3}{27\mathbf{D_p^3 ln^2 S_c}} \quad \textbf{(5- 6)}$$

$$\mathbf{A} = \frac{4\boldsymbol{\sigma}\mathbf{M_w}}{\mathbf{RT}\boldsymbol{\rho}_\mathbf{w}} \quad \textbf{(5- 7)}$$

Where D_p is the critical dry diameter of the aerosol species at supersaturation S_c, σ is the surface tension of the drop which is assumed to be that of water, R is the ideal gas constant, and M_w and ρ_w are the molecular weight and density of water, respectively.

5.3. Results and Discussion

5.3.1. Particle Number Size Distributions

Number and volume size distributions varied widely from site to site and were influenced by changing meteorological conditions and local emissions. Figure 5-3 show the time series for the number and volume distribution throughout the entire campaign with labels on the top indicating the sites. The average number and volume size distribution for the different sites are shown in Figure 5-3.

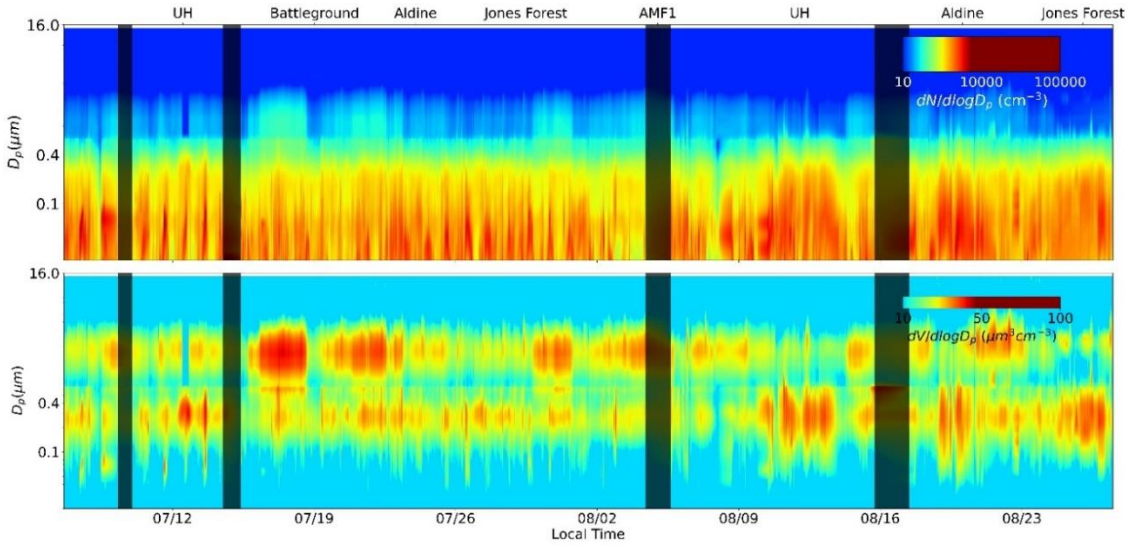

Figure 5-3 Times series of the number and volume distributions throughout the campaign.

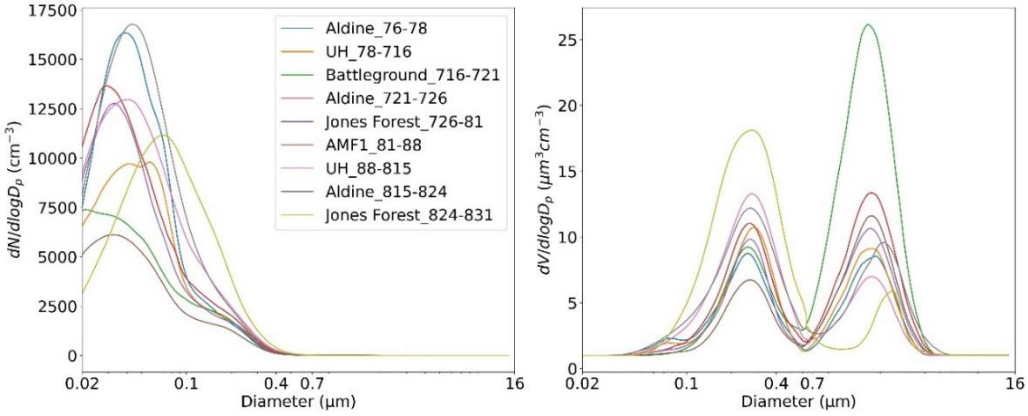

Figure 5-4 Times series of the number (left) and volume (right) distributions throughout the campaign.

A single mode is observed in the averaged number size distribution across all sites, which is consistent with previous research indicating that urban aerosols are typically characterized by a single mode (T. Wu & Boor, 2021). The shapes of the distributions are similar across all sites, with peaks falling between 30 and 50 nm. The Aldine site, which is heavily influenced by local traffic and industrial emissions, has the highest number

concentration. The average volume distributions at all sites exhibit dual modes, with one centered at approximately 0.3 μm and the other at 1 μm. The Battleground site has the highest volume distribution at around 1 μm, due to a potential dust period that will be discussed later on.

5.3.2. New Particle Formation Events

Table 5-3 provides a summary of new particle formation (NPF) events that occurred during the campaign. NPF events were mainly observed in the morning between 9 and 12 AM (local time), indicating the significance of photochemistry in the process. The UH site had the highest NPF frequency of 0.87, which occurred between July 8th and 16th. However, during the second visit, the frequency of NPF events at the UH site was not as high, suggesting the temporal variability of regional NPF. Urban sites, such as UH and Aldine, had more frequent NPF events than other sites.

The average growth rate (GR) of particles at all sites was 4.4 nm hr^{-1}, with the UH site having the highest GR of 8.3 nm hr^{-1}. The observed GR in this study was slower than the 10 nm hr^{-1} measured at Houston in 2009 during the SHARP/SOOT campaign (Levy et al., 2013).

Table 5-3 New particle formation event summary

Site	Stay time	NPF frequency	NPF start time CDT	Average GR (nm hr^{-1})	Max D_p (nm)
Aldine	7/6 – 7/8	0.50	7/7 9:17	4.1	71.8
UH	7/8 – 7/16	0.86	7/10 11:22	4.4	44.7
			7/11 8:58	5.4	62.3
			7/12 11:34	7.1	62.3
			7/13 11:54	8.3	71.8
			7/14 10:25	2.2	32.1
			7/16 10:35	4.2	71.8
Battleground	7/16 – 7/21	0			
Aldine	7/21 – 7/26	0.20	7/25 10:39	3.9	42.6
Jones Forest	7/26 – 8/1	0.80	7/27 10:55	3.5	40.7
			7/28 11:36	2.8	37.0
			7/30 12:12	8.1	68.5
			7/31 11:50	2.6	40.7
AMF	8/1 – 8/8	0			
UH	8/8 – 7/16	0.33	8/9 10:49	3.1	32.1
			8/10 10:34	5.5	71.8
Aldine	8/16 – 8/24	0.38	8/16 10:44	2.8	44.7
			8/18 11:7	5.0	54.0
			8/19 16:38	2.5	49.2
Jones Forest	8/24 – 8/31	0			

5.3.2.1. NPF During Convection

On 18 August 2022, an ambient NPF was recorded by the SMPS beginning around 11 local time (Fig. 5-5). Meanwhile, a storm was approaching from northwest observed by Next Generation Weather Radar (NEXRAD) system, which brought precipitation to Houston area in the night of August 18. The lognormal fit diameters and growth rates for observed modes were presented in Fig. 5-5b, and the NPF event was observed during MAQL2's visit to the Aldine site. Wind direction changed from southwest to southeast,

with wind speed decreasing, as temperature decreased and relative humidity increased, as shown in Fig. 5-5c and 5-5d. A drop in solar intensity and raise in dew point was observed, too (Fig. 5-5e). The Doppler radar operated at the AMF site also recorded convection, as shown in Fig. 5-5f.

The increased solar radiation, indicating active photochemistry, likely played a positive role in the formation of the nucleation mode. In addition, it is reported turbulent fluctuations across temperature and humidity gradient are favorable for nucleation (Nilsson et al., 2001). Another NPF mode occurred in the afternoon of August 19th after strong convection happened throughout the day. The solar intensity was low during the second NPF event. Enhanced trace gases brought to the ground by the convection could be one potential contributor for the nucleation mode (Platis et al., 2016).

Figure 5-5 compares the aerosol number and volume distributions before, during, and after the storm at the same time (19:00 local time). The results showed an increase in the number of smaller particles and also in volume of slightly larger particles after the storm. One possible explanation is that post-convection downdrafts brought lofted aerosol and trace gases to the surface, while wet deposition removed preexisting aerosols. Another possibility is that the storm enhanced atmospheric turbulence and mixing, leading to increased aerosol particle number and size due to coagulation and condensation.

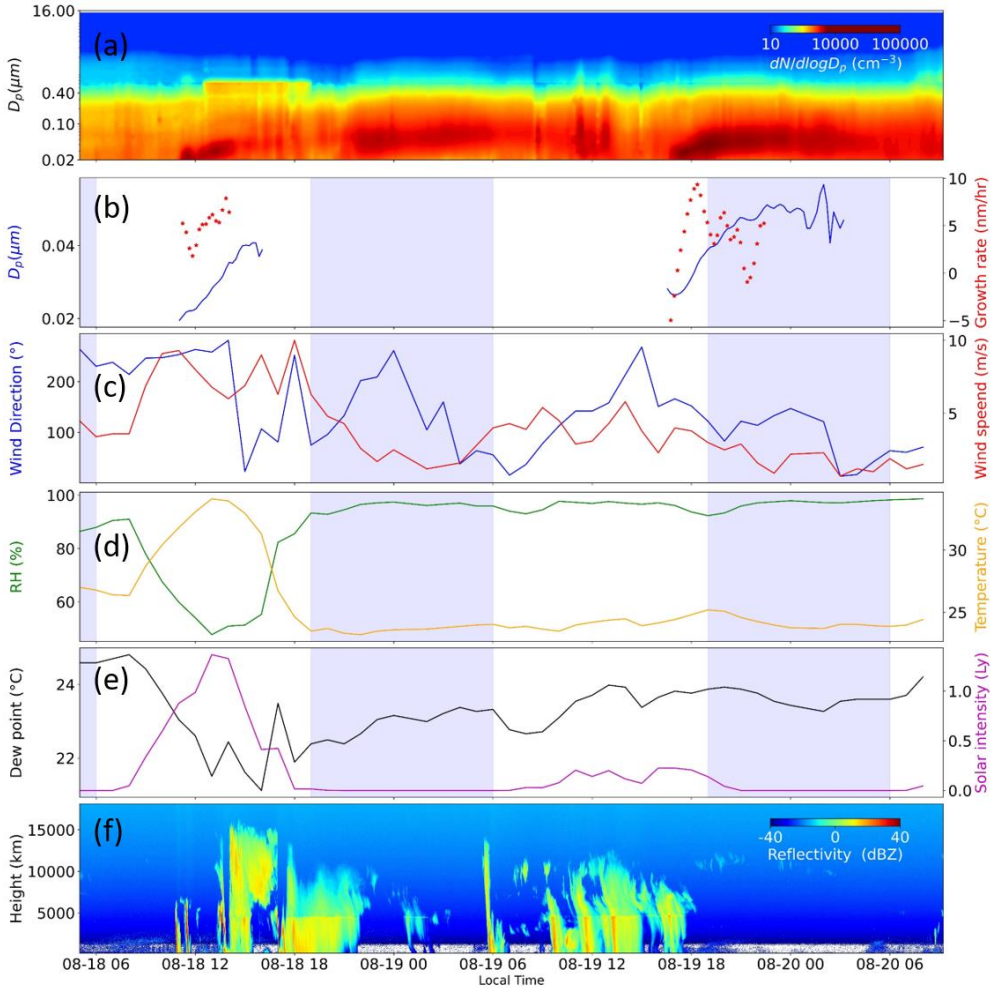

Figure 5-5 (a): Ambient aerosol size distribution time series 2 days during a storm. (b): Time series of the lognormal fit diameters of identified and particle growth rates calculated correspondingly. (c): Wind direction and wind speed. (d): Ambient relative humidity and temperature. (e) Dew point and solar intensity. (f): KAZR reflectivity.

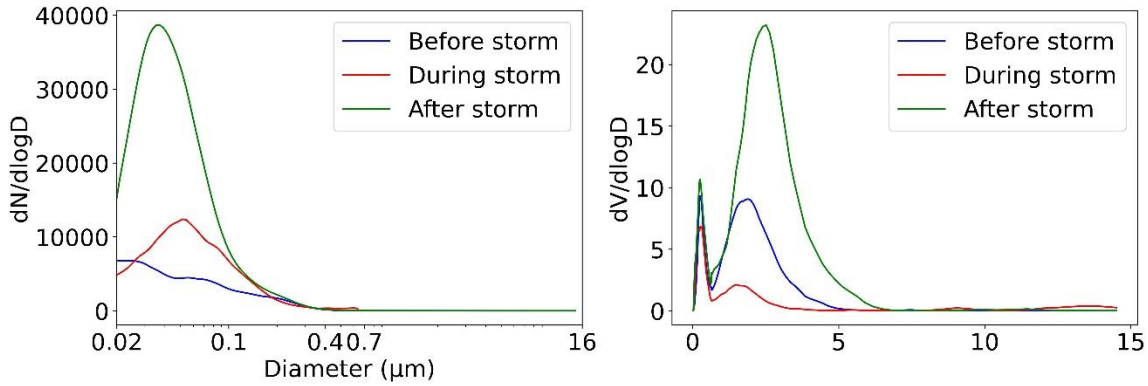

Figure 5-6 Number and volume size distributions before, during, and after the storm.

5.3.3. Supermicron Particles

The temporal trends of the total volume concentration in the size range of 0.5 to 20.1 μm, as measured by APS at MAQL2 and AMF, are presented in Figure 5-7. Despite some sites visited by MAQL2 being far away from AMF, the trends measured by both sites are similar, indicating that the increase in supermicron particles is likely a regional event rather than a result of local emissions. The average number and volume concentrations measured by MAQL2 and AMF1 are 18.8 and 10.2 cm^3, and 18.6 and 11.1 μm^3 cm^3, respectively. The higher concentration observed by MAQL2 may suggest a higher concentration from urban Houston in the northwestern area to the coastal area.

In Figure 5-8, a comprehensive analysis was conducted using aerosol optical properties, including scattering and absorption coefficients, as well as single scattering albedo. The results showed a considerable increase in the scattering coefficient, which was closely associated with the enhancement in particle number and volume concentration. On the other hand, the absorption coefficient exhibited a relatively smaller increase. This suggests that the sources of the supermicron particles were more likely to be non-

absorbing aerosols, such as sulfate and sea salt, rather than absorbing ones like black carbon.

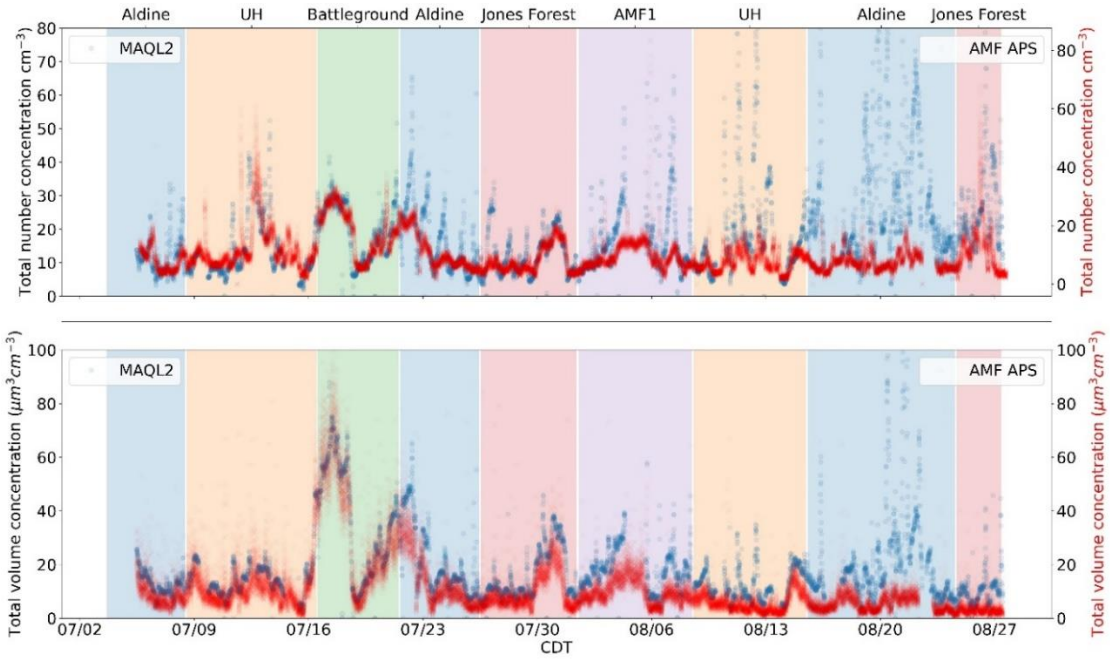

Figure 5-7 Comparisons of time series of the total number and volume concentration measured by MAQL2 and AMF.

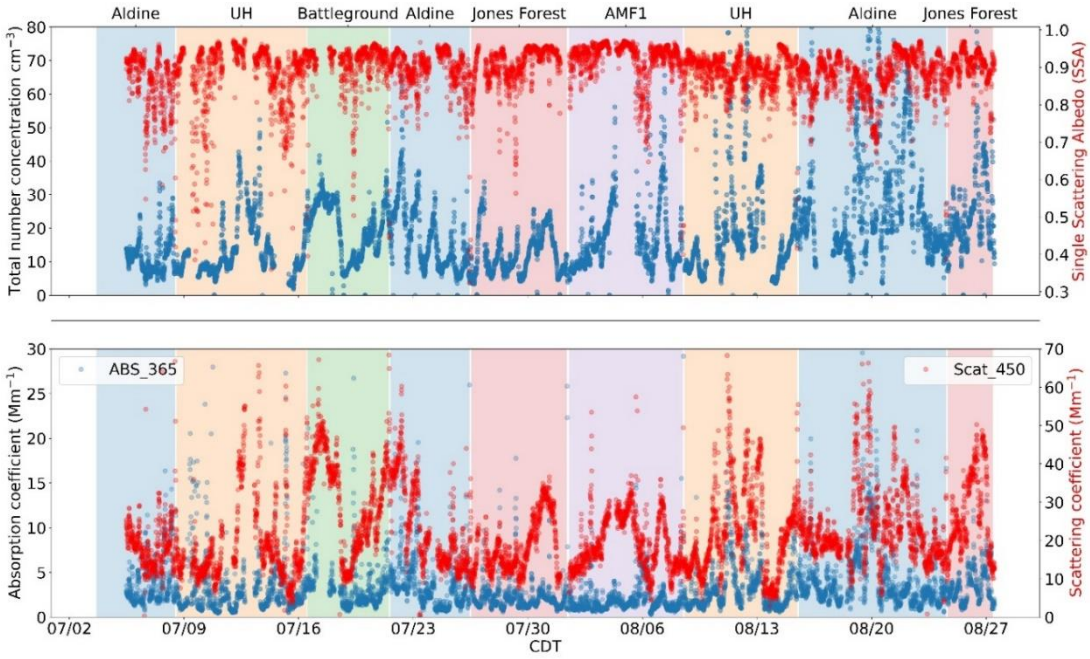

Figure 5-8 (Top) Time series of the total number concentration measured by MAQL2 and Single Scattering Albedo (SSA). (Bottom) Time series of the absorption and scattering coefficient at 365 and 450 nm.

5.3.4. CCN Activity

Figure 5-9 displays the hygroscopicity coefficient κ and critical dry diameter Dp_50 at supersaturation Sc of 0.15, 0.37, and 0.64 for various sites. As expected, aerosols have a larger hygroscopicity coefficient and critical dry diameter at lower Sc for all sites with sufficient data. The κ for all sites falls mainly within the 0.1 to 0.4 range, indicating that the majority of aerosols have moderate hygroscopicity, such as salts, rather than inhygroscopic compounds like organic. The AMF1 location displays the greatest mean κ value at 0.26, whereas the Jones Forest exhibits the lowest at 0.15. This aligns with the anticipated outcome that the biogenic source is more prevalent at the Jones Forest site. Figure 5-10 illustrates the diurnal cycle of averaged κ at different sites, revealing significant variability between sites and supersaturations. Some sites, such as

Battleground and AMF1, exhibit higher κ around noon, while the Jones Forest site maintains a consistent κ throughout the day. The difference may be attributed to the stable isolated source and more abundant SOA at Jones Forest, while the remaining sites are more influenced by local emissions. The differentiation of diurnal patterns across various sites accentuates the distinct sources and circumstances specific to each location. At lower supersaturation of 0.15, hygroscopicity displays a greater time of day dependency than at larger supersaturations. The value of κ was found to be greater at lower supersaturation levels, while there was little difference between the κ values at supersaturation levels of 0.37 and 0.64. Additionally, it was observed that κ values at the two supersaturation levels often became similar in the afternoon, indicating the composition kept stable with particle growing and is relative hygroscopic.

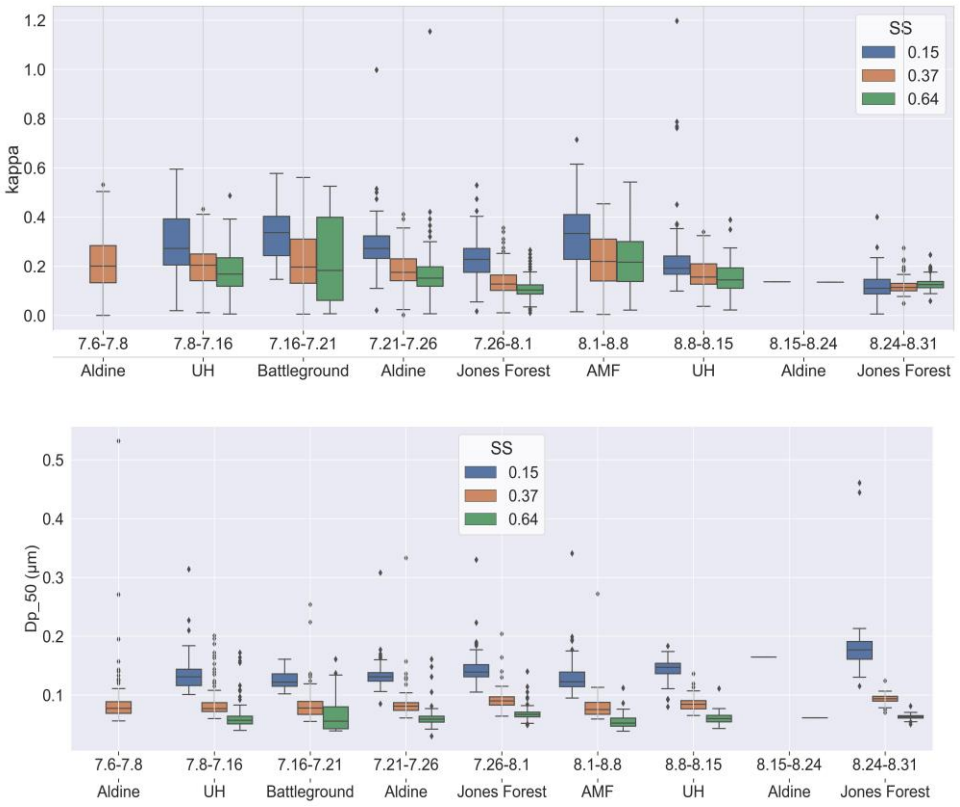

Figure 5-9 The summary of the hygroscopicity coefficient κ and critical dry diameter Dp_50 at supersaturation Sc of 0.15, 0.37, and 0.64 for different sites.

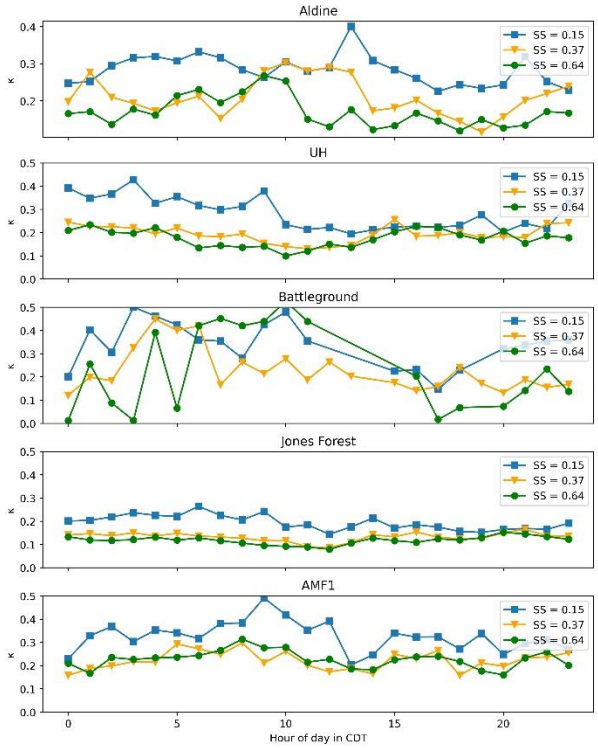

Figure 5-10 Diurnal cycle of averaged hygroscopicity coefficient κ at different sites.

5.4. Conclusions

Between July and August of 2022, the TRACER-MAP campaign utilized the Baylor-UH-Rice-UCR Mobile Air Quality Laboratory (MAQL2) to gather aerosol, volatile organic compounds, trace gas, and meteorological data across Houston. This study focused on aerosol measurements obtained from five sites: La Porte, University of Houston, San Jacinto Battleground, Aldine, and Jones Forest.

The aerosol size distribution was unimodal across all sites, with the highest concentration observed in urban and biogenic environments. The volume distributions were bimodal, with the highest volume concentration observed at the Battleground site due to an increase in supermicron particles. These particles were found to be temporally associated

with AMF measurements, with the highest enhancement observed from July 16th to 18th at the Battleground site.

Frequent new particle formation events were observed at UH and Jones Forest sites. Active NPF was observed associated with convections.

The CCN activity was found to decrease as the supersaturation level increased from 0.15 to 0.64, with a small difference between the supersaturation levels of 0.37 and 0.64. The University of Houston, Battleground, and AMF1 sites showed a moderate diurnal cycle, while the Jones Forest site showed consistent hygroscopicity.

5.5. References

Abbafati, C., Abbas, K. M., Abbasi-Kangevari, M., Abd-Allah, F., Abdelalim, A., Abdollahi, M., Abdollahpour, I., Abegaz, K. H., Abolhassani, H., Aboyans, V., Abreu, L. G., Abrigo, M. R. M., Abualhasan, A., Abu-Raddad, L. J., Abushouk, A. I., Adabi, M., Adekanmbi, V., Adeoye, A. M., Adetokunboh, O. O., … Murray, C. J. L. (2020). Global burden of 87 risk factors in 204 countries and territories, 1990–2019: a systematic analysis for the Global Burden of Disease Study 2019. *The Lancet*, *396*(10258), 1223–1249. https://doi.org/10.1016/S0140-6736(20)30752-2

Akimoto, H., Nagashima, T., Li, J., Fu, J. S., Ji, D., Tan, J., & Wang, Z. (2019). Comparison of surface ozone simulation among selected regional models in MICS-Asia III - Effects of chemistry and vertical transport for the causes of difference. *Atmospheric Chemistry and Physics*, *19*(1), 603–615. https://doi.org/10.5194/acp-19-603-2019

Aldhafeeri, T., Tran, M. K., Vrolyk, R., Pope, M., & Fowler, M. (2020). A review of methane gas detection sensors: Recent developments and future perspectives. In *Inventions* (Vol. 5, Issue 3, pp. 1–18). MDPI Multidisciplinary Digital Publishing Institute. https://doi.org/10.3390/inventions5030028

Almeida, G. P., Bittencourt, A. T., Evangelista, M. S., Vieira-Filho, M. S., & Fornaro, A. (2019). Characterization of aerosol chemical composition from urban pollution in Brazil and its possible impacts on the aerosol hygroscopicity and size distribution. *Atmospheric Environment*, *202*, 149–159. https://doi.org/10.1016/j.atmosenv.2019.01.024

Al-Naiema, I. M., Hettiyadura, A. P. S., Wallace, H. W., Sanchez, N. P., Madler, C. J., Karakurt Cevik, B., Bui, A. A. T., Kettler, J., Griffin, R. J., & Stone, E. A. (2018). Source apportionment of fine particulate matter in Houston, Texas: Insights to secondary organic aerosols. *Atmospheric Chemistry and Physics*, *18*(21), 15601–15622. https://doi.org/10.5194/acp-18-15601-2018

Andersen, T., Scheeren, B., Peters, W., & Chen, H. (2018). A UAV-based active AirCore system for measurements of greenhouse gases. *Atmospheric Measurement Techniques*, *11*(5), 2683–2699. https://doi.org/10.5194/amt-11-2683-2018

Area, U., Ye, J., Batista, C., Barbosa, R., & Ribeiro, I. (n.d.). *Vertical Profiles of Ozone Concentration Collected by an Unmanned Aerial Vehicle and the Mixing of the Nighttime Boundary Layer over an Amazonian*. 1–14.

Bahreini, R., Ervens, B., Middlebrook, A. M., Warneke, C., de Gouw, J. A., DeCarlo, P. F., Jimenez, J. L., Brock, C. A., Neuman, J. A., Ryerson, T. B., Stark, H., Atlas, E., Brioude, J., Fried, A., Holloway, J. S., Peischl, J., Richter, D., Walega, J., Weibring, P., … Fehsenfeid, F. C. (2009). Organic aerosol formation in urban and industrial plumes near Houston and Dallas, Texas. *Journal of Geophysical Research Atmospheres*, *114*(16). https://doi.org/10.1029/2008JD011493

Boy, M., Mogensen, D., Smolander, S., Zhou, L., Nieminen, T., Paasonen, P., Plass-Dülmer, C., Sipilä, M., Petäjä, T., Mauldin, L., Berresheim, H., & Kulmala, M. (2013). Oxidation of SO₂ by stabilized Criegee intermediate (sCI) radicals as a crucial source for atmospheric sulfuric acid concentrations. *Atmospheric Chemistry and Physics*, *13*(7), 3865–3879. https://doi.org/10.5194/acp-13-3865-2013

Brosy, C., Krampf, K., Zeeman, M., Wolf, B., Junkermann, W., Schäfer, K., Emeis, S., & Kunstmann, H. (2017). Simultaneous multicopter-based air sampling and sensing of meteorological variables. *Atmospheric Measurement Techniques*, *10*(8), 2773–2784. https://doi.org/10.5194/amt-10-2773-2017

Byun, D., & Schere, K. L. (2006). Review of the governing equations, computational algorithms, and other components of the models-3 Community Multiscale Air Quality (CMAQ) modeling system. In *Applied Mechanics Reviews*. https://doi.org/10.1115/1.2128636

Carter, W. P. L. (2010). Development of the SAPRC-07 chemical mechanism. *Atmospheric Environment*. https://doi.org/10.1016/j.atmosenv.2010.01.026

C., A. S., W., H. L., Q., T. D., & Jason, W. J. (2010). An Estimate of the Global Burden of Anthropogenic Ozone and Fine Particulate Matter on Premature Human Mortality Using Atmospheric Modeling. *Environmental Health Perspectives*, *118*(9), 1189–1195. https://doi.org/10.1289/ehp.0901220

Chen, Q., Wang, D., Li, X., Li, B., Song, R., He, H., & Peng, Z. (n.d.). *Vertical Characteristics of Winter Ozone Distribution within the Boundary Layer in Shanghai Based on Hexacopter Unmanned Aerial Vehicle Platform*.

Clark, A. E., Yoon, S., Sheesley, R. J., & Usenko, S. (2017). Spatial and Temporal Distributions of Organophosphate Ester Concentrations from Atmospheric Particulate Matter Samples Collected across Houston, TX. *Environmental Science and Technology*, *51*(8), 4239–4247. https://doi.org/10.1021/acs.est.7b00115

Collins, D. R., Flagan, R. C., & Seinfeld, J. H. (2002). Improved inversion of scanning DMA data. *Aerosol Science and Technology*, *36*(1), 1–9. https://doi.org/10.1080/027868202753339032

Cuchiara, G. C., Li, X., Carvalho, J., & Rappenglück, B. (2014). Intercomparison of planetary boundary layer parameterization and its impacts on surface ozone concentration in the WRF/Chem model for a case study in houston/texas. *Atmospheric Environment*, *96*, 175–185. https://doi.org/10.1016/j.atmosenv.2014.07.013

Dai, Q., Schulze, B. C., Bi, X., Bui, A. A. T., Guo, F., Wallace, H. W., Sanchez, N. P., Flynn, J. H., Lefer, B. L., Feng, Y., & Griffin, R. J. (2019). Seasonal differences in formation processes of oxidized organic aerosol near Houston, TX. *Atmospheric Chemistry and Physics*, *19*(14), 9641–9661. https://doi.org/10.5194/acp-19-9641-2019

Demali, G. (n.d.). *Developing a UAS-Deployable Methane Sensor Using Low-Cost Developing a UAS-Deployable Methane Sensor Using Low-Cost Modular Open-Source Components Modular Open-Source Components*. https://ideaexchange.uakron.edu/honors_research_projects

Duren, R. M., Thorpe, A. K., Foster, K. T., Rafiq, T., Hopkins, F. M., Yadav, V., Bue, B. D., Thompson, D. R., Conley, S., Colombi, N. K., Frankenberg, C., McCubbin, I. B., Eastwood, M. L., Falk, M., Herner, J. D., Croes, B. E., Green, R. O., & Miller, C. E. (2019). California's methane super-emitters. *Nature*, *575*(7781), 180–184. https://doi.org/10.1038/s41586-019-1720-3

Ekman, A. M. L., Engström, A., & Wang, C. (2007). The effect of aerosol composition and concentration on the development and anvil properties of a continental deep convective cloud. *Quarterly Journal of the Royal Meteorological Society*, *133*(627), 1439–1452. https://doi.org/10.1002/qj.108

Falabella, A. D., Wallin, D. O., & Lund, J. A. (2018). Application of a customizable sensor platform to detection of atmospheric gases by UAS. *2018 International Conference on Unmanned Aircraft Systems, ICUAS 2018*, 883–890. https://doi.org/10.1109/ICUAS.2018.8453480

Fast, J. D., Allan, J., Bahreini, R., Craven, J., Emmons, L., Ferrare, R., Hayes, P. L., Hodzic, A., Holloway, J., Hostetler, C., Jimenez, J. L., Jonsson, H., Liu, S., Liu, Y., Metcalf, A., Middlebrook, A., Nowak, J., Pekour, M., Perring, A., … Zhang, Q. (2014). Modeling regional aerosol and aerosol precursor variability over California and its sensitivity to emissions and long-range transport during the 2010 CalNex and

CARES campaigns. *Atmospheric Chemistry and Physics*, *14*(18), 10013–10060. https://doi.org/10.5194/acp-14-10013-2014

Fox, T. A., Barchyn, T. E., Risk, D., Ravikumar, A. P., & Hugenholtz, C. H. (2019). Erratum: A review of close-range and screening technologies for mitigating fugitive methane emissions in upstream oil and gas (Environmental Research Letters (2019) 14 (053002) DOI: 10.1088/1748-9326/ab0cc3). In *Environmental Research Letters* (Vol. 14, Issue 6). Institute of Physics Publishing. https://doi.org/10.1088/1748-9326/ab20f1

Gaudel, A., Cooper, O. R., Ancellet, G., Barret, B., Boynard, A., Burrows, J. P., Clerbaux, C., Coheur, P. F., Cuesta, J., Cuevas, E., Doniki, S., Dufour, G., Ebojie, F., Foret, G., Garcia, O., Granados-Muñoz, M. J., Hannigan, J. W., Hase, F., Hassler, B., … Ziemke, J. (2018). Tropospheric Ozone Assessment Report: Present-day distribution and trends of tropospheric ozone relevant to climate and global atmospheric chemistry model evaluation. *Elementa*, *6*(May). https://doi.org/10.1525/elementa.291

Goldberg, L. J. (1971). Environment, Aerosol Facility67rai7) (A /AH) =-mgdt/6iraqH (1) where H = height of chamber, a = radius of particle, A = cross sectional area of chamber, C = aerosol particulate concentration, v = Stokes velocity, m = mass of particle (4/3ira3d), d = density of particle, g = gravitational con-stant, Xj = viscosity of air, and where the term “mg/6ira-q” defines the Stokes velocity of free fall. In *APPLIED MICROBIOLOGY* (Vol. 21, Issue 2). https://journals.asm.org/journal/am

Golston, L. M., Tao, L., Brosy, C., Schäfer, K., Wolf, B., McSpiritt, J., Buchholz, B., Caulton, D. R., Pan, D., Zondlo, M. A., Yoel, D., Kunstmann, H., & McGregor, M. (2017). Lightweight mid-infrared methane sensor for unmanned aerial systems. *Applied Physics B: Lasers and Optics*, *123*(6). https://doi.org/10.1007/s00340-017-6735-6

Guo, F., Bui, A. A. T., Schulze, B. C., Yoon, S., Shrestha, S., Wallace, H. W., Sakai, Y., Actkinson, B. W., Erickson, M. H., Alvarez, S., Sheesley, R., Usenko, S., Flynn, J., & Griffin, R. J. (2021). Urban core-downwind differences and relationships related to ozone production in a major urban area in Texas. *Atmospheric Environment*, *262*. https://doi.org/10.1016/j.atmosenv.2021.118624

Guo, J. J., Fiore, A. M., Murray, L. T., Jaffe, D. A., Schnell, J. L., Moore, C. T., & Milly, G. P. (2018). Average versus high surface ozone levels over the continental USA: Model bias, background influences, and interannual variability. *Atmospheric Chemistry and Physics*, *18*(16), 12123–12140. https://doi.org/10.5194/acp-18-12123-2018

Guo, Y., Zhang, J., An, J., Qu, Y., Liu, X., & Sun, Y. (2020). *Effect of vertical parameterization of a missing daytime source of HONO on concentrations of HONO , O 3 and secondary organic aerosols in eastern China*. *226*(June 2019). https://doi.org/10.1016/j.atmosenv.2019.117208

Hao, L., Garmash, O., Ehn, M., Miettinen, P., Massoli, P., Mikkonen, S., Jokinen, T., Roldin, P., Aalto, P., Yli-Juuti, T., Joutsensaari, J., Petäjä, T., Kulmala, M., Lehtinen, K. E. J., Worsnop, D. R., & Virtanen, A. (2018). Combined effects of boundary layer dynamics and atmospheric chemistry on aerosol composition during new particle formation periods. *Atmospheric Chemistry and Physics*, *18*(23), 17705–17716. https://doi.org/10.5194/acp-18-17705-2018

Heikenfeld, M., White, B., Labbouz, L., & Stier, P. (n.d.). *Aerosol effects on deep convection: The propagation of aerosol perturbations through convective cloud microphysics*.

Hirsikko, A., Vakkari, V., Tiitta, P., Manninen, H. E., Gagné, S., Gagné, S., Laakso, H., Kulmala, M., Mirme, A., Mirme, S., Mabaso, D., Beukes, J. P., & Laakso, L. (2012). Characterisation of sub-micron particle number concentrations and formation events in the western Bushveld Igneous Complex, South Africa. *Atmospheric Chemistry and Physics*, *12*(9), 3951–3967. https://doi.org/10.5194/acp-12-3951-2012

Hodshire, A. L., Lawler, M. J., Zhao, J., Ortega, J., Jen, C., Yli-juuti, T., Brewer, J. F., Kodros, J. K., Barsanti, K. C., Hanson, D. R., Mcmurry, P. H., Smith, J. N., & Pierce, J. R. (2016). *Multiple new-particle growth pathways observed at the US DOE Southern Great Plains field site*. 9321–9348. https://doi.org/10.5194/acp-16-9321-2016

Hong, S. Y., Noh, Y., & Dudhia, J. (2006). A new vertical diffusion package with an explicit treatment of entrainment processes. *Monthly Weather Review*. https://doi.org/10.1175/MWR3199.1

Huang, M., Huang, B., & Huang, A. H. (2014). Implementation of 5-layer thermal diffusion scheme in weather research and forecasting model with Intel Many Integrated Cores. *High-Performance Computing in Remote Sensing IV*. https://doi.org/10.1117/12.2069426

Huang, W., Saathoff, H., Shen, X., Ramisetty, R., Leisner, T., & Mohr, C. (2019). Chemical Characterization of Highly Functionalized Organonitrates Contributing to

Night-Time Organic Aerosol Mass Loadings and Particle Growth. *Environmental Science and Technology*, *53*(3), 1165–1174. https://doi.org/10.1021/acs.est.8b05826

Hu, J., Howard, C. J., Mitloehner, F., Green, P. G., & Kleeman, M. J. (2012). Mobile source and livestock feed contributions to regional ozone formation in central California. *Environmental Science and Technology*, *46*(5), 2781–2789. https://doi.org/10.1021/es203369p

Iwaszenko, S., Kalisz, P., Słota, M., & Rudzki, A. (2021). Detection of natural gas leakages using a laser-based methane sensor and uav. *Remote Sensing*, *13*(3), 1–16. https://doi.org/10.3390/rs13030510

Jerrett, M., Burnett, R. T., Pope, C. A., Ito, K., Thurston, G., Krewski, D., Shi, Y., Calle, E., & Thun, M. (2009). Long-Term Ozone Exposure and Mortality. *New England Journal of Medicine*, *360*(11), 1085–1095. https://doi.org/10.1056/nejmoa0803894

Jha, R. K. (2022). Non-Dispersive Infrared Gas Sensing Technology: A Review. In *IEEE Sensors Journal* (Vol. 22, Issue 1, pp. 6–15). Institute of Electrical and Electronics Engineers Inc. https://doi.org/10.1109/JSEN.2021.3130034

Jose Granados-Munõz, M., & Leblanc, T. (2016). Tropospheric ozone seasonal and long-term variability as seen by lidar and surface measurements at the JPL-Table Mountain Facility, California. *Atmospheric Chemistry and Physics*, *16*(14), 9299–9319. https://doi.org/10.5194/acp-16-9299-2016

Kalivitis, N., Kerminen, V., Kouvarakis, G., Stavroulas, I., Bougiatioti, A., Nenes, A., & Manninen, H. E. (2015). *Atmospheric new particle formation as a source of CCN in the*. 9203–9215. https://doi.org/10.5194/acp-15-9203-2015

Karion, A., Sweeney, C., Tans, P., & Newberger, T. (2010). AirCore: An innovative atmospheric sampling system. *Journal of Atmospheric and Oceanic Technology*, *27*(11), 1839–1853. https://doi.org/10.1175/2010JTECHA1448.1

Kerminen, V. (2018). *Atmospheric new particle formation and growth : review of field observations Atmospheric new particle formation and growth : review of fi eld observations*.

Kulmala, M., Petäjä, T., Ehn, M., Thornton, J., Sipilä, M., Worsnop, D. R., & Kerminen, V. M. (2014). Chemistry of atmospheric nucleation: On the recent advances on precursor characterization and atmospheric cluster composition in connection with atmospheric new particle formation. *Annual Review of Physical Chemistry*, *65*, 21–37. https://doi.org/10.1146/annurev-physchem-040412-110014

Levy, M. E., Zhang, R., Khalizov, A. F., Zheng, J., Collins, D. R., Glen, C. R., Wang, Y., Yu, X. Y., Luke, W., Jayne, J. T., & Olaguer, E. (2013). Measurements of submicron aerosols in Houston, Texas during the 2009 SHARP field campaign. *Journal of Geophysical Research Atmospheres*, *118*(18), 10,518-10,534. https://doi.org/10.1002/jgrd.50785

Lin, J.-T., & McElroy, M. B. (2010). Impacts of boundary layer mixing on pollutant vertical profiles in the lower troposphere: Implications to satellite remote sensing. *Atmospheric Environment*, *44*(14), 1726–1739. https://doi.org/10.1016/j.atmosenv.2010.02.009

Liu, J., Alexander, L., Fast, J. D., Lindenmaier, R., & Shilling, J. E. (2021). *Aerosol characteristics at the Southern Great Plains site during the HI-SCALE campaign*. 5101–5116.

Li, X., & Rappenglueck, B. (2018). A study of model nighttime ozone bias in air quality modeling. *Atmospheric Environment*, *195*(September), 210–228. https://doi.org/10.1016/j.atmosenv.2018.09.046

Marinescu, P. J., Levin, E. J. T., Collins, D., Kreidenweis, S. M., & Heever, S. C. van den. (2019). *Quantifying aerosol size distributions and their temporal variability in the Southern Great Plains , USA*. 11985–12006.

McHale, L. E., Hecobian, A., & Yalin, A. P. (2016). Open-path cavity ring-down spectroscopy for trace gas measurements in ambient air. *Optics Express*, *24*(5), 5523. https://doi.org/10.1364/oe.24.005523

Mena-Carrasco, M., Tang, Y., Carmichael, G. R., Chai, T., Thongbongchoo, N., Campbell, J. E., Kulkarni, S., Horowitz, L., Vukovich, J., Avery, M., Brune, W., Dibb, J. E., Emmons, L., Flocke, F., Sachse, G. W., Tan, D., Shetter, R., Talbot, R. W., Streets, D. G., … Blake, D. (2007). Improving regional ozone modeling through systematic evaluation of errors using the aircraft observations during the International Consortium for Atmospheric Research on Transport and Transformation. *Journal of Geophysical Research*, *112*(D12), D12S19. https://doi.org/10.1029/2006JD007762

Paasonen, P., Peltola, M., Kontkanen, J., Junninen, H., Kerminen, V. M., & Kulmala, M. (2018). Comprehensive analysis of particle growth rates from nucleation mode to cloud condensation nuclei in boreal forest. *Atmospheric Chemistry and Physics*, *18*(16), 12085–12103. https://doi.org/10.5194/acp-18-12085-2018

Parworth, C., Fast, J., Mei, F., Shippert, T., Sivaraman, C., Tilp, A., Watson, T., & Zhang, Q. (2015). Long-term measurements of submicrometer aerosol chemistry at the Southern Great Plains (SGP) using an Aerosol Chemical Speciation Monitor (ACSM). *Atmospheric Environment*, *106*, 43–55. https://doi.org/10.1016/j.atmosenv.2015.01.060

Petters, M. D., & Kreidenweis, S. M. (2007). *and Physics A single parameter representation of hygroscopic growth and cloud condensation nucleus activity*. 1961–1971.

Prisle, N. L., Raatikainen, T., Laaksonen, A., & Bilde, M. (2010). Surfactants in cloud droplet activation: Mixed organic-inorganic particles. *Atmospheric Chemistry and Physics*, *10*(12), 5663–5683. https://doi.org/10.5194/acp-10-5663-2010

Rahn, D. A., & Mitchell, C. J. (2016). Diurnal climatology of the boundary layer in Southern California using AMDAR temperature and wind profiles. *Journal of Applied Meteorology and Climatology*, *55*(5), 1123–1137. https://doi.org/10.1175/JAMC-D-15-0234.1

Reynolds, R. W., Smith, T. M., Liu, C., Chelton, D. B., Casey, K. S., & Schlax, M. G. (2007). Daily high-resolution-blended analyses for sea surface temperature. *Journal of Climate*. https://doi.org/10.1175/2007JCLI1824.1

Sadeghi, B., Pouyaei, A., Choi, Y., & Rappenglueck, B. (n.d.). *Measurement report: Summertime and wintertime VOCs in Houston: Source apportionment and spatial distribution of source origins*. https://doi.org/10.5194/acp-2021-565

Sauter, K., L'Ecuyer, T. S., van den Heever, S. C., Twohy, C., Heidinger, A., Wanzong, S., & Wood, N. (2019). The Observed Influence of Tropical Convection on the Saharan Dust Layer. *Journal of Geophysical Research: Atmospheres*, *124*(20), 10896–10912. https://doi.org/10.1029/2019JD031365

Seinfeld, J. H., & Wiley, J. (n.d.). *ATMOSPHERIC From Air Pollution to Climate Change SECOND EDITION*.

Shah, A., Pitt, J. R., Ricketts, H., Brian Leen, J., Williams, P. I., Kabbabe, K., Gallagher, M. W., & Allen, G. (2020). Testing the near-field Gaussian plume inversion flux quantification technique using unmanned aerial vehicle sampling. *Atmospheric Measurement Techniques*, *13*(3), 1467–1484. https://doi.org/10.5194/amt-13-1467-2020

Shrestha, P., Mendrok, J., & Brunner, D. (2022). Aerosol characteristics and polarimetric signatures for a deep convective storm over the northwestern part of Europe – modeling and observations. *Atmospheric Chemistry and Physics*, *22*(21), 14095–14117. https://doi.org/10.5194/acp-22-14095-2022

Shrestha, S., Yoon, S., Erickson, M. H., Guo, F., Mehra, M., Bui, A. A. T., Schulze, B. C., Kotsakis, A., Daube, C., Herndon, S. C., Yacovitch, T. I., Alvarez, S., Flynn, J. H., Griffin, R. J., Cobb, G. P., Usenko, S., & Sheesley, R. J. (2022a). Traffic, transport, and vegetation drive VOC concentrations in a major urban area in Texas. *Science of the Total Environment*, *838*. https://doi.org/10.1016/j.scitotenv.2022.155861

Shrestha, S., Yoon, S., Erickson, M. H., Guo, F., Mehra, M., Bui, A. A. T., Schulze, B. C., Kotsakis, A., Daube, C., Herndon, S. C., Yacovitch, T. I., Alvarez, S., Flynn, J. H., Griffin, R. J., Cobb, G. P., Usenko, S., & Sheesley, R. J. (2022b). Traffic, transport, and vegetation drive VOC concentrations in a major urban area in Texas. *Science of the Total Environment*, *838*. https://doi.org/10.1016/j.scitotenv.2022.155861

Shrestha, S., Yoon, S., Erickson, M. H., Guo, F., Mehra, M., Bui, A. A. T., Schulze, B. C., Kotsakis, A., Daube, C., Herndon, S. C., Yacovitch, T. I., Alvarez, S., Flynn, J. H., Griffin, R. J., Cobb, G. P., Usenko, S., & Sheesley, R. J. (2022c). Traffic, transport, and vegetation drive VOC concentrations in a major urban area in Texas. *Science of the Total Environment*, *838*. https://doi.org/10.1016/j.scitotenv.2022.155861

Sirmollo, C., Collins, D., McCormick, J., Milan, C., Erickson, M., Flynn, J., Sheesley, R., Usenko, S., Wallace, H., Bui, A., Griffin, R., Tezak, M., Kinahan, S., & Santarpia, J. (2020). Captive Aerosol Growth and Evolution (CAGE) chamber system to investigate particle growth due to secondary aerosol formation. *Atmospheric Measurement Techniques Discussions*, *December*, 1–28. https://doi.org/10.5194/amt-2020-443

So, S., Park, D. G., Jeong, N., Kim, D., Hwang, J., & Lee, C. (2020). Study on the Simultaneous Measurement of O2 and CO Concentrations in the Exhaust Gas of a Methane/Air Flame Using Tunable Diode Laser Absorption Spectroscopy. *Energy and Fuels*, *34*(3), 3780–3787. https://doi.org/10.1021/acs.energyfuels.9b04357

Stocker, T. F., Qin, D., Plattner, G. K., Tignor, M. M. B., Allen, S. K., Boschung, J., Nauels, A., Xia, Y., Bex, V., & Midgley, P. M. (2013). Climate change 2013 the physical science basis: Working Group I contribution to the fifth assessment report of the intergovernmental panel on climate change. *Climate Change 2013 the*

Physical Science Basis: Working Group I Contribution to the Fifth Assessment Report of the Intergovernmental Panel on Climate Change, *9781107057*, 1–1535. https://doi.org/10.1017/CBO9781107415324

Stolzenburg, M., Kreisberg, N., & Hering, S. (1998). Atmospheric Size Distributions Measured by Differential Mobility Optical Particle Size Spectrometry. *Aerosol Science and Technology*, *29*(5), 402–418. https://doi.org/10.1080/02786829808965579

Sun, Y., Xu, W., Zhang, Q., Jiang, Q., Canonaco, F., Prévôt, A. S. H., Fu, P., Li, J., Jayne, J., Worsnop, D. R., & Wang, Z. (2018). Source apportionment of organic aerosol from 2-year highly time-resolved measurements by an aerosol chemical speciation monitor in Beijing, China. *Atmospheric Chemistry and Physics*, *18*(12), 8469–8489. https://doi.org/10.5194/acp-18-8469-2018

Tang, G., Zhu, X., Xin, J., Hu, B., Song, T., Sun, Y., Zhang, J., Wang, L., Cheng, M., Chao, N., Kong, L., Li, X., & Wang, Y. (2017). *Modelling study of boundary-layer ozone over northern China - Part I : Ozone budget in summer*. *187*, 128–137. https://doi.org/10.1016/j.atmosres.2016.10.017

Travis, K. R., Jacob, D. J., Fisher, J. A., Kim, P. S., Marais, E. A., Zhu, L., Yu, K., Miller, C. C., Yantosca, R. M., Sulprizio, M. P., Thompson, A. M., Wennberg, P. O., Crounse, J. D., st. Clair, J. M., Cohen, R. C., Laughner, J. L., Dibb, J. E., Hall, S. R., Ullmann, K., … Zhou, X. (2016). Why do models overestimate surface ozone in the Southeast United States? *Atmospheric Chemistry and Physics*, *16*(21), 13561–13577. https://doi.org/10.5194/acp-16-13561-2016

Tröstl, J., Chuang, W. K., Gordon, H., Heinritzi, M., Yan, C., Molteni, U., Ahlm, L., Frege, C., Bianchi, F., Wagner, R., Simon, M., Lehtipalo, K., Williamson, C., Craven, J. S., Duplissy, J., Adamov, A., Almeida, J., Bernhammer, A. K., Breitenlechner, M., … Baltensperger, U. (2016). The role of low-volatility organic compounds in initial particle growth in the atmosphere. *Nature*, *533*(7604), 527–531. https://doi.org/10.1038/nature18271

Tsai, H. H., Yuan, C. S., Hung, C. H., Lin, C., & Lin, Y. C. (2011). Influence of Sea-Land Breezes on the Tempospatial Distribution of Atmospheric Aerosols over Coastal Region. *Journal of the Air and Waste Management Association*, *61*(4), 358–376. https://doi.org/10.3155/1047-3289.61.4.358

Turner, A. J., Frankenberg, C., & Kort, E. A. (2019). Interpreting contemporary trends in atmospheric methane. In *Proceedings of the National Academy of Sciences of the*

United States of America (Vol. 116, Issue 8, pp. 2805–2813). National Academy of Sciences. https://doi.org/10.1073/pnas.1814297116

Wang, Y., Wu, Z., Ma, N., Wu, Y., Zeng, L., Zhao, C., & Wiedensohler, A. (2018). Statistical analysis and parameterization of the hygroscopic growth of the sub-micrometer urban background aerosol in Beijing. *Atmospheric Environment*, *175*, 184–191. https://doi.org/10.1016/j.atmosenv.2017.12.003

Wilkinson, J., Bors, C., Burgis, F., Lorke, A., & Bodmer, P. (2018). Measuring CO2 and CH4 with a portable gas analyzer: Closed-loop operation, optimization and assessment. *PLoS ONE*, *13*(4). https://doi.org/10.1371/journal.pone.0193973

Wimmer, D., Buenrostro Mazon, S., Manninen, H. E., Kangasluoma, J., Franchin, A., Nieminen, T., Backmann, J., Wang, J., Kuang, C., Krejci, R., Brito, J., Goncalves Morais, F., Martin, S. T., Artaxo, P., Kulmala, M., Kerminen, V.-M., & Petäjä, T. (2017). Direct observation of molecular clusters and nucleation mode particles in the Amazon. *Atmospheric Chemistry and Physics Discussions*, *August*, 1–37.

Wu, T., & Boor, B. E. (2021). Urban aerosol size distributions: A global perspective. In *Atmospheric Chemistry and Physics* (Vol. 21, Issue 11, pp. 8883–8914). Copernicus GmbH. https://doi.org/10.5194/acp-21-8883-2021

Wu, Y., Wang, X., Yan, P., Zhang, L., Tao, J., Liu, X., Tian, P., Han, Z., & Zhang, R. (2017). Investigation of hygroscopic growth effect on aerosol scattering coefficient at a rural site in the southern North China Plain. *Science of the Total Environment*, *599–600*, 76–84. https://doi.org/10.1016/j.scitotenv.2017.04.194

6. Conclusions and Recommendations for Future Work

In chapter 2, a daily routine unmanned aerial system-based measurements of vertical ozone and particulate matters were conducted at Riverside, CA. The default PBL scheme is found to be biased from the ceilometer observation. Additionally, the importance of NOx as an ozone precursor was found to be underestimated. These findings emphasize the importance of considering vertical mixing in the PBL when simulating surface ozone in the CMAQ model. It is recommended to incorporate vertical validation and enhance the diffusivity scheme in the model to improve its accuracy.

Chapter 3 demonstrates an Aircore based UAS air sample collection system. Four deployments were performed in the San Joaquin Valley, CA. The system was able to reliably profile methane and carbon dioxide concentrations in the low troposphere and estimate wind information from the rotational kinematics of a multirotor UAS. Using the concentration and wind profiles, the emission footprint and rate were estimated, providing a cost-effective and easily deployable method to quantify emissions in addition to the conventional ground measurements. The limitations in the deployment of multirotor UAS and Aircore atmospheric sampling, such as flight duration and payload weight limits, will be addressed in future work. Additionally, a new multirotor UAS and Aircore design will be developed to provide transects of the emission plumes for better characterization of emissions.

Chapter 4 presents the first deployment of the CAGE chamber system at the DOE Southern Great Plains (SGP) site in the late summer and fall of 2021. During the three-

month operation, the dual chambers show consistent growth with ambient conditions. By using one chamber as the reference and the other as the perturbation chamber, the sensitivity of particle growth with the addition of gas precursors such as α-pinene and SO_2 was studied. Multiple NPF events were observed and analyzed with meteorological and aerosol observations. The study also investigated the impact of different seed particle compositions on particle growth rates by introducing dry ammonium sulfate particles into the reference chamber and dry potassium sulfate particles into the perturbed chamber. In the future, the CAGE chamber system will be combined with the oxidation flow reactors (OFRs) uncder diverse atmospheric conditions in various regions.

In chapter 5, the observations from the TRACER-MAP campaign were presented. The measurements of aerosol, volatile organic compounds, trace gas, and meteorological data were performed utilizing the Baylor-UH-Rice-UCR Mobile Air Quality Laboratory (MAQL2) across Houston between July and August of 2022. This study focused on aerosol measurements obtained from five sites: La Porte, University of Houston, San Jacinto Battleground, Aldine, and Jones Forest. The aerosol size distributions were unimodal across all sites, with the highest concentration in urban and biogenic environments. The volume distributions were bimodal, with the highest volume concentration observed at the Battleground site for a potential dust event. New particle formation events were frequent at UH and Jones Forest sites. The CCN activity decreased as the supersaturation level increased, with a small difference between the supersaturation levels of 0.37 and 0.64. The University of Houston, Battleground, and AMF1 sites

showed a moderate diurnal cycle, while the Jones Forest site showed consistent hygroscopicity.